DEMOCRATIC AND POPULAR REPUBLIC OF ALGERIA
MINISTRY OF HIGHER EDUCATION AND SCIENTIFIC RESEARCH
UNIVERSITY OF FERHAT ABBES SETIF 1

PhD THESIS

PRESENTED AT FACULTY OF SCIENCES
DEPARTMENT OF PHYSICS
TO OBTAIN THE DEGREE OF

DOCTOR

OPTION: CONDENSED MATTER PHYSICS

Presented by :
SI ABDALLAH Fatma

Structural, electronic and magnetic properties of graphene and h-BN 2D nanomaterials on Co substrate: an *ab-initio* study

---

Discussed publicly at /06/2021

Jury committee:

Pr.	KAMEL KASSALI	Univ. Ferhat Abbas Setif	President
Pr.	KHELLIL BOUAMAMA	Univ. Ferhat Abbas Setif	Supervisor
Pr.	SALIM MOURAD CHÉRIF	Univ. Sorbonne Paris North	Co-supervisor
Pr.	HAKIM BAAZIZ	Univ. Mohamed Boudiaf M'sila	Examiner
Pr.	DJAMEL MAOUCHE	Univ. Ferhat Abbas Setif	Examiner

Résumé: Les matériaux bidimensionnels (2D) tels que le graphène et l'hexagonal de nitrure de bore (*h*-BN), en raison des propriétés uniques qu'ils possèdent, ont suscité un intérêt croissant en tant que plateforme pour présenter des applications potentielles et futures dans les dispositifs optoélectroniques et spintroniques. Dans ce travail, nous avons étudié les propriétés structurale, magnétique et électronique des monocouche et bicouches de graphène et d'*h*-BN en interfaces avec un substrat de cobalt, en nous basant sur des calculs *ab-initio*. Ainsi, nous avons étudié l'effet d'un substrat de cobalt à travers une étude approfondie des systèmes graphène/Co(0001) et *h*-BN/Co(0001), pour différentes configurations d'empilement et déterminer les configurations les plus stables. Les principales propriétés électroniques et magnétiques sont expliquées au moyen des hybridations d'interface et de transfert de charge entre les atomes de *Co* et les atomes de *C* (*B* et *N*). Enfin, dans le cas du graphène, nous avons traité une situation plus compliquée lorsque les deux couches sont en rotation avec différents angles ce qui reflète le cas expérimental réel.

Abstract: Two-dimensional layered materials such as graphene and hexagonal boron nitride (*h*-BN), due to the unique properties they possess, have attracted increasing interest as a platform to present potential and future applications in optoelectronics and spintronics devices. In this work, we investigated the structural, magnetic, and electronic properties of monolayer and bilayer graphene and *h*-BN interfaced with a cobalt surface based on *ab-initio* calculations. Thus, we investigated the effect of a cobalt substrate through a deep study of graphene/Co(0001) and *h*-BN/Co(0001) systems, for different stacking configurations and find the more stable configurations. The main electronic and magnetic properties are explained by means of interface hybridizations and charge transfer between the *Co* atoms and *C* (*B* and *N*) atoms. Finally, for the graphene, we study a more complicated situation when the two layers are twisted, with different angles, which reflect the real experimental case.

ملخص: جذبت المواد ثنائية الأبعاد (2D) مثل الغرافين ونتريد البورون السداسي (*h*-BN)، نظرًا للخصائص الفريدة التي تمتلكها، اهتمامًا متزايدًا كمنصة لعرض التطبيقات المحتملة والمستقبلية في الأجهزة الإلكترونية الضوئية والإلكترونات السبينية. في هذا العمل، درسنا الخصائص الهيكلية والمغناطيسية والإلكترونية لواجهات الأحادية والثنائية الطبقات من الغرافين و*h*-BN مع ركيزة الكوبالت، بناءً على حسابات *ab-initio*. وعلى إثر هذا، قمنا بدراسة تأثير ركيزة الكوبالت من خلال دراسة متعمقة لأنظمة الغرافين /(0001) Co و*h*-BN /(0001) Co، لتكوينات المتراصة المختلفة ولتحديد التكوينات الأكثر استقرارًا. يتم شرح الخصائص الإلكترونية والمغناطيسية الرئيسية عن طريق تهجين ونقل الشحنة بين ذرات Co وذرات C (B وN). أخيرًا، في حالة الغرافين، تعاملنا مع حالة أكثر تعقيدًا عندما تدور الطبقتان بزوايا مختلفة مما يعكس الحالة التجريبية الحقيقية.

DEDICATION

This thesis is dedicated to my beloved parents for all their encouragement, support and blessings.

ACKNOWLEDGEMENTS

First of all, I am thankful to Allah for his mercy and blessings.

I would like to express my sincere and faithful gratitude to my advisors, Prof. Khellil Bouamama and Prof. Salim Mourad Chérif for their excellent guidance and support throughout my research years. They have been perfect advisors in every aspect. Their technical insight helped me to go forward in the right direction, while their patience and confidence in me was a source of encouragement. I appreciate Prof. Samir Farhat who has contributed a large portion of my research, his knowledge and proficiency in this field have been an inspiration.

I would like to express my deep appreciation to my thesis committee for generously offering their time, and guidance throughout the discusses period and for reviewing this thesis and for the useful input to improve the manuscript.

I would also like to thank my friends and colleagues that I met during my PhD study.

Finally, my biggest thanks goes to my family.

.

TABLE OF CONTENTS

LIST OF FIGURES

LIST OF TABLES

LIST OF ABBREVIATIONS

CNT	Carbon Nanotube
SWCNT	Single-Walled Carbon Nanotube
MWCNT	Multi-Walled Carbon Nanotube
0D, 1D, 2D, 3D	Zero-, One-, Two-, Three-Dimensional
BZ	Brillouin Zone
SLG	Single Layer Graphene
BLG	Bilayer Graphene
TBG	Twisted Bilayer Graphene
HOMO	Highest Occupied Molecular Orbital
LUMO	Lowest Unoccupied Molecular Orbital
FCC	Face-Centred Cubic
BCC	Body-Centred Cubic
HCP	Hexagonal Close-Packed
VASP	Vienna Ab initio Simulation Package
PAW	Projected Augmented Wave
vdW	Van der Waals
DFT	Density Functional Theory
LDA	Local Density Approximation

GGA   Generalized Gradient Approximation

PAW   Projector Augmented Wave

PBE   Perdew Burke Ernzerhof functional

BO   Born-Oppenheimer

HF   Hartree-Fock

TF   Thomas-Fermi

HK   Hohenberg-Kohn

KS   Kohn-Sham

SCF   Self-Consistent Field

TS   Tkatchenko-Scheffler

PDOS   Projected Density of States

DOS   Density of States

BS   Band Structure

Preface

Nanoscience and nanotechnology is emerging as a leading frontier of research and development in natural sciences, engineering as well as the anticipated pillars of the high-tech industry of this century. The tremendous interest in materials science confined to nanoscales stems from the fact that these nanomaterials exhibit fundamentally unique properties with great potential to revolutionize next-generation technologies in electronics, computing, optics, biotechnology, medical imaging, automotive, aerospace, food, and energy [KTK18]. Science advances through a symbiotic interaction between theory and experiment: theory is used to interpret experimental results and may suggest new experiments, an experiment helps to test theoretical predictions and may lead to improved theories. Quantum mechanics is the most important achievement of the last century, as it is not only the basis of modern physics theory but also the main driving force of the so-called third wave of the industrial revolution. From a pedagogical point of view, the 1 nanometer scale requires the concepts of "quantum mechanics" which, once introduced, are key to understanding behaviour down to the atomic level. The application of numerical calculations based on density functional theory (DFT) is rapidly becoming available for many materials modelling problems in physics, chemistry, materials science, and multiple branches of engineering, to understand the fundamental relationships between physical properties or phenomena and material dimensions [War14].

Objective

In 2004, a single layer of graphene was successfully isolated [NGM$^+$04], leading to the attribution of the Nobel Prize to A. Geim and K. Novoselov in 2010 [GN10a]. Since then, interest has opened up to other types of 2D materials such as dichalcogenides and van der Waals structures (stacks of different *2D* materials) [MOP$^+$17]. Indeed, such layered structures have wonderful electronic, mechanical, thermal and optical properties and quickly proved useful in areas such as electronics, spintronics, and optoelectronics [FBF$^+$15, HWWL02].

The aim of this thesis is to gain a deeper understanding of the adsorption effect of graphene or hexagonal boron nitride on a ferromagnetic surface via first-principles calculations, within corrected dispersion studies, wherein the structural, magnetic and electronic properties of graphene (Gr) and hexagonal boron nitride (*h*-BN) are investigated.

Thesis Outline

This thesis manuscript is organized as follows: I will start with the introduction then the **chapter 1** who has an overview of *2D* materials is presented with an emphasis on Gr and *h*-BN, and the basic concepts of surfaces are introduced to study both *h*-BN and Gr based systems. In **chapter 2**, a brief review of the theoretical framework used in this thesis is presented. The concept of functional density theory is introduced, along with the challenges to developing enhanced exchange-correlation E_{xc} functionals. **Chapter 3** with **chapter 4**, presents and discusses the results. I was interested in *2D* materials with a special focus on Gr and *h*-BN/ metal interfaces, namely *h*-BN/Co(0001) and Gr/Co(0001). Equilibrium configurations, distances between atoms, charge transfers and magnetic moments at the interfaces were carefully determined. Cases of Gr (*h*-BN) monolayer and bilayers are treated, along with the case when the Gr bilayers are twisted. Finally, I conclude with the main findings of this work and provide a perspective for the direction of future research.

SOME ASPECTS OF NANOMATERIALS

Contents

1.1 Introduction

In this chapter, we intoduce some aspects dealing with nanomaterials and some of their applications. A focus will be devoted to *2D* materials, such as graphene and hexagonal boron nitride, that have been widely studied in this thesis work by means of first-principle calculations. I will recall some concepts of crystallography useful for the rest of the manuscript. Finally, I will briefly introduce the computational approach used in this work, and which will be developed in chapter 2.

1.2 Nanostructural Materials

Nanomaterials are materials with a nanoscale ranging in size from 1 to 100 *nm* at least in one dimension (Figure 1.1). Nanostructures and nanomaterials have become one of the most active research fields in the areas of solid-state physics, chemistry, and engineering. Evidence of this interest is provided by number of conferences and research papers devoted to the subject [EC98]. Nanomaterials exhibit multifunctional properties which are distinctively different from that of bulk materials. This is because of having a large fraction of surface atoms per unit volume. The ratio of surface atoms to interior atoms changes dramatically if one successively divides a macroscopic object into smaller parts. For example, the crystals in the nanometer scale have a low-melting-point, reduced lattice constants, different crystal structure, disappearance or shift of Curie temperatures (of ferroelectrics and magnetic materials), changed electrical conductivity of metals or oxides, increased oxidation and wear resistance, and higher sensitivity of sensors compared to their bulk counterparts. The semiconductors and metals nanoparticles become insulators and semiconductors, respectively, when the characteristic size few nanometers [Cao04].
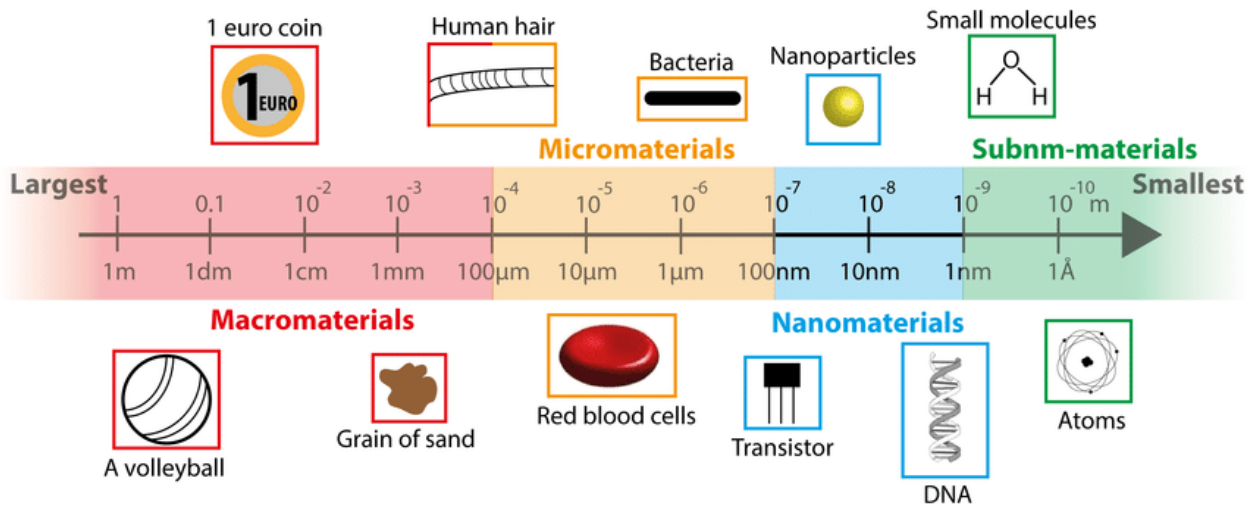
Figure 1.1: Nanomaterials have a characteristic dimension in the size range from 1 to 100 *nm*. The presented length scale offers a frame of reference for the reader. Adapted from [War14]

1.3   Carbon Nanostructures

In this work, I was more particularly interested in *2D* carbon-based nanostructures, such as graphene, and in a *2D* system with 2 different atoms, hexagonal boron nitride. I present in the following some aspects relating to this type of nanomaterial, starting with the introduction of carbon fullerene, which can be considered as the basic system of carbon-based nanostructures.

1.3.1   Fullerene

Fullerenes are zero-dimensional closed cage molecules for carbon allotropic that have the ability to form various shapes such as a hollow sphere, an ellipsoid, or a tube [MA18]. The most well-known member of the buckminsterfullerene family is called buckyballs (C_{60}), which is made up of 12 pentagonal and 20 hexagonal carbon atoms (see Figure 1.2).
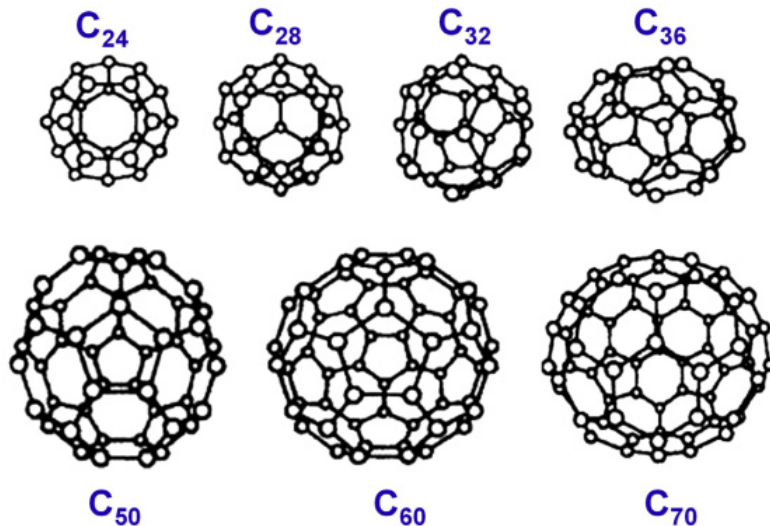
Figure 1.2: Types of fullerenes. Adapted from [MA18]

1.3.2   Carbon Nanotube

Carbon nanotubes (CNTs) cylindrical in shape are form of carbon nanostructure. There are two types of CNTs: the single-walled carbon nanotubes (SWCNTs) and the multi-walled carbon nanotubes (MWCNTs), in which there are various possible classes of SWCNT, named zigzag, chiral and armchair [RTM08]. In order to describe such nanotubes, chiral vector (C_h) defines the unit cell, the C_h vector is defined as the circumference of the tube surface and is given by [OHKL98]:

$$\vec{C}_h = n\vec{a}_1 + m\vec{a}_2 \equiv (n, m)$$

Where *n, m* are the integers that characterise the chiral vector, $\vec{a}_1$ and $\vec{a}_2$ are the two basis vectors of graphene. The chiral angle (θ) as depicted in Figure 1.3 can be obtained from [RT08]:

$$\tan\theta = \frac{\sqrt{3}m}{2n+m}$$

The chiral angle and indices separate carbon nanotubes into three classes : zigzag ($m = 0, n > 0, \theta = 0°$), chiral ($0 < |m| < n, 0 < \theta < 30°$) and armchair ($n = m, \theta = 30°$) [PAV17].
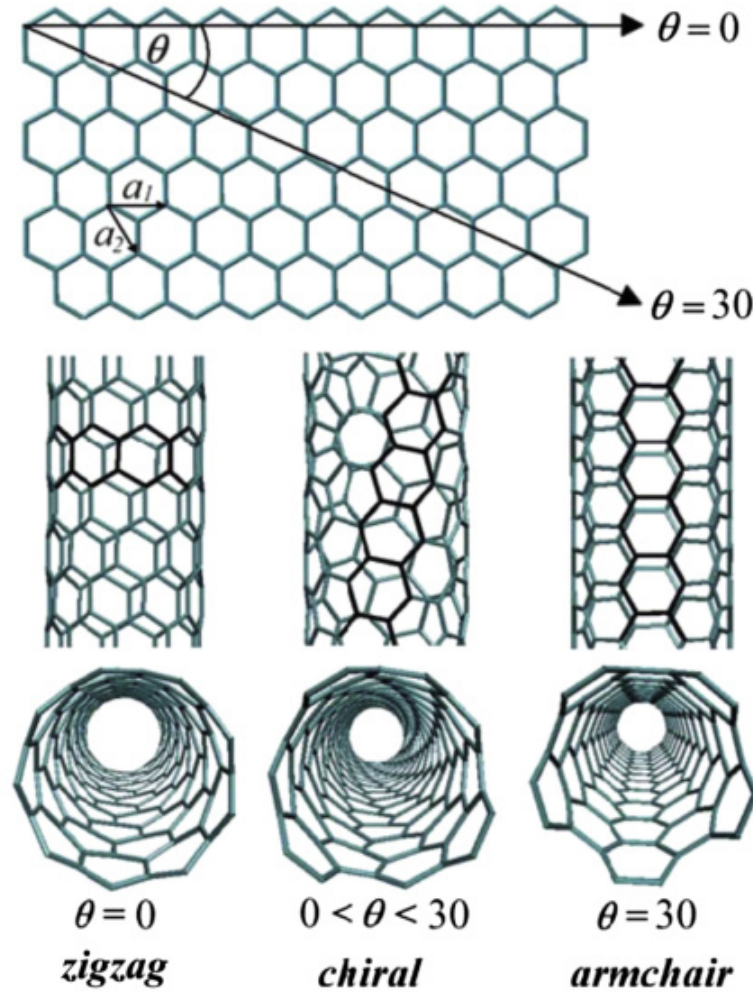
Figure 1.3: Classification of carbon nanotubes: (*left*) zigzag, (*middle*) chiral and (*right*) armchair. Adapted from [MA18]

1.3.3 Graphene

Graphene is the name given to a flat single layer of carbon atoms tightly packed into a two dimensional (*2D*) honeycomb lattice and is a basic building block for graphitic materials of all other dimensionalities (Figure 1.4). It can be wrapped up into *0D* fullerenes, rolled into *1D* nanotubes or stacked into *3D* graphite [GN10b].
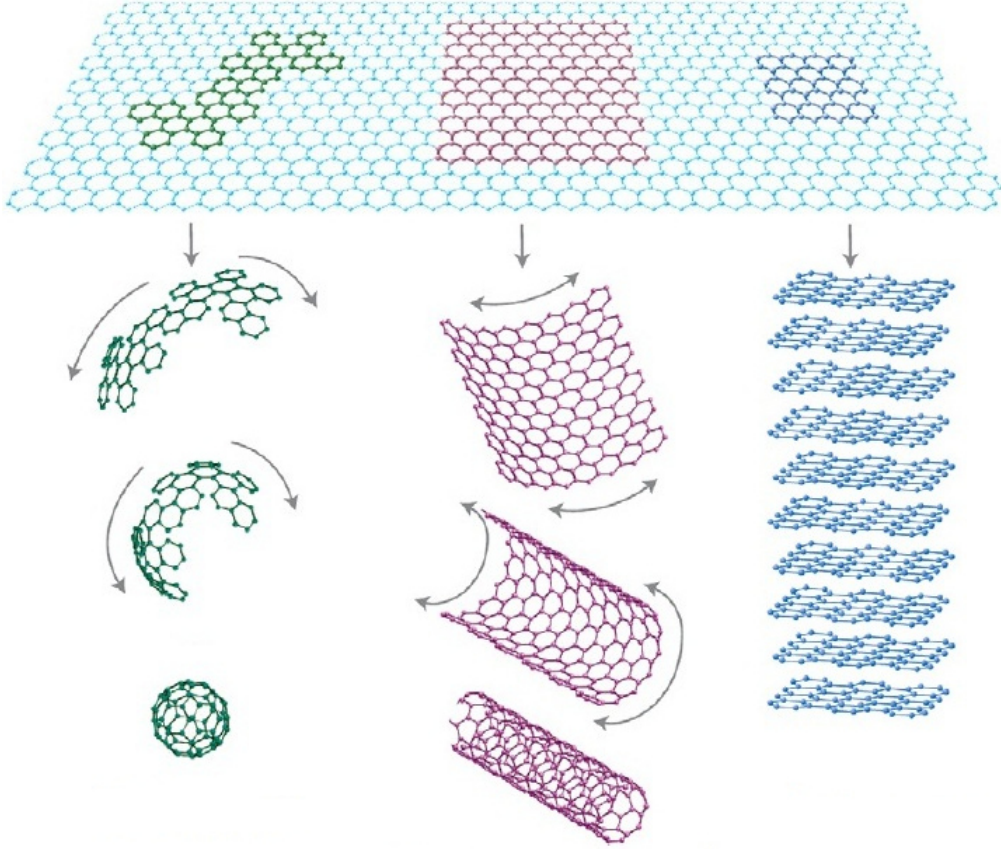
Figure 1.4: Graphene is the basis of all graphitic forms. Wrapped in buckyballs shape (*0D*), rolled as nanotubes (*1D*) or stacked in layers like graphite (*3D*). Adapted from [AGEA15]

Graphene has a honeycomb crystal lattice, and its unit cell includes two carbon atoms at the *A* and *B* sites (Figure 1.5 a). The Bravais lattice is triangular where lattice vectors are defined as follows [KK12]:

$$\vec{a}_1 = \frac{a}{2}(3, \sqrt{3}), \quad \vec{a}_2 = \frac{a}{2}(3, -\sqrt{3})$$

Where $a \approx 1.42$ Å is the distance to the nearest neighbours, which is called a carbon-carbon bond. The reciprocal lattice is also triangular, with the lattice vectors are given by

$$\vec{b}_1 = \frac{2\pi}{3a}(1, \sqrt{3}), \quad \vec{b}_2 = \frac{2\pi}{3a}(1, -\sqrt{3})$$

High symmetry points *K*, *K'* and *M* appear for the Brillouin zone (BZ), along with wave vectors (Figure 1.5 b).

$$\vec{K}' = \left(\frac{2\pi}{3a}, \frac{2\pi}{3\sqrt{3}a}\right), \quad \vec{K} = \left(\frac{2\pi}{3a}, -\frac{2\pi}{3\sqrt{3}a}\right), \quad \vec{M} = \left(\frac{2\pi}{3a}, 0\right)$$
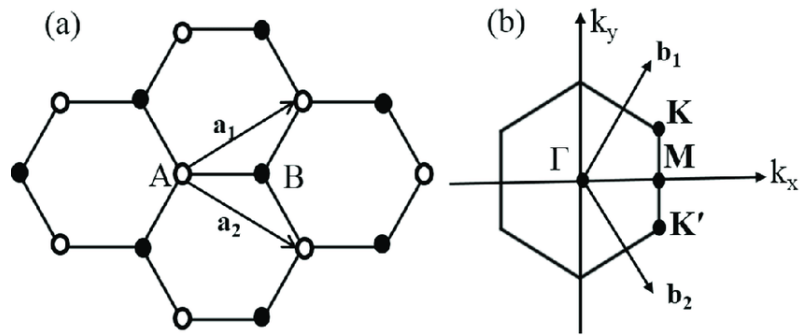
Figure 1.5: (a) The honeycomb lattice structure of graphene. The unit cell consists of carbon atoms represented by A and B, $\vec{a}_1$ and $\vec{a}_2$ are the lattice vectors and (b) corresponding Brillouin zone, showing the high-symmetry points. Adapted from [Wol14a]

The graphene band structure shows the many branches of energy that resulting from the π and σ electrons, which are produced by the outermost electrons of carbon [WA11]. Dirac point at the K-point of the Brillouin zone is created by the valence π-band and conduction π^*-band (Figure 1.6), while the task of σ-bond is to give the distinctive hexagonal structure (Figure 1.6).
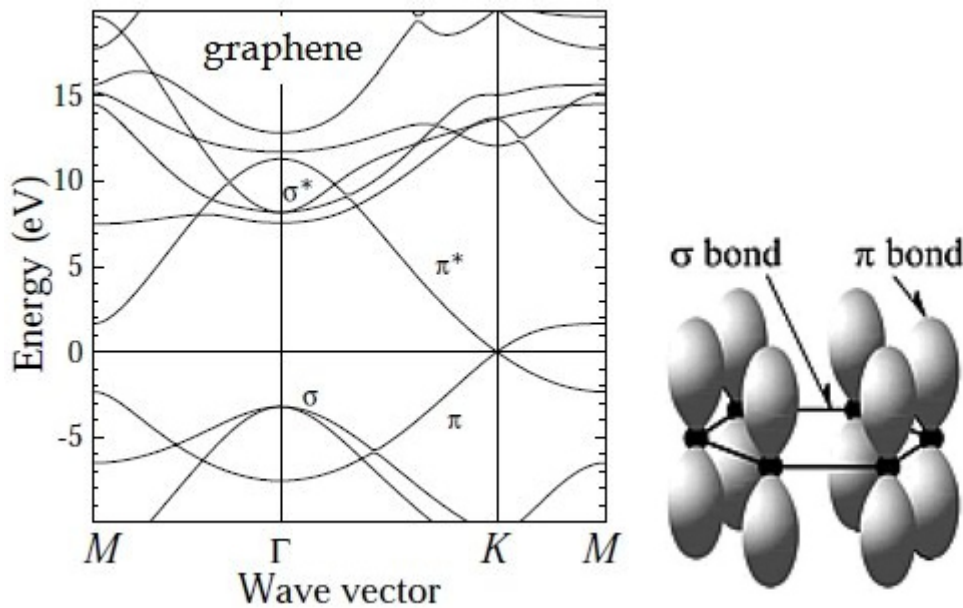
Figure 1.6: (*left*) Electronic band structure of graphene, (*right*) schematic of the in-plane σ-bonds and the π orbitals perpendicular to the plane of the graphene sheets. Adapted from [CLSK10]

First systematic and illustrative study used the tight-binding model, by approximating the nearest-neighbour that can solve the Schrödinger equation and can obtain the energy dispersion relationship of π (bonding) and π^* (antibonding) bands to display band structure of graphene in a *3D* image (Figure 1.7 a), where the valence and the conduction band touch each other in the Brillouin zone at six points giving Dirac cones. From these six points, only two are nonequivalent indicated by K and K' [CL11].
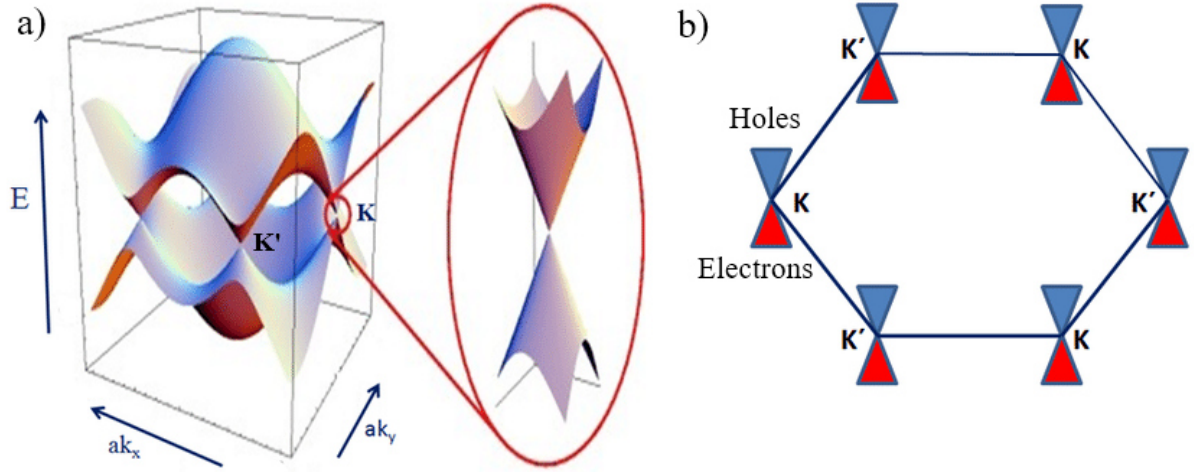
Figure 1.7: (a) The electron energy spectrum of graphene in the nearest-neighbour approximation and (b) hexagonal Brillouin zone of honeycomb lattice, showing intersecting conical electron bands. Adapted from [Per09]

Bilayer graphene (BLG) can generally be described as two single layers graphene (SLGs) stacked parallel to each other. Three limited cases are possible: if $\theta = 0°$ ($M = N$), the honeycomb layers perfectly match and the so-called AA stacking is obtained (Figure 1.8 a)(this means that atoms of the same type in the graphene unit cell usually denoted in graphene literature as A- or B-type atoms do overlay); when A-type atoms are superimposed on B-type atoms (or vice versa), one gets the so-called AB stacking, which can be obtained by a full rotation by ($\theta = 60°$) (Figure 1.8 b). In a twisted BLG, the angles are confined as form $0° < \theta < 60°$ (Figure 1.8 c), the large commensurate supercells can be obtained for $\theta \sim 0°$ either by choosing large M and N values, for which $|M - N|$ is small or for angles $\theta \sim 30°$ with large $|M - N|$. In order to get an angle $\theta \sim 60°$ close to the perfect AB stacking one can choose N=1 (or M=1) and large M (or large N) [TLMM10]. The (M, N) index for the commensurate twisted BLG is related with the twist angle θ, the cell size L_{cell}, and the number of atoms N_{atom} in the unit cell as follows

$$\cos\theta = \frac{N^2 + 4NM + M^2}{2\left(N^2 + NM + M^2\right)}$$

$$L_{\text{cell}} = d\sqrt{3\left(N^2 + NM + M^2\right)}$$

$$N_{\text{atom}} = 4\left(N^2 + NM + M^2\right)$$

where d is the *C-C* distance in the graphene layer, and (M, N) is a pair of integers.
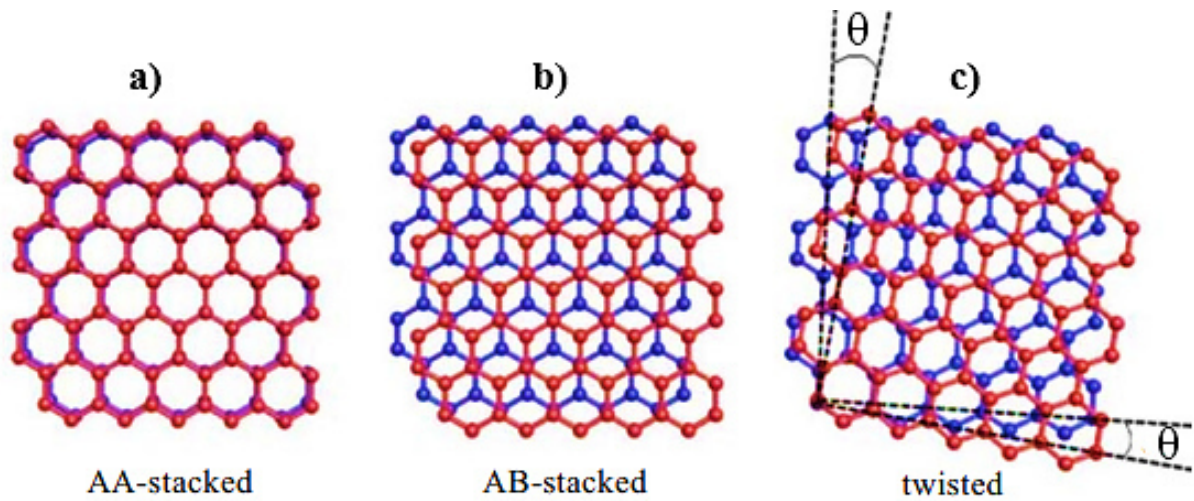
Figure 1.8: Three categories of bilayer graphene: (a) AA-stacked, (b) AB-stacked and (c) twisted BLG. Adapted from [YHZ18]

1.4 Two-Dimensional Materials

1.4.1 The Case of Boron Nitride Nanosheet (*h*-BN)

h-BN belongs to the family of *2D* materials, which range in thickness from one layer to a few atomic layers, *h*-BN consist of sp^2-conjugated boron and nitrogen atoms that form a honeycomb structure [BGR16]. It is alike in geometry to its all-carbon graphene, as illustrated in Figure 1.9.
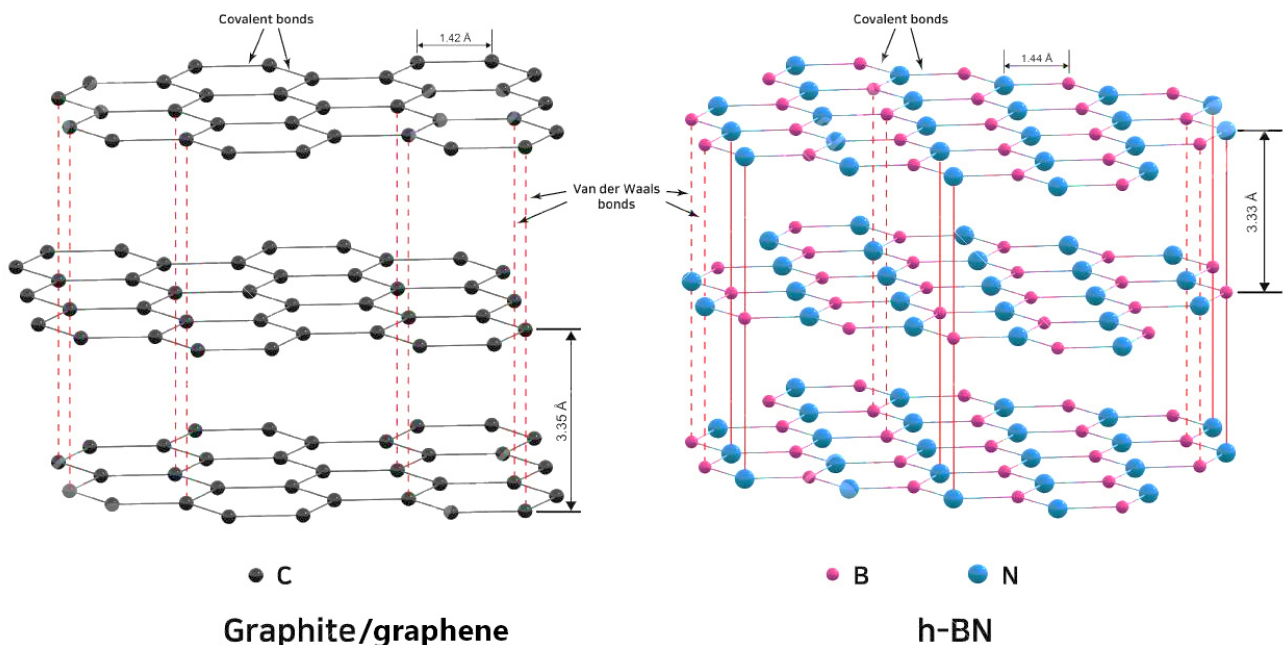
Figure 1.9: Hexagonal boron nitride and carbon graphite crystalline structure. Adapted from [Nay16]

h-BN is the only one among the two-dimensional materials with a wide band-gap [WMS17], the HOMO and LUMO levels of the *2D h*-BN are determined by π and π^* which are located in the *N* and *B* atoms as shown Figure 1.10.
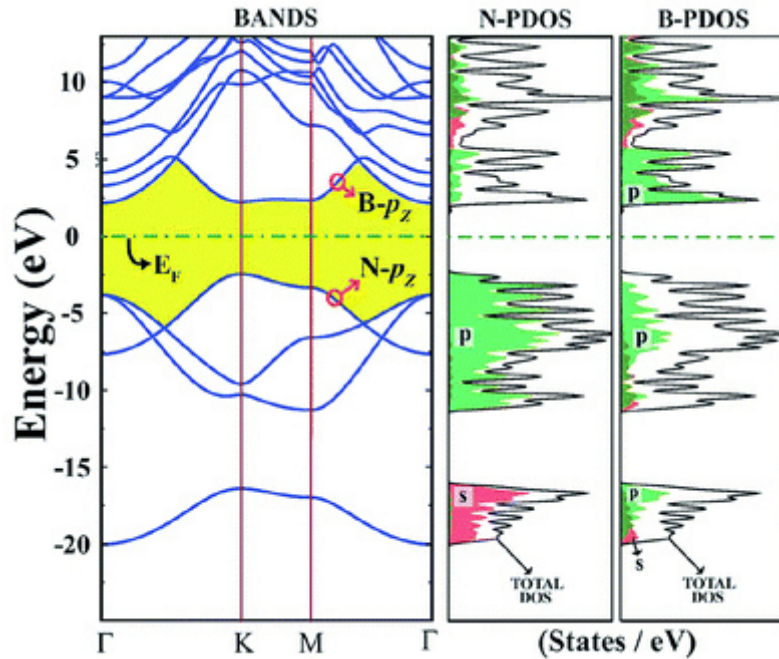
Figure 1.10: Orbital property and electronic structure of *h*-BN. Adapted from [TAC09]

1.5 Some Applications of 2D Materials: Example of Graphene and *h*-BN

1.5.1 Graphene

(a) Spintronics: Graphene plays an important role in spintronic devices because the weak spin-orbit (SO) coupling and hyperfine interaction in carbon atoms entail exceptionally long spin diffusion lengths while including high charge carrier mobility, and gate-tunable charge carrier density [KSF14, AOG$^+$20], with these outstanding properties, is an excellent candidate for the creation of a full spectrum of spintronic nanodevices beyond current technologies, including ultra-low energy demand devices and circuits comprising (re-) writable microchips, transistors, logic gates [FBF$^+$15].

(b) Photonics: 2D graphene shows future prospects for electronic devices and systems. In high-speed optoelectronic devices, graphene's high-carrier mobility is a benefit. Applications in a variety of spectral regions will gain from graphene's broad spectral absorption. For applications requiring robust photonic and nonlinear optical structures graphene's high optical damage threshold and mechanical strength will be paramount [Cur14]. In addition, the ease

of graphene's transfer to other substrates and its ability to conformally coat surfaces make it ideal for integrating hybrid photonic systems. Graphene-based devices are manufactured for use as nonlinear optical and photonic devices: such as optical modulation, photodetectors, solar cells, plasmonics, LED, laser, touchscreens [BHZ17].

1.5.2 *h*-BN

(a) Optoelectronics: 2D-hBN nanosheets exhibit high transparency in the wavelengths from *UV* to *IR*, while the sharp absorption peak appears in the deep ultraviolet (DUV). *h*-BN could be a promising candidate for application in ultraviolet lasing, photon emission, and DUV detectors [ZFW$^+$17]. The detector is more sensitive to DUV light than visible light with a stable sensitivity. *h*-BN possess strong cathodoluminescence (CL) and photoluminescence (PL) emissions in the DUV range. *h*-BN is used as optical and magneto-optical recording media, and for optical disc memories [HWWL02].

(b) Nanoelectronics: The excellent insulating and dielectric properties of *h*-BN combined with the high thermal conductivity. These properties make the *h*-BN a unique *2D* material for the design and fabrication of high-quality devices, such as barriers utilized in field-effect tunnelling transistors and the atomically thin insulators to separate metallic channels, and as insulator layers for MISFET semiconductor. *h*-BN is also applied as a substrate for high-performance devices as windows in microwave apparatus [WWW$^+$16].

1.6   Basic Concepts of Crystallography

One of the major issues the last years in research, in spintronic for instance, is to control the properties of magnetic materials and spins of electrons. An emerging possibility is the coupling of a ferromagnetic (*FM*) with *2D* materials. Indeed, the combination of ferromagnetic transition metals such as *Co, Ni, Fe* and their alloys, with *2D* materials may prove to be an interesting approach. In this context, it is important to study the effects of the interface in the 2D/FM materials. These effects involve mainly hybridizations between the orbitals of the surface atoms of the *FM* and the *2D* material [MJG11]. Thus, in the following, I present some basic aspects of crystallography, well known but useful when I will approach in the next chapters the study of the Graphene/Co or *h*-BN/Co interfaces.

1.6.1 Crystal Structure, Direction and Plane

To understand the difference between bulk and surface, we will mention some basic concepts in crystallography. By considering a group of atoms as mathematical points, all crystalline materials can then be considered as a repeating pattern of points in the space called a lattice. Groups of lattices can be classified into seven crystal systems and 14 Braves lattices. Most pure metals have one of three lattice structures: face-centered cubic (FCC), body-centered cubic (BCC), or hexagonal close-packed (HCP). To better describe the lattice structure, we have to define the coordinate system, which consists of three planar axes along unit cell edges (a, b, c) with the origin at a corner of the unit cell. Once the coordinate system has been defined, any crystal orientation is easy to index. We can consider any crystallographic direction as a vector that can be described by a set of integers [uvw] based on the coordinate system as follows: T $= u$a $+ v$b $+ w$c in which a, b, and c are the axes of the unit cell; T is the vector representing that specific crystallographic direction, and u, v, and w are integers. Thus, we can index any crystallographic direction using a set of integers $[uvw]$ in the coordinate system of the unit cell (Figure 1.11). We use $< uvw >$ to define a family of crystallographic directions that are identical due to the symmetry of the crystals. For any given plane, the plane will either parallel or intercept one of the three axes. The reciprocals of interceptions on three axes are used to index the orientation of the crystallographic planes. This set of integers (hkl) is called the Miller index, we also use {hkl} to index a family of crystal planes if they are identical due to the symmetry of the crystals, just like the crystallographic direction family [KMM96].
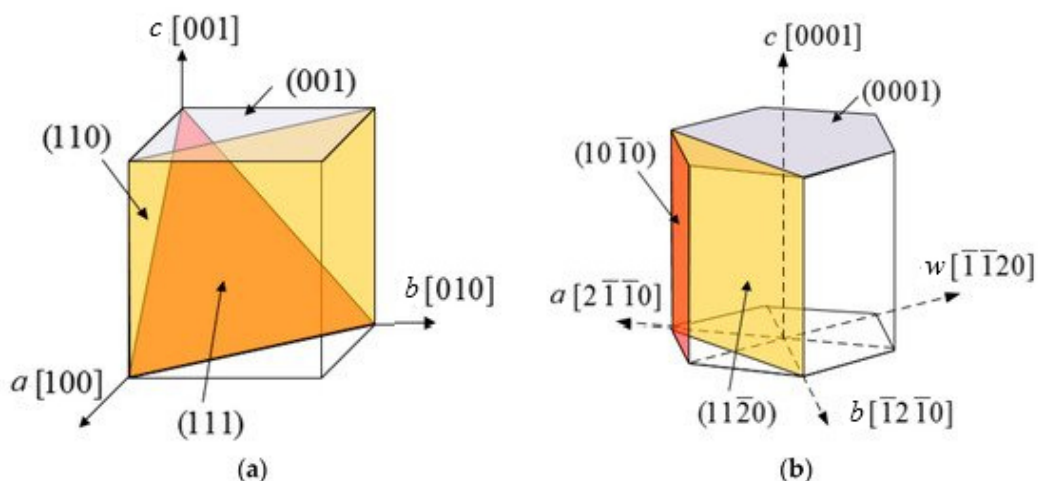
Figure 1.11: Illustration of the low-index surfaces for (a) cubic (001), (110) and (111) and (b) hexagonal (0001), (10$\bar{1}$0) and (11$\bar{2}$0). Adapted from [TCY20]

1.6.2 Surface Structure for Close-Packed Structures

The volume packing density of HCP structures is identical to that of FCC structures as shown in Table 1.1. We know that in the HCP structure, each atom has 12 closest neighbour atoms–6 in the same base plane and 3 each in the hollow site of both the top and bottom planes. With regard to the FCC structure, it has the same packing density as an HCP structure, by plotting the close-packed plane (111), we can clearly see that any atom in this plane has six closest neighbour atoms touching each other. It also has three atoms each on the hollow site on the crystal planes above and below. The only difference between the FCC and HCP structures is that neighbouring atoms on the crystal planes above and below are not in the same set of hollow sites in the FCC structure. In other words, the top and bottom atoms are not aligned together as in the HCP case [GT09].

Table 1.1: Summary of close-packed planes and directions, APF, and closest neighbors for FCC, and HCP structures. Adapted from [GT09]

	FCC	HCP
Close-packed directions	$< 110 >$	Hexagonal edge
Close-packed planes	{111}	Base plane {0001}
Atomic packing factor (APF)	0.74	0.74
Number of closest neighbors	12	12

As mentioned earlier, both FCC and HCP are close-packed structures, where the HCP structure is a close-packed plane (the base plane) stacking structure with ABABAB sequencing, and the FCC structure is nothing but a similar stacking structure of close-packed plane (111) with a sequence of ABCABC. Therefore, the FCC structure is also a close-packed structure with a different stacking sequence. If the surface is their close-packed planes, that is, (111) for FCC and (0001) for HCP as shown in Figure 1.12, each surface atom will be identical and have a coordination number (CN) of nine, or nine closest neighbours–six of them in the plane and three atoms in the very next plane underneath the surface. In addition, the atoms in the very next layer underneath the surface will have a CN of 12, which means that it is already like atoms in the bulk. So this layer in theory can already be considered as being a bulk layer [GT09].
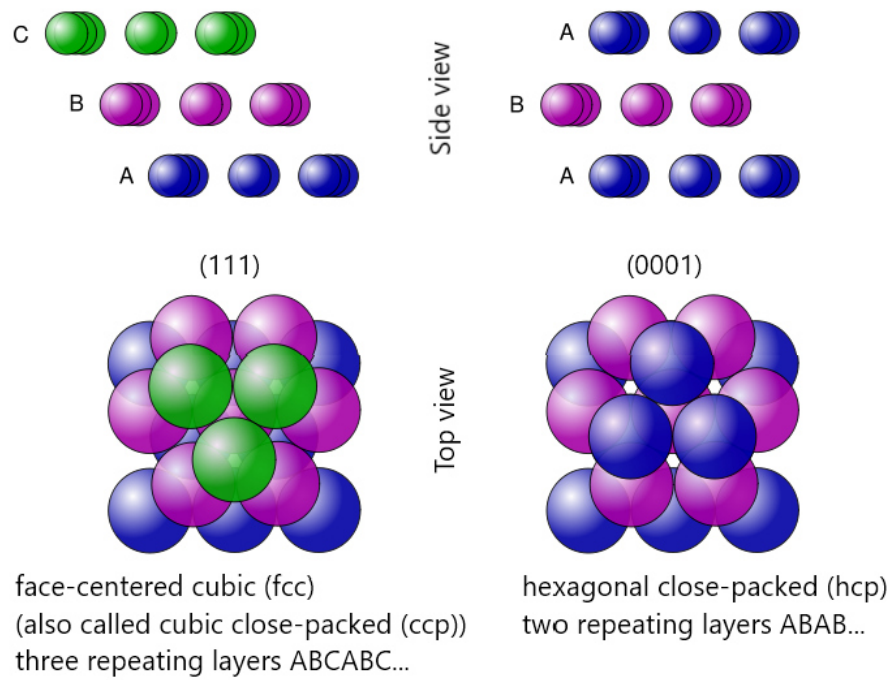
Figure 1.12: Similarities and difference between close-packed structures: (*left*) FCC and (*right*) HCP. Adapted from [Wik21]

1.7   Computational Methodology in This Work

In this thesis, we mainly deal with the *ab-initio* calculations of some physical properties (structural, magnetic and electronic) of ferromagnetic cobalt interfaced with graphene or *h*-BN. The computational methods can provide an efficient approach to study the physical properties of this kind of hybrid nanomaterials that are synthesized in a laboratory. The *ab-initio* results can provide guidance for experimental studies to gain cost and time. In the present work, all the calculation are based on density-functional theory (DFT), one of the most widely recognized used quantum mechanical methods in physics and other sciences, it will be detailed in chapter 2.

1.8 Summary

Nanomaterials can be in different shapes such as nanotube and in the form of layers like *2D* material, I was interested in two-dimensional nanomaterials with unique properties such as: graphene and *h*-BN nanosheets, which have a semi-metal character as in the case of graphene and large band-gap as in the case of *h*-BN. These two materials has a prominent position in many fields and applications, such as optoelectronics and spintronic ... etc. *Ab initio* calculations are a simple and cost-effective approach allowing the study of different combination of *2D* materials with other materials such as the ferromagnetic ones. This is particularly interesting in designing desirable materials and devices with predefined properties providing an effective way to analyze their relevance for different applications, such as in spintronics.

TWO

THEORETICAL BACKGROUND

Contents

2.1   Introduction

In this chapter, an overview of the theory underlying the calculations performed in this manuscript is provided. It presents the Density Functional Theory (DFT) as well as describing an excerpt about the functional used and their development. Finally, the intended purpose adding of the van der Waals dispersion interactions with the method used to determine them.

2.2   Many-Body Schrödinger Equation

The atoms that make up the crystal can be fully described within the unit cell, with the complete crystal formed by the periodic repeating of atoms in the unit cell. The generic unit cell has *3(N +1)* degrees of freedom, where N is the number of atoms contained within the unit cell. This consists of 3 spatial degrees of freedom within the unit cell for each atom, plus 6 degrees of freedom in the unit cell parameters. The translational symmetry of the unit cell that all crystal systems possess removes 3 degrees of freedom. Interactions at the atomic scale are described by quantum mechanics, and the starting point is the non-relativistic Hamiltonian, which is the operator corresponding to the total energy of the atomic system. In the absence of any external field, only the electrostatic potential (Coulomb) and kinetic energies are considered in the time-independent Schrödinger equation [Mar14]:

$$\hat{H}\Psi\left(r_1, r_2, \ldots r_N, R_1, R_2.R_M\right) = \mathrm{E}\Psi\left(r_1, r_2, \ldots r_N, R_1, R_2.R_M\right) \tag{2.1}$$

Where Ψ is the wave function (which represent the eigenvector) of the system, r_i and R_I are the position coordinates of the electrons and nuclei respectively. The Hamiltonian operator $\hat{H}$ is given:

$$\begin{aligned}
\hat{H}_{tot} = &\sum_i -\frac{\hbar^2}{2m_e}\nabla_i^2 + \sum_I -\frac{\hbar^2}{2M_I}\nabla_I^2 + \frac{1}{2}\sum_{i\neq j}\frac{e^2}{4\pi\epsilon_0\left|r_i - r_j\right|} \\
&+ \sum_{i,I} -\frac{Z_Ie^2}{4\pi\epsilon_0\left|r_i - R_I\right|} + \frac{1}{2}\sum_{I\neq J}\frac{Z_IZ_Je^2}{4\pi\epsilon_0\left|R_I - R_J\right|}.
\end{aligned} \tag{2.2}$$

m_e denotes the mass of an electron, M_I and Z are respectively the mass and the charge (atomic number) of the nuclei, and ∇^2 is the Laplacian operator. The half factor in the electron-electron and nucleus-nucleus Coulomb terms is to prevent double-counting. The Hamiltonion can be decomposed into five items:

$$\hat{H}_{tot} = \hat{T}_e + \hat{T}_n + \hat{V}_{e-e} + \hat{V}_{e-n} + \hat{V}_{n-n} \tag{2.3}$$

The first two terms correspond respectively to the kinetic energies of the electrons and of the nuclei. The last three terms correspond to electrostatic potential energies. Firstly between pairs of

electrons, then between the electrons with the nuclei ,and finally between pairs of nuclei. For simplicity, the atomic units will be used in the following ($\hbar = m_e = |e| = 4\pi\epsilon_0 = 1$). The Schrödinger equation can be written as:

$$\hat{H}\Psi = \left[-\frac{1}{2}\sum_i \nabla_i^2 - \frac{1}{2M_I}\sum_I \nabla_I^2 - \sum_{i,I} \frac{Z_i}{|r_i - R_I|} + \frac{1}{2}\sum_{i \neq j} \frac{1}{|r_i - r_j|} + \frac{1}{2}\sum_{I \neq J} \frac{Z_I Z_J}{|R_I - R_J|} \right] \Psi = E\Psi \tag{2.4}$$

It is clear that finding the ground state (E) solution of the Schrödinger equation (2.4) is not an easy task. In fact, it is impossible to solve this equation exactly. However, it is possible to make a number of approximations to this equation, based on physical arguments, so that approximate solutions are feasible.

2.2.1 Born-Oppenheimer Approximation

One of the main steps in simplifying the problem to separate the motion of the nuclei and the electrons through the Born-Oppenheimer approximation [BO27]. This is based on the fact that the nuclear masses are much heavier ($\sim 10^3$) than the electron mass so that the nuclei move much slower than the electrons. Thus, in the electron reference frame, the nuclei can be considered to be at rest (i.e., the kinetic energies of the nuclei vanish) and the electrons move in the static field generated by the nuclei plus the other electrons. The wave function can be expressed as a product of the nuclear wave function and the electron wave function

$$\Psi(\mathbf{r}, \mathbf{R}) = \Psi_e(\mathbf{r})\Phi_n(\mathbf{R}) \tag{2.5}$$

The total Hamiltonian $\hat{H}$ (Eq.2.3) takes the form of the electronic $\hat{H}_e$ Hamiltonian, which can be written as

$$\hat{H}_e = \hat{T}_e + \hat{V}_{e-e} + \hat{V}_{e-n} \tag{2.6}$$

The Schrödinger equation for the entire system (electrons plus nuclei) reduces to the form

$$\hat{H}_e\Psi_e = E_e\Psi_e \tag{2.7}$$

Even with this simplified approximation of Schrödinger's equation (2.7), the exact resolution remains impossible when systems have two or more electrons. This is due to the bi-electronic repulsion term of the Hamiltonian ($\hat{V}_{e-e}$) which has no analytical solution. Several methods have been developed in order to approach the exact solution as precisely as possible and which are more or less satisfactory as we shall see later.

2.2.2 Hartree & Hartree-Fock Approachs

Hartree [Har28] simplifies the interaction of the N-body problem into an independent electron problem, where each electron moves alone in the mean-field generated by nuclei and other electrons, i.e. our problem is capable of solving the multi-electron Schrödinger equation, the total electronic wave function can be expressed as a product of the wave function of each electron in its respective orbital

$$\Psi\left(\mathbf{r}_1, \ldots, \mathbf{r}_N\right) = \prod_{i=1}^{N} \psi_i\left(\mathbf{r}_i\right) \tag{2.8}$$

Thus, each one-particle wave function is a solution of the mono-electronic Schrödinger equation

$$\left[-\frac{1}{2}\nabla^2 + V_{eff}(\mathbf{r})\right]\psi_i(\mathbf{r}) = \varepsilon_i\psi_i(\mathbf{r}) \tag{2.9}$$

with :

$$V_{eff}(\mathbf{r}) = V_{ext}(\mathbf{r}) + V_H(\mathbf{r}) \tag{2.10}$$

where V_{ext} is the interaction potential of an electron with nuclei and V_H represents the Hartree potential of the electron-electron interaction, it is given as follows

$$V_H = \sum_{j \neq i} \int |\psi_j(\mathbf{r}\prime)|^2 \frac{1}{|\mathbf{r} - \mathbf{r}\prime|} d\mathbf{r}\prime \tag{2.11}$$

These individual wave functions could now be solved independently. However, the simplicity of Hartree's approach failed to capture the anti-symmetry of the wave function, leading to a violation of Pauli's exclusion principle [PEVM94].

The Hartree-Fock [Foc30] approximation of the electronic wave function with a Slater [Sla29] creates an anti-symmetric product of non-interacting wave functions. Since electrons are fermions that do not have the same spin, they cannot occupy the same position. The N electron wave function is formed by a Slater determinant of one-electron orbitals, as is shown in this formula:

$$\Psi(\mathbf{r}) = \frac{1}{\sqrt{N!}} \begin{vmatrix} \psi_1\left(\mathbf{r}_1\right) & \psi_1\left(\mathbf{r}_2\right) & \cdots & \psi_1\left(\mathbf{r}_N\right) \\ \psi_2\left(\mathbf{r}_1\right) & \psi_2\left(\mathbf{r}_2\right) & \cdots & \psi_2\left(\mathbf{r}_N\right) \\ \vdots & \vdots & \ddots & \vdots \\ \psi_N\left(\mathbf{r}_1\right) & \psi_N\left(\mathbf{r}_2\right) & \cdots & \psi_N\left(\mathbf{r}_N\right) \end{vmatrix} \tag{2.12}$$

where $\frac{1}{\sqrt{N!}}$ is the normalization factor of this wave function.

with the determinant, the Hartree-Fock equation is then written as:

$$\begin{aligned} &\left[-\frac{1}{2}\nabla^2 - V_{ext}(\mathbf{r}) + \sum_{j \neq i} \int |\psi_j(\mathbf{r}\prime)|^2 \frac{1}{|\mathbf{r} - \mathbf{r}\prime|} d\mathbf{r}\prime\right] \psi_i(\mathbf{r}) \\ &- \sum_{i \neq j} \delta_{S_i S_j} \int \psi_j^*\left(\mathbf{r}'\right) \psi_i(\mathbf{r}\prime) \frac{1}{|\mathbf{r} - \mathbf{r}\prime|} d\mathbf{r}\prime \psi_j(\mathbf{r}) = \varepsilon_i\psi_i(\mathbf{r}) \end{aligned} \tag{2.13}$$

This equation contains an additional term compared with the Hartree equation, the last term at the bottom is pure quantum mechanics, which is called the exchange term.

System of equations (Eq.2.13) is solved by the Self-Consistent Field (SCF) method insofar as the potentials depend on the wave functions. Due to the number of variables they depend on, these calculation methods become very heavy or even impossible to apply to large systems. The solution to this problem did not begin until after the birth of the functional density theory. The main objective of DFT is to replace the multiple electron wave function with electron density as the basic quantity for computations. In this way, the ground state energy of the studied system will be determined thanks to the resolution of an equation which no longer depends on the wave function with 3N variables but on the density which depends only on the 3 spatial coordinates [PW89].

2.3 Foundations of Density Functional Theory (DFT)

2.3.1 Thomas-Fermi Theory

The concept of using the electron density instead of a wave function can be traced back to the work of Thomas-Fermi [Tho27, Fer27], in which the kinetic energy of electrons is approximated as an explicit functional of the density based on non-interacting electrons in a homogeneous gas. Within this model, the total energy is obtained

$$E_{TF}[\rho] = \frac{3}{10}\left(3\pi^2\right)^{2/3}\int \rho^{5/3}(\mathbf{r})d\mathbf{r} + \int V_{ext}(\mathbf{r})\rho(\mathbf{r})d\mathbf{r} + \frac{1}{2}\iint \frac{\rho(\mathbf{r})\rho(\mathbf{r}')}{|\mathbf{r}-\mathbf{r}'|}d\mathbf{r}d\mathbf{r}' \qquad (2.14)$$

where the first term is the kinetic energy of electrons while the second and the third terms corresponds to the electron-nuclei and the Coulomb part of the electron-electron interactions, respectively. Although it is an important first step, the Thomas-Fermi model remains unsuitable, not only due to the poor description of the uniform gas in the representation of the kinetic energy, but also the complete neglect of exchange and correlation terms.

2.3.2 Hohenberg-Kohn Theorems

Hohenberg–Kohn [HK64] outlined DFT in terms of the following two theorems for non-degenerate ground electronic states: the first theorem states that *for any system of interacting electrons in an external potential $V_{ext}(r)$, the external potential is a unique functional of the ground-state electronic density $\rho(r)$.*
This theorem states that there exists a one-to-one (bijective) mapping between the ground-state wave function and the ground-state electron density [SS11]. That is, for each non-degenerate ground state density $\rho(r)$, there exists only one external potential energy $V_{ext}(r)$ that leads to

this density, and for each non-degenerate ground state density $\rho(r)$, there exists one and only one ground state wave function ψ which would give rise to this density. This defines map C between the potential energies $V_{ext}(r)$ and the wave functions ψ, and establishes the map D between wave functions and densities, as shown in Figure 2.1.
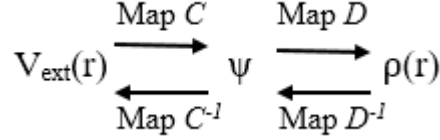
Figure 2.1: Maps relating the correspondence between external potential energies, ground state wave functions, and ground state densities. Adapted from [Sah14]

The second theorem proves the variational principle, which is defined as follows: *There exists a universal functional for the energy in terms of density. The global minimum of this functional is the ground state energy of the system, and the corresponding density is the ground state density.* Can be expressed the total energy as functional (i.e., functions of another function), this a functional is written as follows

$$E_{HK}[\rho(\mathbf{r})] = F[\rho(\mathbf{r})] + \int V_{ext}(\mathbf{r})\rho(\mathbf{r})d\mathbf{r} \qquad (2.15)$$

where

$$F[\rho(\mathbf{r})] = T[\rho(\mathbf{r})] + E_{e-e}[\rho(\mathbf{r})] \qquad (2.16)$$

$F[\rho(\mathbf{r})]$ represents the universal functional of Hohenberg-Kohn.

The minimization of the total energy by a simple variation of the function $\rho(r)$ is then possible and will lead to the density and the energy of the ground state. In other words, the functional $E[\rho(\mathbf{r})]$ satisfies a variational principle.

$$E[\rho(\mathbf{r})] \geq E[\rho_0(\mathbf{r})] = E_0 \qquad (2.17)$$

Although the Hohenberg–Kohn theorem is established as the fundamental theorem of quantum physics based on electron density, it is not in itself sufficient to calculate the universal functional $F[\rho(\mathbf{r})]$ [Tsu14].

2.3.3 Kohn-Sham Scheme

The approach used by Kohn-Sham [KS65] is to reformulate the entire problem as a non-interacting theory, based on the HK theorems to transform an interactive system into a non-interactive one via effective external potentials, assuming that the electronic ground states are the same (see Figure 2.2). Kohn-Sham's thinking is best illustrated by carefully rewriting the expression of the total energy functional and fine-tuning the newly written terminology.
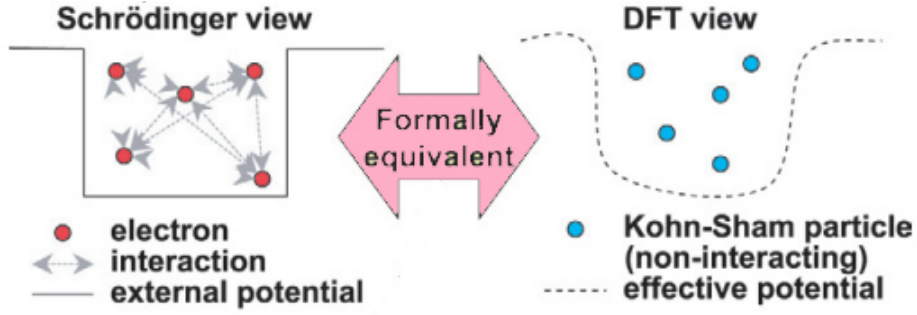
Figure 2.2: Transformation of the real interactive system into a fictitious non-interactive system (*left*) a real system made up of many electrons in mutual interaction (*right*) fictitious system of the independent electrons. Adapted from [MSD+04]

The total energy functional in the Kohn-Sham method given by the equation:

$$E_{KS}[\rho(\mathbf{r})] = T_s[\rho(\mathbf{r})] + E_{e-e}[\rho(\mathbf{r})] + \int V_{\text{ext}}(\boldsymbol{r})\rho(\mathbf{r})\mathrm{d}\boldsymbol{r} \qquad (2.18)$$

T_s is the kinetic energy of independent particles that the gives equation

$$T_s[\rho(\mathbf{r})] = -\frac{1}{2}\sum_i \int \psi_i^*(\mathbf{r})\nabla^2\psi_i(\mathbf{r})\mathrm{d}\mathbf{r} \qquad (2.19)$$

E_{e-e} is the electron-electron electrostatic interaction, the E_{xc} is the non-classical exchange-correlation energy.

$$E_{e-e}[\rho(\mathbf{r})] = \frac{1}{2}\iint \frac{\rho(\mathbf{r})\rho(\mathbf{r}')}{|\mathbf{r}-\mathbf{r}'|}d\mathbf{r}d\mathbf{r}' + E_{xc}[\rho(\mathbf{r})] \qquad (2.20)$$

Here ψ_i is one-electron orbitals of Kohn-Sham and the electron density is defined as:

$$\rho(\mathbf{r}) = \sum_i |\psi_i(\mathbf{r})|^2 \qquad (2.21)$$

The Schrödinger-like equation for each non-interacting electron is given by the formula

$$\hat{H}_{KS}\psi_i(\boldsymbol{r}) = \epsilon_i\psi_i(\boldsymbol{r}) \qquad (2.22)$$

$\hat{H}_{KS}$ acts as a Hamiltonian, defined as:

$$\hat{H}_{KS} = -\frac{1}{2}\nabla_i^2 + V_{ks}(\mathbf{r}_i) \qquad (2.23)$$

The term V_{ks} is called the KS-effective potential, and V_H is the classical Hartree potential defined in equation (2.11)

$$V_{ks}(\mathbf{r}) = V_{ext}(\mathbf{r}) + V_H(\mathbf{r}) + V_{xc}(\mathbf{r}) \qquad (2.24)$$

where V_{xc} is the exchange-correlation potential defined as:

$$V_{xc}(\mathbf{r}) = \frac{\delta E_{xc}[\rho(\mathbf{r})]}{\delta\rho(\mathbf{r})} \qquad (2.25)$$

The numerical approach for solving the Kohn-Sham equation is illustrated by a flowchart in Figure 2.3. One gives an initial guess of the electron density function $\rho(r)$, determines the KS-effective potential V_{ks} and solve the Kohn-Sham equation with a chosen approximation for the exchange-correlation functional, then constructing the density via $\rho(\mathbf{r}) = \sum_i |\psi_i(\mathbf{r})|^2$, reconstructs the density and compare to the initial density, the algorithm repeats itself until the desired convergence is reached as the total energy is minimized, i.e. self-consistent [Liu17].
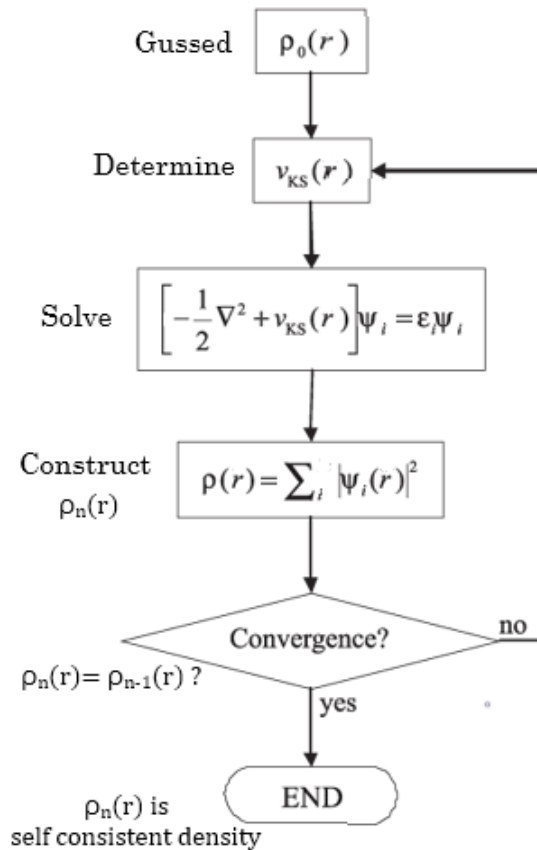
Figure 2.3: Flowchart of the iterative solution within the Kohn-Sham method. Adapted from [OSHD09]

2.3.4 Exchange-Correlation Energy

For practical use of the Kohn-Sham equations, we must know what the form of the exchange-correlation energy functional is. However, the exact form of E_{xc} is unknown. A type of approximation was used for E_{xc} to list approximate functions with varying levels of complexity.

2.3.4.1 Local Density Approximation (LDA)

The simplest approximation is the assumption that the exchange-correlation effect is purely local and can be described by the exchange-correlation energy of a uniform electron gas with a specifie density. This is called the local density approximation (LDA). The exchange-correlation

functional with LDA is written as:

$$E_{xc}^{LDA}[\rho(\mathbf{r})] = \int \rho(\mathbf{r})\varepsilon_{xc}^{unif}[\rho(\mathbf{r})]d\mathbf{r} \qquad (2.26)$$

Where, ε_{xc}^{unif} is the exchange-correlation energy per electron of an electron gas with uniform density.

2.3.4.2 Generalized Gradient Approximation (GGA)

The generalized gradient approximation is another form of exchange-correlation which is semilocal, due to the non-uniformity nature of electron gas in real systems, as it takes into account the contribution from the gradient of the density $\nabla\rho(\mathbf{r})$. This can be expressed as:

$$E_{xc}^{GGA}[\rho(\mathbf{r})] = \int \rho(\mathbf{r})f_{xc}[\rho(\mathbf{r}), \nabla\rho(\mathbf{r})]d\mathbf{r} \qquad (2.27)$$

Here $f_{xc}[\rho(\mathbf{r}), \nabla\rho(\mathbf{r})]$ is also a functional of the local density and its gradient.

2.3.4.3 Hybrid Functional

The exchange part in Kohn-Sham is poorly described, while the exchange part in Hartree-Fock is defined exactly. Although the direct combination of the correlation part of KS and the exchange part of HF gives poor results [Koh06]. Thus mixing of KS and HF, and regroup the exchange and correlation parts of both methods with the intention of achieving an additional degree of accuracy. The hybrid functionals can be formally written as:

$$E_{xc}^{\text{Hybrid}}[n(\mathbf{r})] = aE_x^{\text{HF}} + (1-a)E_x^{\text{LDA(GGA)}} + E_c^{\text{LDA(GGA)}} \qquad (2.28)$$

where the coefficient a is either determined experimentally or estimated theoretically, E_x and E_c is exchange and correlation energies respectively.

2.3.4.4 Van der Waals Dispersion Interactions

Failure to describe long-range electron correlations (electron dispersion forces) occurs due to the approximate nature of exchange-correlation functionals such as LDA and GGA, this is because not taking into account the instantaneous density fluctuations and using only local properties to calculate exchange-correlation energy, in which the addition of reliable dispersion corrections is a fairly recent addition to the DFT toolkit that gives satisfactory results [Pro19].

vdW Dispersion Corrections (DFT+vdW)

In this type of method, vdW interactions within DFT are described, by calculating the total energy $E_{DFT-disp}$ as the sum of the standard Kohn-Sham energy E_{KS-DFT} and the semi-empirical dispersion correction E_{disp}, given as follow [Gri04]

$$E_{\text{DFT}-\text{disp}} = E_{\text{KS}-\text{DFT}} + E_{\text{disp}} \tag{2.29}$$

The general form of the dispersion term is

$$E_{disp} = -\sum_{A<B} \sum_{n=6,8,10,\dots} f_n^{damp}(R_{AB}) \frac{C_n^{AB}}{R_{AB}^n} \tag{2.30}$$

where C_n^{AB} are the dispersion coefficients for the atom pair A and B separated by the distance R_{AB}^n and f_n^{damp} is a damping function preventing.

vdW Functional (vdW-DF)

The principle of the approach consists of finding a non-local contribution to the exchange-correlation functional used in a DFT calculation, it is expressed as [DRS⁺04]

$$E_{xc}^{\text{vdW}-\text{DF}}[\rho(r)] = E_x^{\text{GGA}}[\rho(r)] + E_c^{\text{LDA}}[\rho(r)] + E_c^{\text{nl}}[\rho(r)] \tag{2.31}$$

with the simplest form of the non-local correlation energy part, is defined in equation.

$$E_c^{\text{nl}} = \frac{1}{2} \iint \rho(\mathbf{r}) \phi(\mathbf{r}, \mathbf{r}') \rho(\mathbf{r}') \, d\mathbf{r} d\mathbf{r}' \tag{2.32}$$

2.4 Pseudopotential Method

The basic idea of pseudopotential is to replace the real potential arising from both the core electrons and ionic cores with an effective potential (see Figure 2.4). The primary application in this electronic structure is to replace the strong Coulomb potential of the nuclei and the effects of the tightly bound core electrons by an effective ionic potential acting on the valence electrons. The motivation for using pseudopotentials is to reduce the number of electrons, and consequently the number of orbitals involved in a calculation [Mar04].

Among the most important pseudopotentials approximation is the projector augmented wave (PAW) method [Blö94]. This method preserves the core electrons (in a frozen state) and the full all-electron valence wave functions and the true wave functions are replaced by smooth wave functions. The core wave functions are imported directly from all-electron calculations for the considered atom. This formalism offers the advantage that it combines the efficiency of the pseudopotential approach while providing good accuracy.
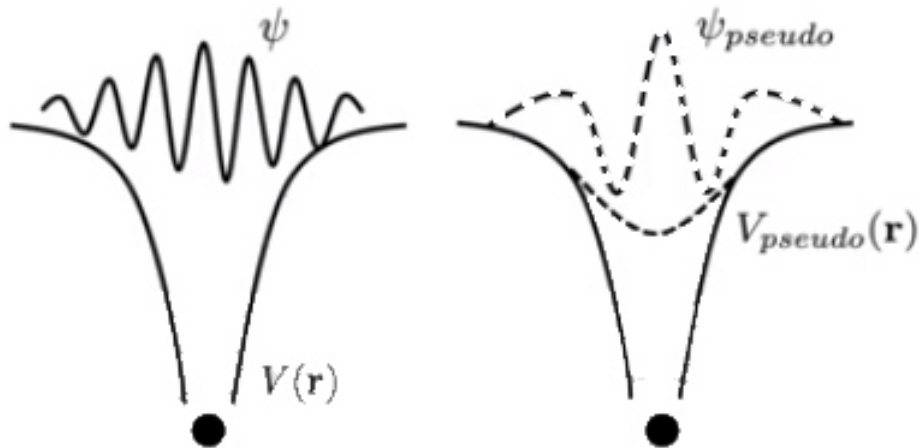
Figure 2.4: Schematic illustration of all-electron (solid line) and pseudo-electron (dashed line) potentials and their corresponding wave functions. Adapted from [Böe19]

2.5 Why and How Van der Waals (vdW) Dispersion Interactions were Selected ?

Dispersion interactions depend on electronic correlation, but DFT generally ignores long-range dispersion because of the term of exchange-correlation, V_{xc}, it is generally supposed to be a function of the local electronic density $V_{xc}(\rho)$, or gradient of the electronic density $V_{xc}(\partial\rho/\partial r)$. A consequence of this assumption is that only local contributions to the electronic correlation are included. Therefore, typical DFT functionals do not model correlations outside the Fermi hole and thus neglect long-range dispersion. The LDA and GGA ignore the far-reaching non-local correlations that give rise to vdW forces. Several functions have been developed to model dispersive interactions. These functionals do not contain the explicit term dispersion, but they have been parameterized on systems governed by dispersion interactions and have shown some success for the modelling of the compound associated with dispersion. In the VASP code, there are a few methods implemented to include vdW interactions: DFT-2D [Gri06], DFT-3D [GAEK10, GEG11], DFT-dDsC [SC11a, SC11b], MBD@rsSCS [TDJCS12, ARDJT14], DFT-TS [TS09], DFT-TS/HI [BLHA13, BLÁH14], TS+SCS [TDJCS12] and vdW-DF [DRS+04, KRPSL09] with the functionals (optPBE-vdW, optB88-vdW, and optB86b-vdW) [KBM09] and also SCAN + rVV10 [PYPS16], vdW-DF2 [LMK+10] and vdW-DF2-B86R [Ham14].

Among these methods, we have compared some of them to choose which one we are going to use in our study. For this purpose, we calculated the elastic properties of graphene and compared the obtained value of Young's modulus with the experimental value one [LWKH08]. The 2D elastic constants for hexagonal lattice are C_{11} and C_{12}, where due to symmetry these structures have $C_{11} = C_{22}$.

Generally, when calculating in first-principles, and using the constraint-based least squares adjustment method, C_{ij} can be obtained from the following formula [WLKG18]:

$$E_S = \frac{1}{2}C_{11}\varepsilon_{xx}^2 + \frac{1}{2}C_{22}\varepsilon_{yy}^2 + C_{12}\varepsilon_{xx}\varepsilon_{yy}$$

Where E_S is the deformed energy defined by $E_s = E_{tot} - E_0$, where E_{tot} is the total energy of the deformed system, E_0 is the total energy of the system without deformation. The Young modulus (E), the Poisson's ratio (v) and shear modulus (G) are: $E = \frac{C_{11}^2 - C_{12}^2}{C_{11}}$, $\nu = \frac{C_{12}}{C_{11}}$ and $G = \frac{1}{2}(C_{11} - C_{12})$. The results obtained are shown in Table 2.1 with the experimental value of The Young modulus (E) for comparison.

Table 2.1: The elastic constants (C_{ij}), Young's (E) and shear modulus (G) in GPa * nm as well as the Poisson's ratio (v). The values in brackets are the uncertainties with the experimental value [LWKH08].

	C_{11}	C_{12}	**E**	**G**	v
DF2	348	61.8	337 (0.89%)	143.10	0.178
DF3	358	68.7	345 (1.37%)	144.65	0.192
TS	349	62.9	338 (0.71%)	143.05	0.180
TS/HI	352	64.1	340 (0.09%)	143.95	0.182
MBD	352	63.9	341 (0.20%)	144.05	0.181
B86R	348	62.4	337 (1.04%)	142.80	0.179
vdW-DF2	342	56.4	332 (2.29%)	142.80	0.165
Ref.			340 [a]		0.186 [b]

[a] Ref. [LWKH08]   [b] Ref. [LML07]

The results obtained from Young's modulus (E) for the different van der Waals methods: DFT-2D, MBD@rsSCS, DFT-TS and DFT-TS/HI are in very good agreement with the experimental one with an uncertainty lower or equal to 1% and the obtained values of the Poisson's ratio are all equal to 0.18. In the case of DF3, the uncertainty is 1.4% and the poison coefficient is equal to 0.19 (5% greater than the value obtained by the other methods) in the case of vdW-DF2 the uncertainty is 2.3% and $v = 0.165$ (8% lower than the value obtained by the other methods).

In this thesis work, the DFT-TS method [TS09] will be used in the calculations.

2.6 Summary

Density Functional Theory (DFT) has now become a standard tool in both solid-state physics and quantum chemistry for studying the properties of materials at the nanometric scale. After a fairly global review of the theoretical basis on which our numerical simulations are based, in the next chapter I present the findings related to studying the structural, electronic and magnetic properties of the h-BN and graphene interfaces with the surface of cobalt material.

STUDY OF GRAHPENE/COBALT AND H-BN/COBALT INTERFACES

Contents

3.1 Introduction

In this work, we will provide a summary of the method used for calculation. Through ab-initio computations, the structural, magnetic, and electronic properties of mono and bilayer graphene, as well as *h*-BN alone and when absorbed on the surface of Co(0001), were investigated.

3.2 Method and Computational Details

All the calculations performed in this work are based on density functional theory as implemented in the VASP package [KH93, KFH94, KF96]. The generalized gradient approximation of Perdew, Burke, and Ernzerho (GGA-PBE) [PBE96] with vdW correction proposed by the Tkatchenko-Scheffler (DFT-TS) is adopted [TS09]. The projected augmented wave (PAW) pseudopotentials [KJ99, Van90, KH94] are employed to describe the electron-ion interaction. The calculations were made with high precision, and the cut-off energy depending was set to the values of the compounds. The Brillouin zone integration was performed by using the Monkhorst-Pack scheme [MP76] and sampled with a $19 \times 19 \times 1$ k-point mesh. For the structure relaxation, we used the Methfessel-Paxton method [MP89] of the first order and a conjugate gradient scheme until the forces acting on the atoms are less than 1 meV/Å and the total energy less than 10^{-7} eV. We apply a vacuum in the z-direction. We keep the distance ~ 12 Å between the two nearest supercells along the z-axis to prevent the interactions between the neighbouring atoms.

3.3 Graphene

3.3.1 Structural Properties

Graphene is a planar layer of carbon atoms, that atoms are arranged in a honeycomb lattice. For each unit cell the composed of two non-equivalent atoms [AD13]. Graphene bilayer is a two-layer of graphene, the most famous and stable of which is called Bernal stacked (AB) configuration as seen in Figure 3.1.
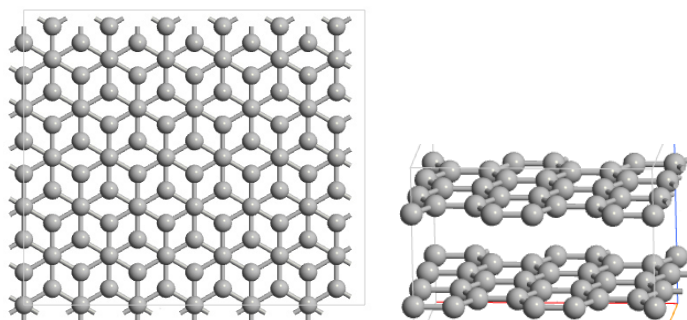
Figure 3.1: Structure of bilayer graphene Bernal stacking (a) top view (b) side view.

3.3.2 Electronic Properties

Dirac point is of great importance that is due to the excellent performance of graphene representing a two-dimensional, zero band-gap semiconductor. It plays a role similar to that Gamma point in a direct band-gap semiconductor. Thus the electronic properties are usually studied near the Dirac point, as near the Gamma point in a direct band-gap semiconductor [SAHR11]. The electronic property of graphene results from its electronic bonds, which contribute to the electron conduction and provides interaction between their layers. Due to the two carbon atoms sublattice in its hexagonal lattice, cone-like the valence and conduction bands intersect at two non-equivalent points of the Brillouin zone (the conduction and valence bands of graphene intersect at the Fermi level on K and K' points of the Brillouin zone) [GPKH14]. The stability of graphene is due to its very compact carbon atoms and sp^2 orbital hybridization. A combination of s, p_x and p_y orbitals make up the σ-bond. The p_z electrons constitute the bond π . The π-bonds hybridize together to form the π-band and the π*-bands. These bands are responsible for most of the notable electronic properties of graphene, via the half-filled band that allows electrons to move freely. The upper half of the dispersion is the conduction π* band and the lower is the valence π-band from the nature of the HOMO and LUMO orbitals as highlighted in *3D* band structure in Figure 3.2(a). Owing to the absence of a band-gap at the Fermi energy, graphene is considered a semi-metal or zero band-gap semiconductor, and in the fact that the conduction and valence bands intersects at $E_F = 0$, this point is known as "Dirac point" or "Dirac cone" [Wol14b]. Single-layer graphene (SLG) and bilayers graphene (BLG) has simple electronic spectra as shown in Figures 3.2(b) and (c), even though the energy dispersion of bilayer graphene exhibits two parabolic branches near K like conventional semiconductors. It is a zero-gap semiconductor also referred to as zero-overlap semimetals with one type of electron and one type of hole. Finally, the ABA stack is a trilayer graphene exhibiting linear and quadratic bands overlapping as shown in Figure 3.2(d).

(a)

(b)

(c)

(d)
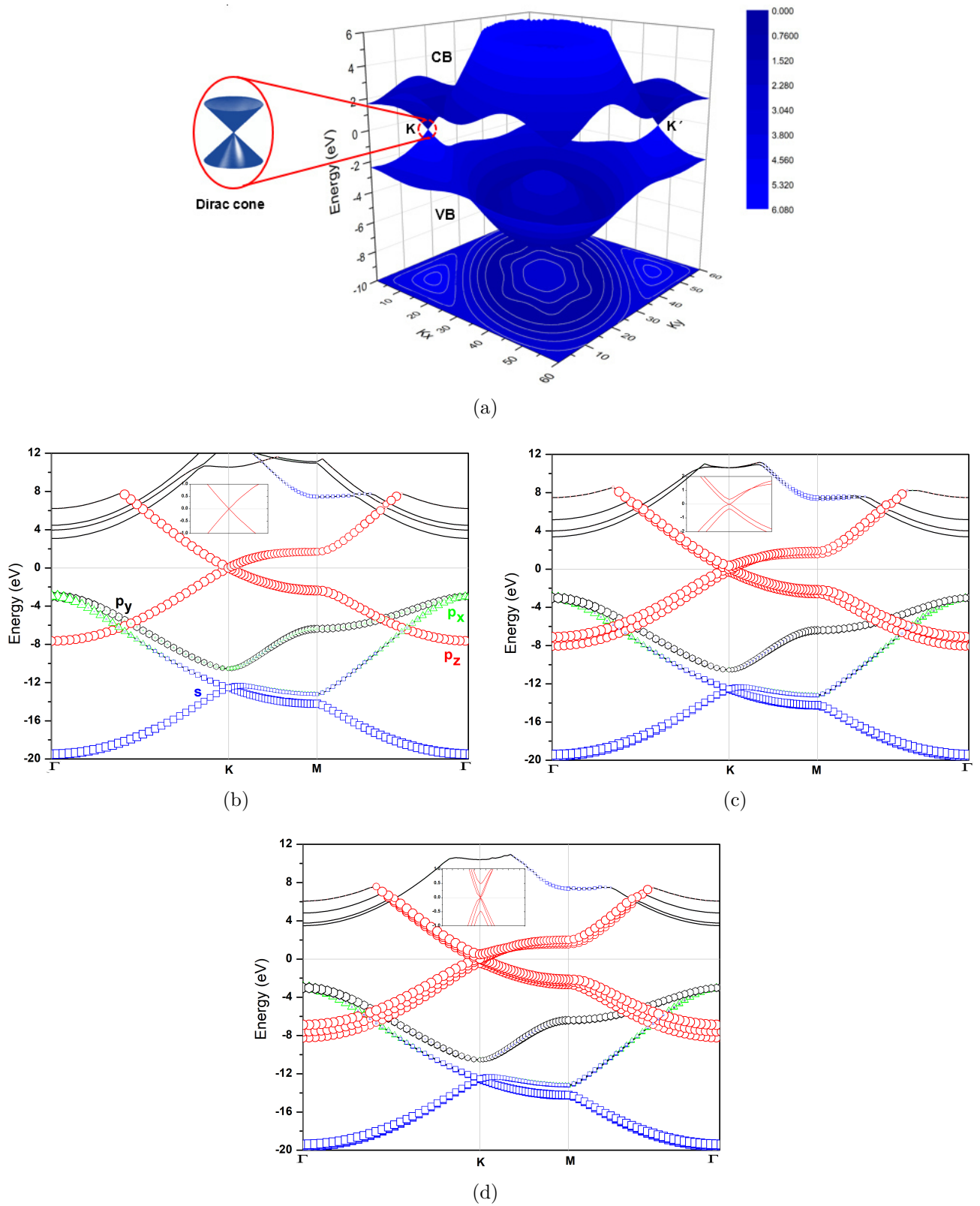
Figure 3.2: (a) *3D* band structure of single-layer graphene, (b-d) the orbital projected electronic bands structures of graphene mono, bi and trilayer respectively.

33

3.4 *h*-BN

3.4.1 Structural Properties

Hexagonal boron nitride (*h*-BN) is a *2D* insulator, known as the "white graphite", in which there are five stacking patterns for bilayers that are described according to the position of boron relative to a nitride [RP11]. We have focused our studies on AB2' stacking, that shows atomic isostructure to graphite as shown in Figure 3.3, where *B* and *N* atoms alternate in a planar hexagonal network. These atoms covalently bonds in-plane and are weakly stacked out-of-plane via the vdW forces.

(a)   (b)
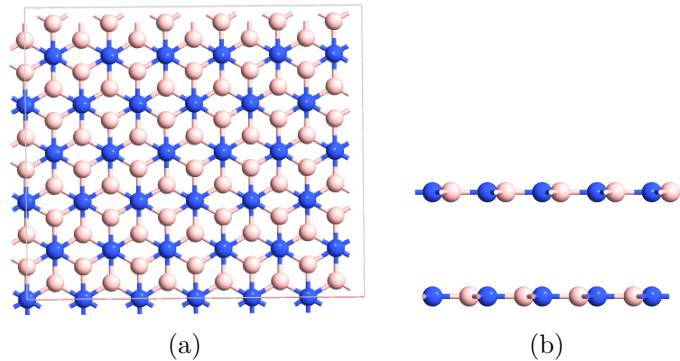
Figure 3.3: Structure of bilayer *h*-BN (a) top view (b) side view. The beige and blue colors are for B and N atoms, respectively.

3.4.2 Electronic Properties

Although a structural similarity of *h*-BN to graphene, nonetheless their electronic properties are quite different, whereas graphene is a zero-overlap semimetal, the *h*-BN is a large band-gap semiconductor (about 6 eV). For the monolayer case, we obtain an indirect gap of about 4.4 eV using the vdW dispersion correction method. When adding to the hybrid functional correction (HSE06) 5.6 eV was obtained (Figure 3.4(a)). In the case of bilayers, we studied the AB2' *h*-BN. We also found an indirect band-gap about 4.2 eV using vdW method and about 5.3 eV introducing the hybrid one (Figure 3.4(b)). These results are consistent with previous research [WWW+13, FS16, GPD+19].
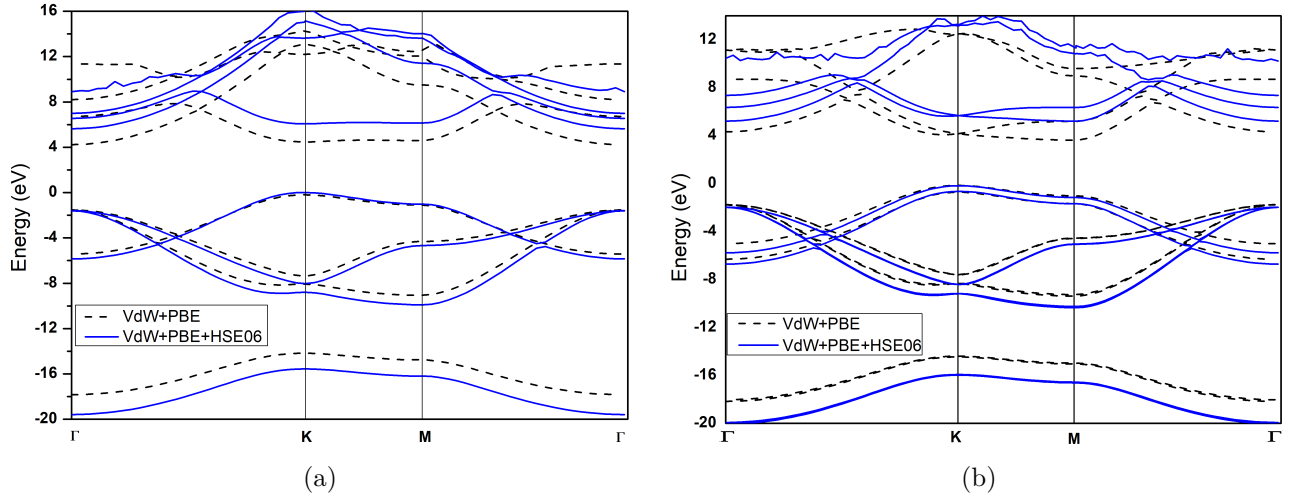
Figure 3.4: Band structure of *h*-BN, (a) monolayer (b) bilayer .

3.5 Cobalt Surface

3.5.1 Structural Properties

Using modelling techniques, we can employ the surface approach via the supercell model to study simulated thin-films. Sheds light in this framework on the cobalt metal, by performing the essential criterions to create a surface structure, we have applied sufficiently broad vacuum region to decouple the slabs and the sufficient slab thickness to mimic semi-infinite crystal, in the first criterion, we opted for a vacuum distance over 10 Å and for the second criterion, we will need to calculate the surfaces energy to check its convergence with layers thickness (n) in the slab. The surface energy γ can be defined as [Boe94]:

$$\gamma = \frac{1}{2A}\left(E_{\text{slab}} - NE_{\text{bulk}}\right) \tag{3.1}$$

where A is the area of the surface in the unit cell, the $1/2$ factor because it exists the two surfaces of a slab, E_{slab} is the energy of the slab, the N is the number of atoms in the surface slab, and E_{bulk} is the bulk energy per atom.

The obtained surface energies are given in Table 3.1. We got the convergence at the five-layer, we have thus conserved the five-layer slab with five cobalt atoms in the constitution of each layer (plane).

Table 3.1: The surface energies as a function of thickness for Co(0001)

Layers thickness (n)	2	3	4	5	6	7	8
Surface energy (J/m^2)	2.10	2.20	2.15	2.19	2.17	2.16	2.18

3.5.2 Magnetic Properties

Table 3.2 reports the values of the magnetic moments for a slab containing five Co layers. Our results indicate that the sides of the slab behave similar is due to the symmetry of the slab surface. The highest magnetic moment is found at the surface (*Co1, Co5*) because of the decrease of atomic coordination numbers of the surface, leading to rising of the magnetic moment also in the adjacent inner layer, but in a smaller proportion (*Co2, Co4*), while the centre layer (*Co3)* has same behaviour with the bulk (1.58 μ_B).

Table 3.2: The magnetic moment of Co(0001) surface

Postion atoms	Co1	Co2	Co3	Co4	Co5
Magnetic moment (μ_B)	1.71	1.63	1.60	1.63	1.71

3.6 Monolayer Graphene/Co(0001) Interface

3.6.1 Structural Properties

Depending on the positions of the atoms that exist in the cobalt (0001) substrate, we have found three types of sites known as the *top* site which is the first cobalt layer, the second position of the cobalt layer is the *hcp* site and the *fcc* site at the hollow. We have adsorbed graphene who has two *C* atoms, in those sites or between them, consequently, we got six possibility of configurations, namely : *top-fcc*, *top-hcp*, *hcp-fcc*, and *bridge-top*, *bridge-fcc*, *bridge-hcp*, as shown in Figures 3.5.

- *top-fcc* structure, the atoms of graphene are situated one above the *top* site and a second above the *fcc* site (see Figure 3.5 a).

- *top-hcp* structure, one atom stays on the *top* site, but the other atom is on the *fcc* site (see Figure 3.5 b).

- *hcp-fcc* structure, the atoms are placed on *hcp* and *fcc* sites (see Figure 3.5 c).

- *bridge-top* structure is described by located one atom between the sites *top* and *fcc* and the second one between the sites *top* and *hcp* (see Figure 3.5 d).

- *bridge-fcc* structure, placing one (second) atom between *fcc* and *hcp* (*fcc* and *top*) sites (see Figure 3.5 e).

- *bridge-hcp* structure, one (second) atom is situated between the sites *hcp* and *top* (*hcp* and *fcc*)(see Figure 3.5 f).
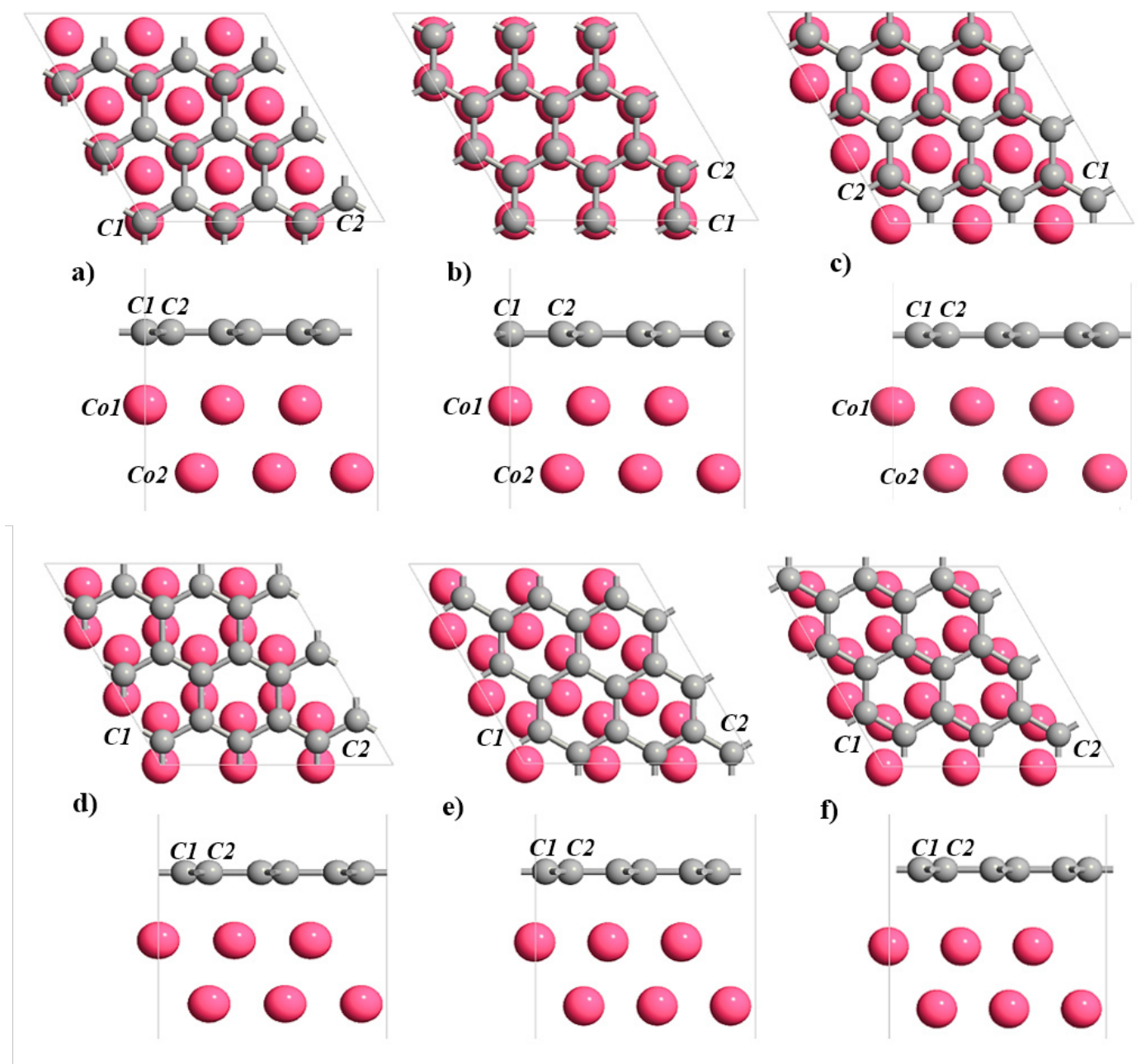
Figure 3.5: Top and side views of all configurations of monolayer graphene adsorbed on Co(0001) surface (a) *top-fcc*, (b) *top-hcp*, (c) *hcp-fcc*, (d) *bridge-top*, (e) *bridge-fcc*, and (f) *bridge-hcp*. Pink color is for cobalt *Co* atoms and grey color is for carbon *C* atoms.

To check the stability of the graphene/Co(0001) system , we have calculated the binding energy (E_B) which is defined as the extent to which graphene is bound to the Co surface and is given by the following expression:

$$E_B = E_{\text{graphene/Co(0001)}} - \left(E_{\text{graphene}} + E_{\text{Co(0001)}} \right) \tag{3.2}$$

where $E_{\text{graphene/Co(0001)}}$ is the energy of the interface system and E_{graphene} and $E_{\text{Co(0001)}}$ are the energies of pure graphene and *Co* surface, respectively.

The binding energy (E_B), the distances (D) of the carbon atoms from the *Co* surface and the optimized lattice parameter a for the 6 possible configurations are reported in Table 3.3, along with calculated and experimental values [KJBG12, TNMY13, SŽA+14, VD11, EPR+09, KGK+07, OYMT11, ASBZ13] for some configurations, issued from literature, for comparison.

From the calculated binding energy (E_B) we obtain the following stability order of the six configurations: *bridge-hcp < bridge-fcc < hcp-fcc < bridge-top < top-hcp < top-fcc*, We find two more stable configurations that are *top-fcc* of value -0.184 eV per *C* atom and *top-hcp* of value -0.177 eV per *C* atom, also observed in [SŽA+14, TNMY13, KJBG12, OYMT11].

The distances (D) between graphene and Co(0001) are calculated, the smallest value (2.1 Å) for *top-fcc*, *top-hcp* and *bridge-top* configurations, which is in good agreement with the theoretical [KJBG12, TNMY13, SŽA+14, VD11, KGK+07, OYMT11, ASBZ13] and the experimental [EPR+09] values, and the biggest value (3.5 Å) for *hcp-fcc* is in line with [KJBG12, VD11]. Moreover, the *bridge-fcc* and *bridge-hcp* configurations have an average value 2.9 Å (see Table 3.3).

It should be noted that E_B decreases when D increases due to the reduction of the interaction between the graphene sheet and the cobalt surface.

We find that the lattice parameter (a), for the two more stable configurations, has a value of about 2.48 Å and approximately 2.46 Å for the rest of the other configurations (see Table 3.3). These values agree well with [TNMY13, KJBG12, SŽA+14, OYMT11, KGK+07].

Table 3.3: Binding energy (E_B) (from Eq.3.2) per carbon atom, the distances (D) between graphene and Co(0001), and lattice parameter (a) for the monolayer graphene on Co(0001) substrate.

Monolayer structures	D (Å)	E_B (eV)	a (Å)
top-fcc	2.109	-0.184	2.477
	2.09[a]	-0.22[a]	2.50[a]
	2.00[b]	-0.207[b]	2.52[b]
	2.154[c]	-0.077[c]	2.46[c]
	2.155/2.137[d]		
	1.5-2.2[e]		
top-hcp	2.109	-0.177	2.476
	2.04[f]	-0.32[f]	2.506[f]
	2.07[a]	-0.077[c]	2.50[a]
	2.30[g]	-0.086[g]	2.51[g]
	2.155/2.138[d]		
	2.12[h]		
hcp-fcc	3.534	-0.104	2.455
	3.08[a]		2.50[a]
	3.639[d]		
bridge-top	2.196	-0.143	2.461
bridge-fcc	2.938	-0.092	2.463
bridge-hcp	2.934	-0.091	2.463

[a] Ref. [KJBG12] [b] Ref. [TNMY13] [c] Ref. [SŽA⁺14]
[d] Ref. [VD11] [e] Ref. [EPR⁺09] [f] Ref. [KGK⁺07]
[g] Ref. [OYMT11] [h] Ref. [ASBZ13]

3.6.2   Magnetic Properties

The magnetic moment (m) was calculated for the two stable configurations *top-fcc* and *top-hcp*, they are listed in Table 3.4. For the *top-fcc* configuration, we got -0.041 μ_B for the *top-C* atom (*C1*), that leads to an antiferromagnetic coupling to the *Co* atoms, and 0.040 μ_B for the *fcc-C* atom (*C2*), indicating ferromagnetic coupling with the *Co* atoms. As for the *top-hcp* configuration, we obtain -0.044 μ_B and 0.045 μ_B for the *top-C* atom (*C1*) and *hcp-C* atom (*C2*) respectively. We note the reduction of the magnetic moment induced by the surface cobalt atom (*Co1*) which is in contact with the graphene layer. For the case of *top-fcc* we find $m = 1.52$ μ_B and is reduced to 12% and for *top-hcp* $m = 1.50$ μ_B and is reduced to 13%, that compared with the clean surface (*Co5*), which has 1.72 μ_B. Our values confirm the previous results [KJBG12, SŽA⁺14, VD11, ASBZ13].

Table 3.4: Magnetic moment (m) given by μ_B for the non-equivalent graphene atoms (*C1* and *C2*) and of the cobalt atoms in each layer for the two most stable configurations of the monolayer graphene/Co(0001) interface.

Atoms	top-fcc	top-hcp
C1	-0.041	-0.044
	-0.043[a]	-0.048[a]
	-0.040[b]	
	-0.083[c]	
C2	0.040	0.045
	0.038[a]	0.044[a]
	0.040[b]	
	0.056[c]	
	0.05-0.1[d]	
Co1	1.522	1.501
	1.54[a]	1.496[a]
	1.50[b]	
	1.54[c]	
	1.59[e]	
Co2	1.562	1.578
	1.54[b]	
	1.75[e]	
Co3	1.568	1.583
	1.54[b]	
	1.74[e]	
Co4	1.640	1.641
	1.61[b]	
	1.75[e]	
Co5	1.716	1.718
	1.68[b]	
	1.78[c]	
	1.81[e]	

[a] Ref. [VD11]
[b] Ref. [SŽA$^+$14]
[c] Ref. [KJBG12]
[d] Ref. [WRH$^+$10]
[e] Ref. [ASBZ13]

3.6.3   Electronic Properties

3.6.3.1   Density of States

In order to better understand the origin of the induced magnetic moment for C atoms, we have calculated the projected density of states (**PDOS**) of the most stable *top-fcc* and *top-hcp* configurations, PDOS plots of each of the *fcc-C*, *hcp-C* and *top-C* atoms, in addition to the interface layer (*Co1*), with graphene sheet and the clean surface of the cobalt(0001) (*Co-free*) are displayed in Figure 3.6.

Our results show that the C atoms acquired spin polarization and split into up and down spins bands. On the other hand, the PDOS of the contact layer (*Co1*) decreases, which is due to the interaction between the cobalt substrate and the graphene sheet and the resulting hybridization between Co and C electronic orbitals. These results in complete agreement with [KJBG12, SŽA$^+$14, VD11].
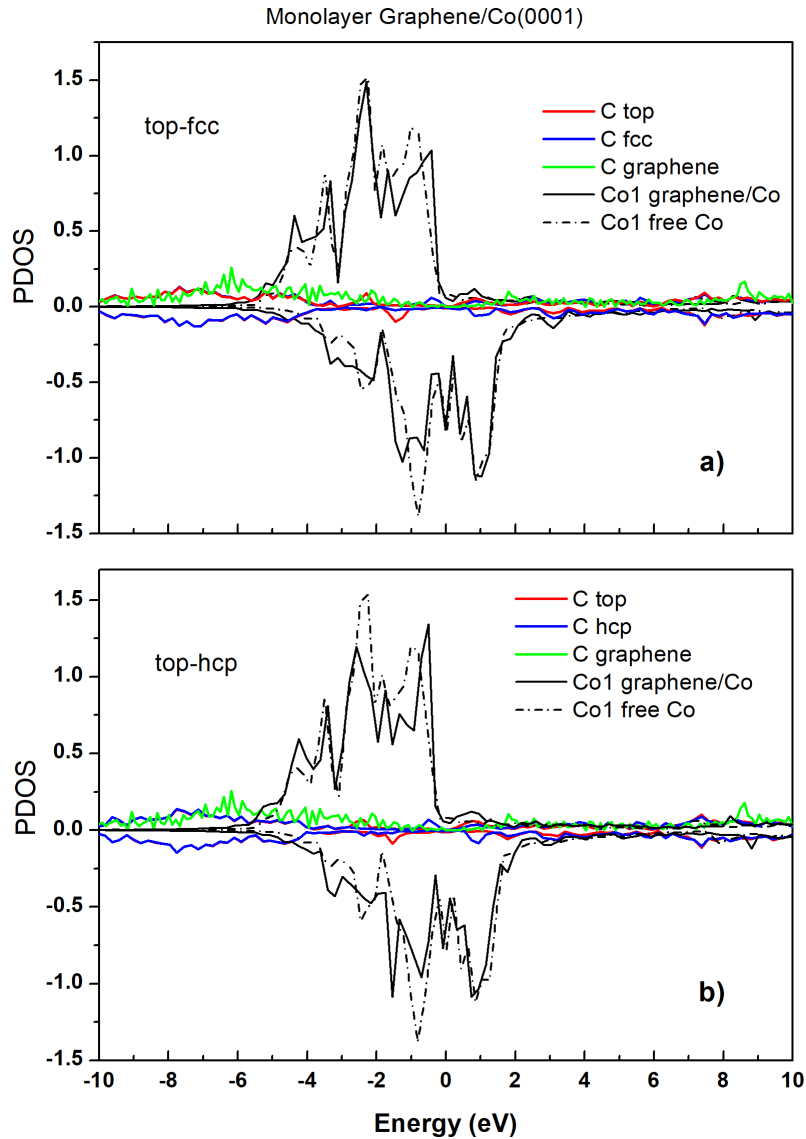
Figure 3.6: PDOS calculations for *top-fcc* (a), *top-hcp* (b) configurations of monolayer graphene on Co(0001).

3.6.3.2 Band Structure

From the calculation of the band structure (**BS**) (Figure 3.7), we observe the destruction of the Dirac cone at K point and the opening of the band-gap by 0.43 eV for the majority channel (spin-up) and 0.32 eV for the minority channel (spin-down), which returns to the strong hybridization that occurred between the out-of-plane p_z orbital (*top-C* atom, because the *fcc-C* atom occupying the hollow site for the Co surface) of graphene with the topmost layer d_{z^2} orbital of cobalt substrate. These results agree with previously measured and calculated values [KJBG12, SŽA$^+$14, VD11].
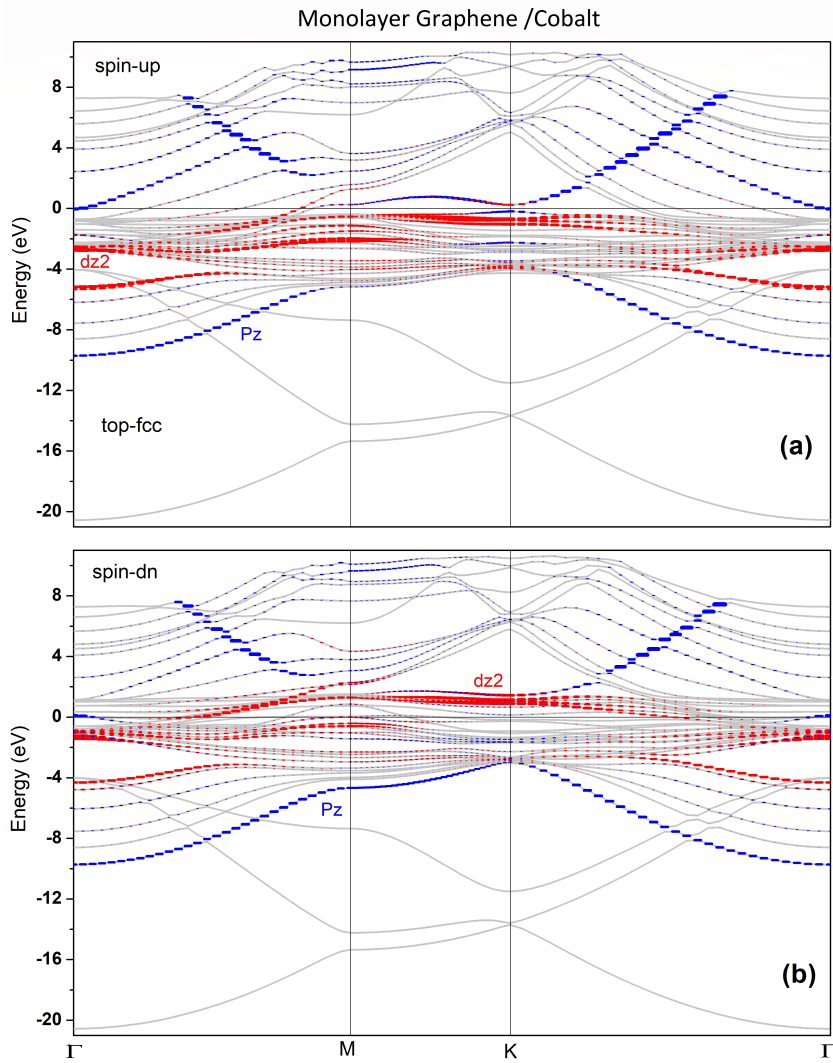
Figure 3.7: Calculated band structures for spin-up (a), spin-down (b) for monolayer graphene on Co(0001) for the most stable *top-fcc* configuration. Blue lines represent the p_z orbitals of the π-band and the red lines the d_{z^2} orbitals of cobalt.

3.6.3.3 Charge Transfer

Hybridization is a direct result of charge transfer, to understand this we plotted the charge density difference and used the Badar charge analysis, where the charge transfer is determined by the difference in the charge density between the system and its components, it is presented by:

$$\Delta\rho^\sigma = \rho^\sigma_{\text{graphene/Co}} - \rho^\sigma_{\text{Co}} - \rho^\sigma_{\text{graphene}} \tag{3.3}$$

Where σ denotes spin-up or spin-down, $\rho_{\text{graphene/Co}}$ the charge density of the full system (interface), ρ_{Co} and ρ_{graphene} are the charge density of a clean cobalt surface and the charge density of pure graphene, respectively.

In Figure 3.8 we show a charge transfer from *Co* substrate to graphene in the case of the *top-fcc* structure. It can be observed a clear difference in the charge redistribution for the spin-up and the spin-down parts. For the spin-up part, a slight accumulation on the *fcc-C* atoms (*C2*) and deficient for the cobalt surface (Figure 3.8 a) are noticed. It means that there is the transfer of spin-up electrons the *Co* atoms to the *fcc-C* atoms. For the spin-down, we have seen an excess charge accumulation between the cobalt surface atoms and the *top-C* atoms (*C1*) (Figure 3.8 b). The net effect of the spin-polarized charge transfer is shown in Figure 3.8 c. The spin-up (-down) electrons are accumulated on the *fcc-C* (*top-C*) atoms, resulting in magnetic moment on the *fcc-C* (*top-C*) atoms and to parallel (antiparallel) alignment with the contact *Co1* atoms.
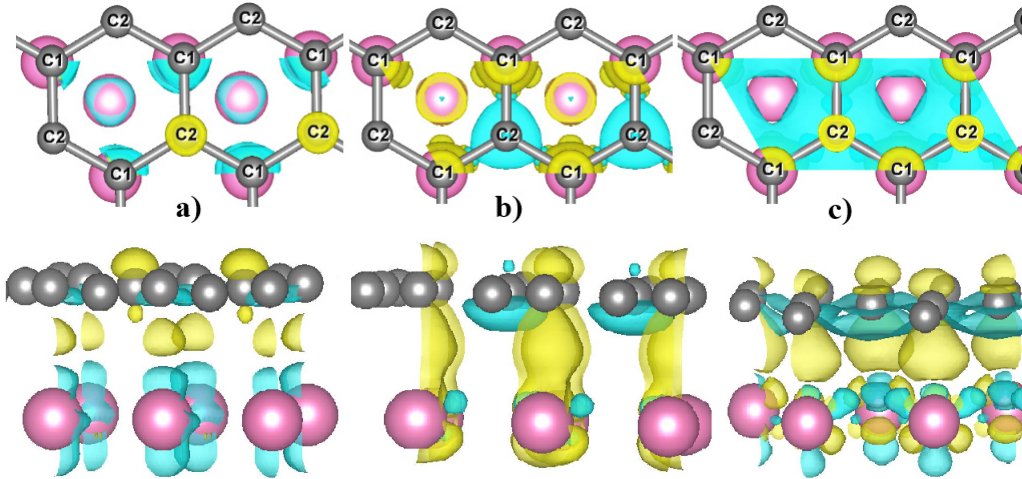
Figure 3.8: Illustration of the charge distribution for the *top-fcc* configuration of monolayer graphene on Co(0001). a) spin-up, b) spin-down and c) total charge. Grey (Pink) color represents the carbon *C* (cobalt *Co*) atoms. Yellow (bleu-green) color represents the accumulation (deficient) charges.

Based on the Bader charges analysis, we found that the *top-C* and *fcc-C* atoms gain $0.06e$ and $0.05e$ respectively, the contact surface (*Co1*) lose $0.13e$, while the second layer *Co* surface atoms (*Co2*) are slightly affected (i.e. a part of the charge of the electrons of the *Co* surface atoms is were transferred to the graphene *C* atoms). These results indicate graphene's ability to be magnetic, in line with results reported in literature [YH07, ZWS$^+$09, CWYL14, MBB$^+$20, LKWVW16, LWW$^+$15, WTS$^+$15].

Table 3.5: Bader charges of the non-equivalent atoms (*C1* and *C2*) of the first graphene layer and the cobalt atoms of the first and second layer (*Co1* and *Co2*).

Configurations	C1	C2	Co1	Co2
top-fcc	-0.064	-0.054	0.13	0.0088
	-0.04[a]	-0.04[a]	0.13[b]	
top-hcp	-0.053	-0.065	0.124	0.0014

[a] Ref. [ASBZ13]   [b] Ref. [VD11]

3.7 Bilayer Graphene/Co(0001) Interface

3.7.1 Structural Properties

In this section, we adsorbed bilayer graphene on Co(0001), when adding the second graphene layer the number of possible configurations is doubled (i.e, each monolayer structure, has the possibility of forming two configurations of the bilayer structure) for example, the *top-fcc* monolayer structure is the same first layer for the bilayers structure and the second layer is either *hcp-fcc* or *top-hcp*. We applied the same rule to the other monolayer structures, we found 12 configurations for the bilayer structure, four of them (the most stable) are shown in Figures 3.9 a-d.
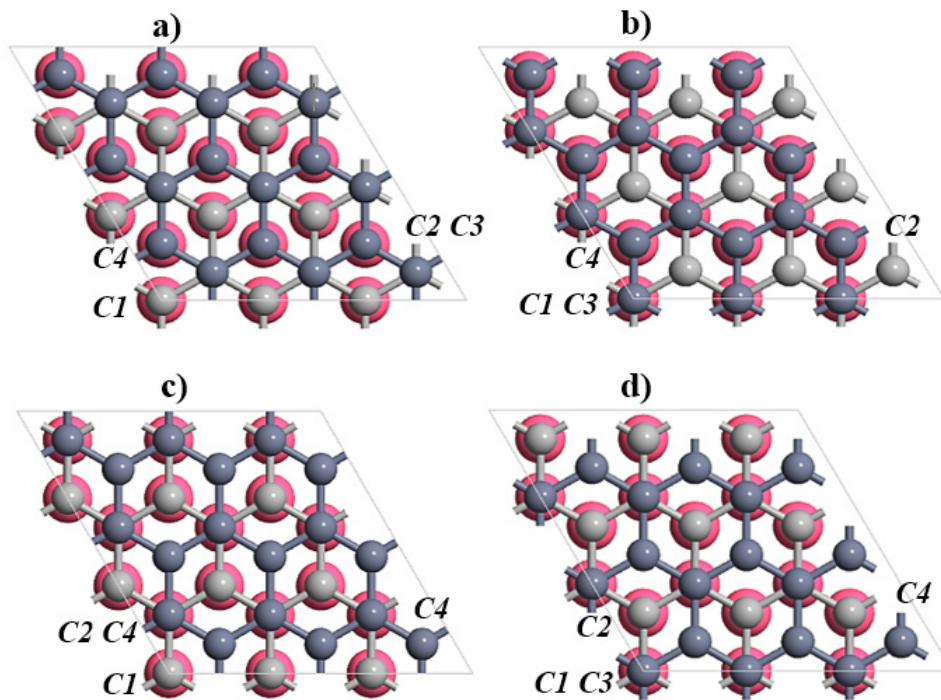
Figure 3.9: Top view of the 4 most stable configurations of bilayer graphene adsorbed on Co(0001) surface: a) *hcp-fcc/top-fcc/Co* , b) *top-hcp/top-fcc/Co*, c) *hcp-fcc/top-hcp/Co* and d) *top-fcc/top-hcp/Co*. Pink color is for *Co* atoms; light and dark gray colors are for the adsorbed (first layer) and the second layer of graphene atoms, respectively.

We calculated the binding energy (E_B), the intralayer distance (d) of graphene and the distance (D) between the Co(0001) surface and the first graphene layer for the different configurations of the bilayer interface structures, which are listed in Table 3.6. Four configurations were found to have E_B -0.11 eV/C, whose the first layers (either *top-fcc* or *top-hcp*) are the most stable configurations in the monolayer case, they are described as follows: two configurations where the *top-fcc* is the first layer and second layer it is either *top-hcp* or on *hcp-fcc* (Figures 3.9 a,b), and the remaining two ones are described as the first layer is *top-hcp*, and *top-fcc* or *hcp-fcc* for the second layer (Figures 3.9 c,d).

The distance values (D) obtained for more stable configurations ($\sim$ 2.10 Å) are very close compared to those calculated in the monolayer case of graphene, the relatively small distance between graphene and the top layer of *Co* surface is probably due to the intermixing of the electronic states of both materials. The graphene intralayer distance d varies slightly from one configuration to another and ranges from of 3.286 Å to 3.446 Å, which is in line with the value found in the literature of 3.35 Å [SMMB08, OHL$^+$08, LA08, CJKK08].

Table 3.6: Binding energy (E_B) per carbon atom, distances (D) between the first layer of graphene and the surface layer of cobalt, distance (d) of intralayer (between the two graphene layers) for the all possible configurations of the bilayer graphene/Co(0001) interface.

Configurations structures	E_B (eV)	d (Å)	D (Å)
top-hcp/top-fcc/Co	-0.113	3.287	2.101
hcp-fcc/top-fcc/Co	-0.114	3.352	2.099
top-fcc/top-hcp/Co	-0.110	3.298	2.101
hcp-fcc/top-hcp/Co	-0.111	3.350	2.097
top-fcc/hcp-fcc/Co	-0.061	3.286	3.501
top-hcp/hcp-fcc/Co	-0.061	3.291	3.485
Bridge-top-1	-0.097	3.345	2.157
Bridge-top-2	-0.097	3.405	2.102
Bridge-fcc-1	-0.099	3.392	2.115
Bridge-fcc-2	-0.096	3.354	2.147
Bridge-hcp-1	-0.101	3.342	2.137
Bridge-hcp-2	-0.089	3.446	2.111

3.7.2   Magnetic Properties

The magnetic moments values for the most stable structures are reported in Table 3.7. The *top-C* atom (*C1*) of the first layer adsorption owns a magnetic moment of -0.04 μ_B and is aligned antiparallel to the *Co* atom, as in a graphene monolayer. The second atom (*C2*) which lies in the same layer (adsorption layer) is located on the *fcc* and *hcp* sites, has a magnetic moment of about 0.04 μ_B aligned parallel to cobalt, which also corresponds to the case of monolayer. The same behaviour for the *C3* and *C4* atoms is observed. The magnetic moment of the cobalt surface *Co1* (the contact layer with graphene) is reduced to 1.50-1.52 μ_B (reduction about 12.8-11.6 %). In contrast, the fifth layer (the free surface) was not affected by the presence of graphene and keep a high magnetic moment (1.72 μ_B). The magnetic moment of graphene is limited to the first layer (the adsorbent layer) while the second layer do not contribute significantly. Due to the strong interaction that occurs between the topmost cobalt layer (*Co1*) and the adsorbed layer, while graphene interlayers interaction is weak.

Table 3.7: Magnetic moments (*m*) by μ_B of the non-equivalent carbon atoms (*C1* and *C2*) of the first graphene layer, (*C3* and *C4*) of the second graphene layer and of the cobalt, in each layer, for the four most stable configurations of the bilayer graphene/Co(0001) interface. The sites of the *C* atoms in the four configurations are C3-C4/C1-C2/Co(0001).

Atoms	top-hcp/ top-fcc/Co	hcp-fcc/ top-fcc/Co	top-fcc/ top-hcp/Co	hcp-fcc/ top-hcp/Co
C4	0.001	0.006	0.002	0.005
C3	0.002	-0.003	0.002	-0.004
C2	0.041	0.037	0.046	0.042
C1	-0.041	-0.039	-0.044	-0.043
Co1	1.519	1.514	1.502	1.495
Co2	1.562	1.561	1.574	1.572
Co3	1.573	1.572	1.580	1.580
Co4	1.642	1.642	1.639	1.639
Co5	1.717	1.718	1.717	1.717

3.7.3 Electronic Properties

3.7.3.1 Density of Sates

Figure 3.10 exhibits the DOS of the two configurations *top-hcp/top-fcc/Co* and *hcp-fcc/top-fcc/Co*. The splitting of the *top* (*C1*) and *fcc* (*C2*) atoms to spin-up and spin-down appears as in the case of monolayer graphene. A same behaviour is observed for the *C3* and *C4* atoms. As observed in the case of single graphene layer, a slight reduction of DOS is noticed for the cobalt atoms in presence of graphene denoting a charge transfer from *Co* atoms to *C* atoms.
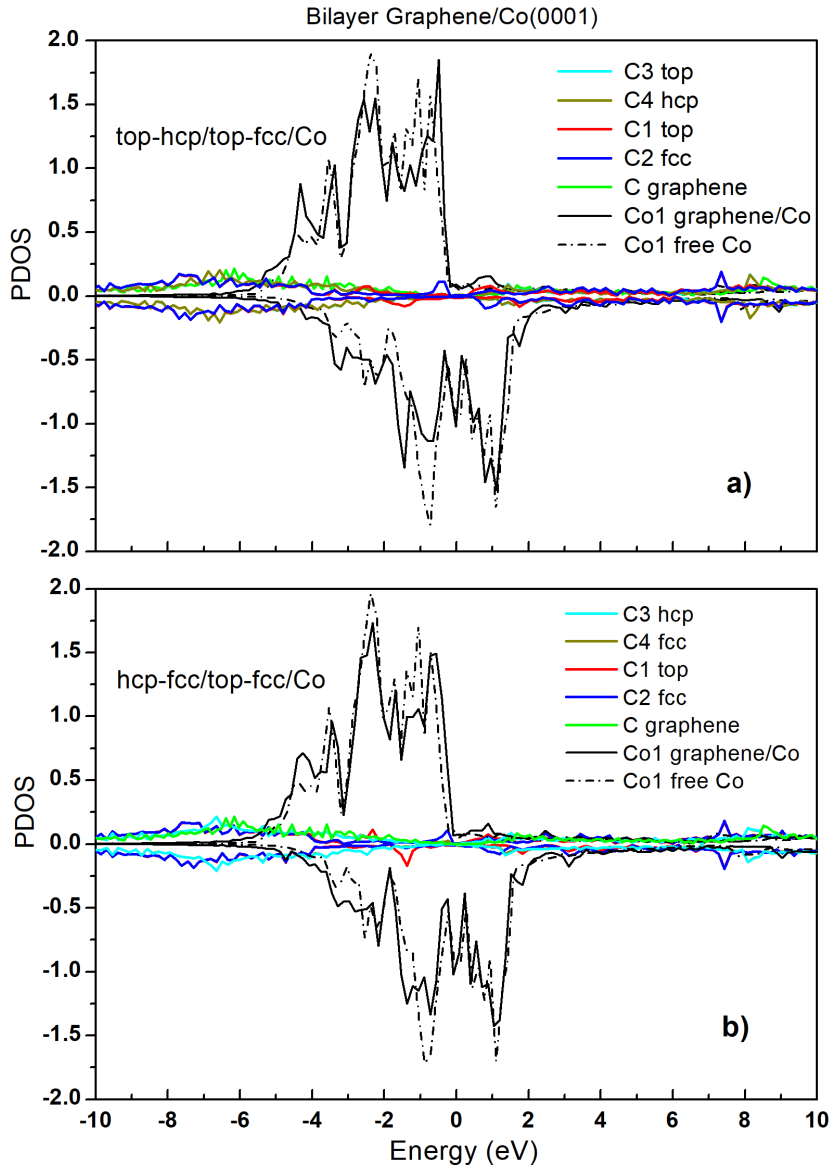
Figure 3.10: PDOS calculations for *top-hcp/top-fcc/Co* (a), *hcp-fcc/top-fcc/Co* (b) configurations of bilayer graphene on Co(0001).

3.7.3.2   Band Structure

Figure 3.11 displays the BS of the spin-up and the spin-down for the *hcp-fcc/top-fcc/Co* configuration. We notice an increase in the gap of about 0.5 eV for the spin-up band, slightly larger than that determined in the monolayer case. For the spin-down band, we observe a Dirac cone at K point below the Fermi level with a small gap about 0.11 eV, with remaining hybridization occuring between p_z orbitals of graphene and metallic d_{z^2} orbitals of cobalt.
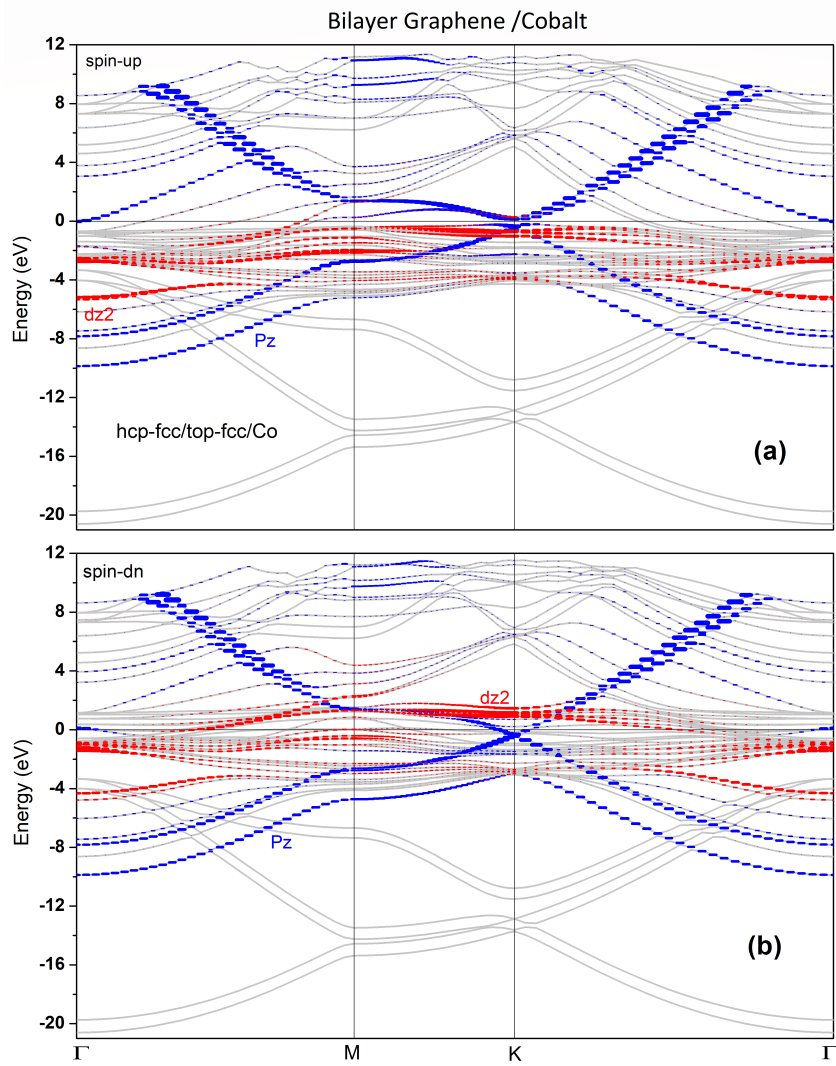
Figure 3.11: Calculated band structures for spin-up (a), spin-down (b) for bilayer graphene on Co(0001) for the most stable *hcp-fcc/top-fcc/Co* configuration. Blue lines represent the p_z orbitals of the π band and the red lines the d_{z^2} orbitals of cobalt.

3.7.3.3 Charge Transfer

Bader's charge transfer analysis of the two configurations *top-hcp/top-fcc/Co* and *hcp-fcc/top-fcc/Co* is mentioned in Table 3.5. The first layer graphene atoms *C1* and *C2* show approximately of the same behaviour as in the case of monolayer graphene adsorption, 0.07-0.06 electrons are gained respectively. Moreover, we find that the atoms of second graphene layer (*C3* and *C4*) slightly contributes. Conversely, the *Co* atom of the contact surface (*Co1*) lose 0.12-0.14 electrons and the layer adjacent to the contact layer is also slightly affected (low contribution).

Table 3.8: Bader charges of the non-equivalent carbon atoms (*C1* and *C2*) of the first graphene layer, (*C3* and *C4*) of the second graphene layer as well as of the cobalt atoms of the first and second layer (*Co1* and *Co2*).

Configurations	C1	C2	C3	C4	Co1	Co2
top-hcp/ top-fcc/Co	-0.069	-0.060	-0.0012	-0.0011	0.140	0.0054
hcp-fcc/ top-fcc/Co	-0.058	-0.057	-0.0016	-0.0016	0.124	0.0003

3.8 Monolayer *h*-BN/Co(0001) Interface

3.8.1 Structural Properties

In this study, we will adsorb a hexagonal boron nitride (*h*-BN) sheet on the Co(0001) surface. With the possibility of exchanging N and B atoms from their sites, we found 12 configurations, six of them are shown in Figures 3.12.

Table 3.9 illustrates the binding energies (E_B), the distances (D_N) and (D_B) between N and B atoms with the *Co1* layer and the lattice parameter (a) for all configurations. From the binding energy, four more stable configurations were obtained, the first two configurations *top(N)-hcp(B)* and *top(N)-fcc(B)* (Figures 3.12 a and b) having a value equals to -0.222 eV per *BN* pair and the two other are the bridge configurations (*bridge-top*) N (or B) *top-hcp* with B (or N) *top-fcc* (Figure 3.12 d) have a binding energy of -0.215 (-0.213) eV per BN pair. Our findings are well supported by refs. [ZZG11, JG13, OSKH13]. The parameter (a) varies from one configuration to another and ranges from 2.472 to 2.503 Å close to that reported in [SHJ+10].
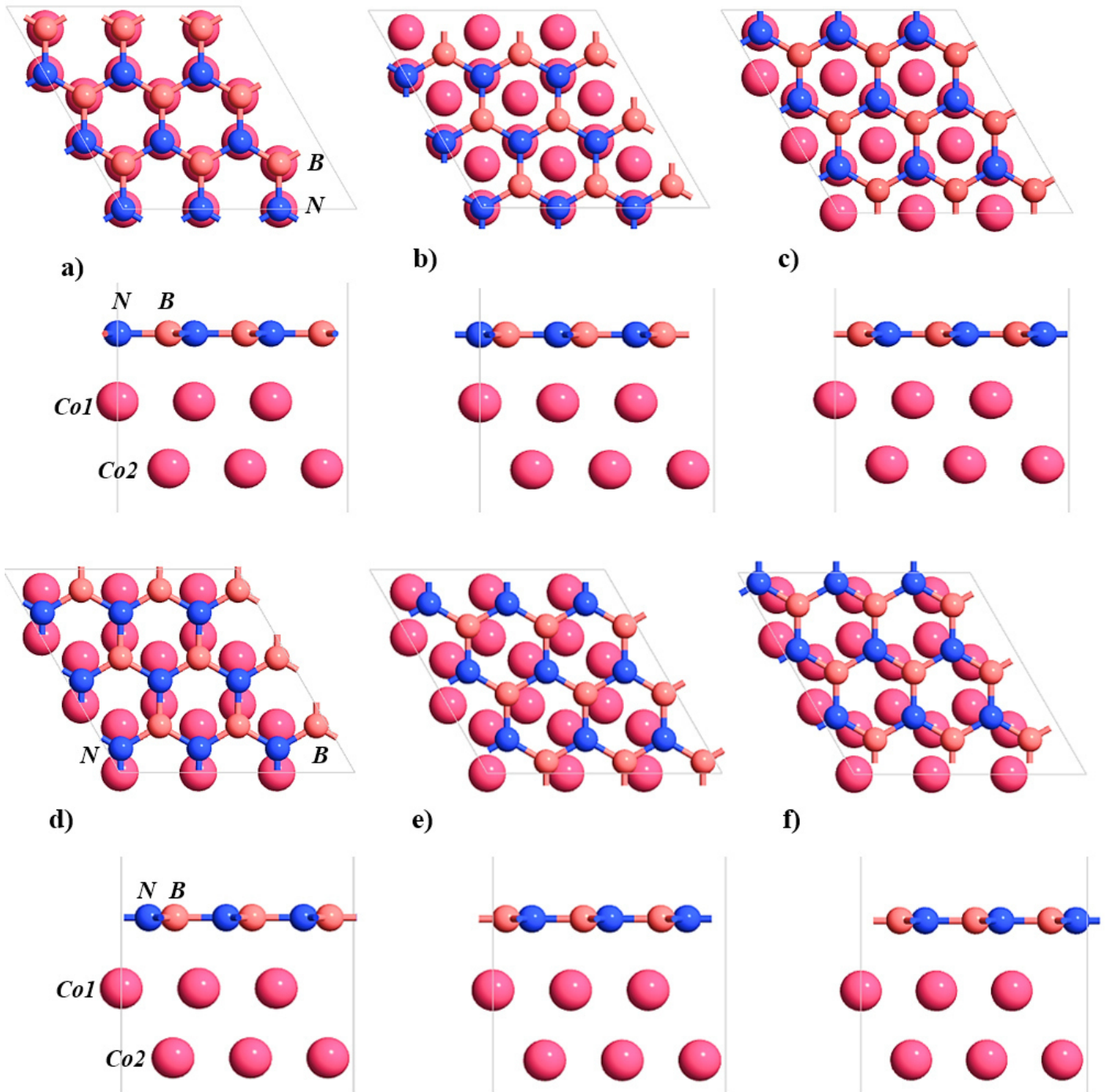
Figure 3.12: Top and side views of the 6 configurations of monolayer *h*-BN adsorbed on Co(0001) surface (a) *top(N)-fcc(B)*, (b) *top(N)-hcp(B)*, (c) *hcp(N)-fcc(B)*, (d) *bridge-top: N(top-hcp)* and *B(top-fcc)*, (e) *bridge-fcc: N(hcp-fcc)* and *B(top-fcc)*, and (f) *bridge-hcp: N(top-hcp)* and *B(hcp-fcc)*. Pink color is for cobalt *Co* atoms, blue and light brick colors are for Nitrogen *(N)* and Boron *(B)* atoms respectively.

The variance is shown in the value of the distance between nitrogen (N) and boron (B) atoms with the *Co* surface, in the more stable configurations we find about 2.13 Å for the D_N and 2.00 Å for the D_B, indicating that the N atom is moving away from the surface of Co (0001), while the B atom is moving towards the cobalt surface, where leads to the chemisorbed interaction (strong bound). Our results are in line with [ZZG11, JG13, LBS08, TVW$^+$16, KNS15].

Table 3.9: Binding energy (E_B) per BN pair, the distances of the N (D_N) and B (D_B) atoms with the *Co* surface, and lattice parameter (a) for the 12 configurations of the monolayer *h*-BN on Co(0001) substrate.

	top-hcp		**top-fcc**		**hcp-fcc**	
	top(N)-hcp(B)	top(B)-hcp(N)	top(N)-fcc(B)	top(B)-fcc(N)	hcp(N)-fcc(B)	hcp(B)-fcc(N)
a (Å)	2.492	2.479	2.495	2.472	2.474	2.474
E_B **(eV)**	-0.222 -0.501[a] -0.73[b]	-0.048 -0.04[a] -0.42[b]	-0.222 -0.509[a] -0.73[b]	-0.090 -0.108[a] -0.42[b]	-0.082 0.206[a] -0.44[b]	-0.082 0.294[a] -0.44[b]
D_N **(Å)**	2.126 2.113[a]	3.333 2.809[a]	2.133 2.082[a] 2.11[b] 2.15[c] 2.10[d]	2.786 2.791[a]	3.141	3.137
D_B **(Å)**	2.004 2.015[a]	3.318 2.786[a]	2.006 1.988[a] 1.99[b] 2.03[c] 1.98[d]	2.763 2.750[a]	3.141	3.126
	Bridge-top		**Bridge-hcp**		**Bridge-fcc**	
	N(top-fcc) B(top-hcp)	B(top-fcc) N(top-hcp)	N(top-hcp) B(hcp-fcc)	B(top-hcp) N(hcp-fcc)	N(hcp-fcc) B(top-fcc)	B(hcp-fcc) N(top-fcc)
a (Å)	2.503	2.500	2.491	2.500	2.491	2.498
E_B **(eV)**	-0.213	-0.215	-0.205	-0.071	-0.072	-0.210
D_N **(Å)**	2.118	2.123	2.135	2.877	2.796	2.595
D_B **(Å)**	1.997	2.005	2.017	2.855	2.767	2.549

[a] Ref. [ZZG11]   [b] Ref. [JG13]   [c] Ref. [LBS08]   [d] Ref. [TVW$^+$16]

3.8.2 Magnetic Properties

From studying the magnetic properties of the most stable configurations, an induced magnetic moment was observed on the *h*-BN sheet. We find that the *N* atoms acquire a moment of 0.01 μ_B aligned parallel with the *Co* atom, while the *B* atoms acquire a magnetic moment of -0.02 μ_B aligned antiparallel to the *Co* atom (Table 3.10). The magnetic moment for the *Co* surface atoms decreases to 1.56 μ_B (a decrease of 9.8 %) compared to 1.73 μ_B for the clean surface (*Co5*). These values concurred well with [JG13] and also confirms our earlier ones.

Table 3.10: Magnetic moment (m) given by μ_B of the *h*-BN sheet and of the cobalt atoms in each layer for the 4 most stable configurations of the monolayer *h*-BN/Co(0001) interface.

Atoms	top-hcp	top-fcc	Bridge-top	
	top(N)-hcp(B)	top(N)-fcc(B)	N(top-fcc) B(top-hcp)	B(top-fcc) N(top-hcp)
B	-0.020	-0.020 -0.06[a]	-0.022	-0.021
N	0.012	0.013 0.02[a]	0.010	0.012
Co1	1.552	1.559 1.56[a]	1.551	1.563
Co2	1.605	1.597	1.602	1.597
Co3	1.610	1.608	1.602	1.599
Co4	1.655	1.654	1.655	1.652
Co5	1.728	1.726 1.69[a]	1.731	1.728

[a] Ref. [JG13]

3.8.3 Electronic Properties

3.8.3.1 Density of States

Figure 3.14 shows the *PDOS* of the *h*-BN on Co(0001) for the *top(N)-hcp(B)* and *top(N)-fcc(B)* configurations. We see a splitting of the electronic states of the *N* and the *B* atoms of the interface to a spin-up and spin-down states as well as a clear decrease of the electronic states of the cobalt contact layer (*Co1*) compared with the clean *Co* surface. This explains the existence of an hybridization between the *h*-BN sheet electronic states and the *Co* substrate electronic states. Our results are in good agreement with ref. [LBS08].
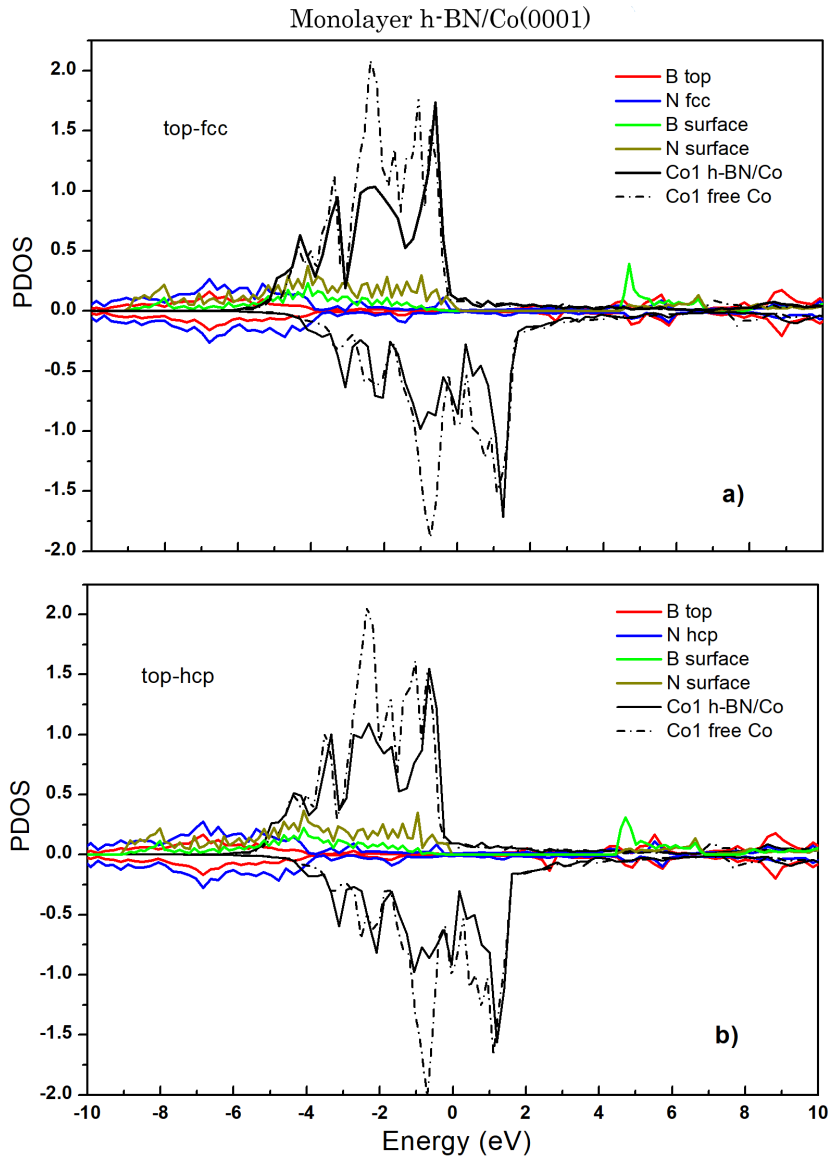
Figure 3.13: PDOS calculations for *top(N)-fcc(B)* (a), *top(N)-hcp(B)* (b) configurations of monolayer *h*-BN on Co(0001).

3.8.3.2 Band Structure

The plot in Figure 3.14 is the band structure of the spin-up and the spin-down channels for the *top(N)-hcp(B)* configuration. We noted that the characteristic gaping structure of *h*-BN free-standing is kept at the region of *K*-point, in the inside this gap, the *N* orbital is mixed with the *Co* states, while the contribution of the *B* orbital appears mainly at the local boundary of the band-gap, this contribution between the *h*-BN and Co(0001) substrate is a consequence of the strong interaction that is accompanied by the significant hybridization of the *h*-BN $\pi(p_z)$ and the d_{z^2} *Co* states [JG13, TVW$^+$16, UTB$^+$18].
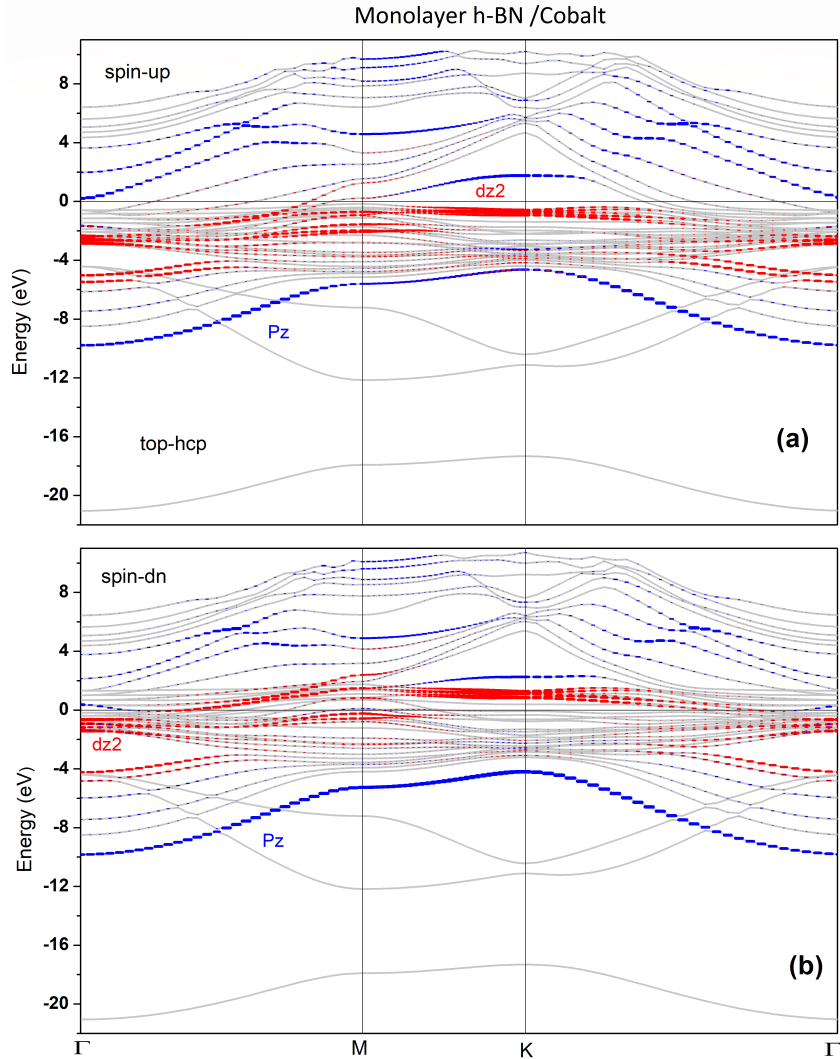
Figure 3.14: Calculated band structures for spin-up (a), spin-down (b) for monolayer *h*-BN on Co(0001) for the most stable *top(N)-hcp(B)* configuration. Blue lines represent the p_z orbitals of the π-band and the red lines the d_{z^2} orbitals of cobalt.

3.8.3.3 Charge Transfer

The *p-d* hybridization leads to charge transfer between the *h*-BN and the *Co* substrate, this is exhibited for Figure 3.15. We observe for the spin-up that there is a charge accumulation on *N* atoms and a deficiency in the surface *Co* atoms (Figure 3.15 a). This is the result of donating electrons from *Co* to *N* atoms. As for the spin-down, there is a clear accumulation on *B* atoms regarding to the cobalt surface (Figure 3.15 b). The combined effect of electron transfer of spin channels is illustrated by the total charge (Figure 3.15 c).
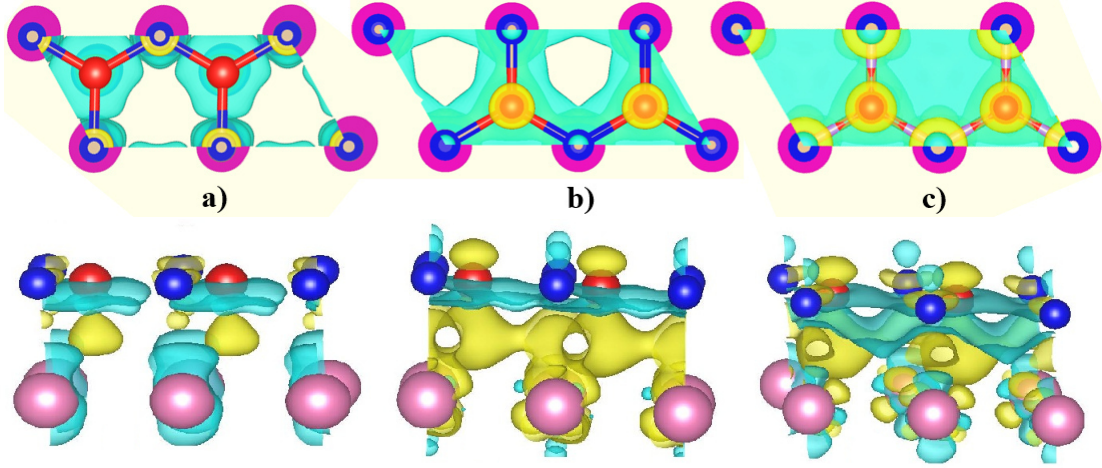
Figure 3.15: Illustration of the charge distribution for the *top(N)-hcp(B)* configuration of monolayer *h*-BN on Co(0001). a) spin-up, b) spin-down and c) total charge. Red (*B* atoms), Blue (*N* atoms) and Pink (*Co* atoms). Yellow (bleu-green) color represents the accumulation (deficient) charges.

We have performed an analysis based on charges calculated within the Bader's method. From calculation, *B* (*N*) atom gains 0.09 (0.02) electrons, and cobalt loses about 0.12 electrons. Therefore, the *B* atom becomes negatively charged and thus is attracted towards the least negatively charged *Co* surface and vice versa for the *N* atom, causing the *h*-BN sheet to buckle. The results of our study are positively related to previously published works [JG13, ZZG11].

Table 3.11: Bader charges of the of the *B* and *N* atoms of the first graphene layer and the cobalt atoms of the first and second layer (*Co1* and *Co2*).

Configurations	N	B	Co1	Co2
top(N)-fcc(B)/Co	-0.020	-0.09	0.121	-0.007
	-0.113[a]	-0.014[a]	0.128[a]	
	0.01[b]	-0.21[b]	0.15[b]	
top(N)-hcp(B)/Co	-0.01	-0.09	0.101	-0.002

[a] Ref. [ZZG11]   [b] Ref. [JG13]

3.9   Bilayer *h*-BN/Co(0001) Interface

3.9.1   Structural Properties

As in the case of the two-layer graphene adsorbed over *Co*, we used a bilayer of *h*-BN with the choice of stacking type AB2' on the surface of cobalt. The total of obtained configurations is 12 structures, the most stable ones are displayed in Figures 3.16 a-d.

The binding energies (E_B), the distances (D_N) and (D_B) are determined for the different configurations (see Table 3.12). We found four (4) stable structures, the lowest binding energy (-0.112 eV per BN pair) are for the configuration [top(N)-fcc(B)] for the first (absorbed) layer with [top(N)-hcp(B)] for the second layer (Figure 3.16 a) and the configuration [top(N)-hcp(B)] for the first (adsorbed) layer with [top(N)-fcc(B)] for the second layer (Figure 3.16 b).
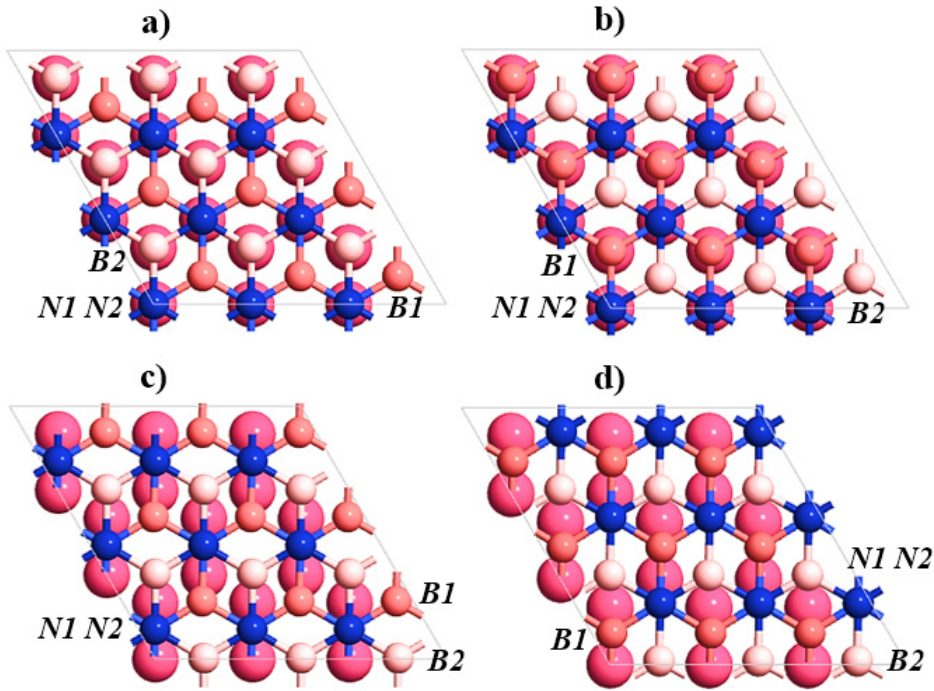
Figure 3.16: Top view of the 4 most stable configurations of bilayer *h*-BN (type AB') adsorbed on Co(0001) surface: a) *top(N)-hcp(B)/top(N)-fcc(B)/Co* , b) *top(N)-fcc(B)/top(N)-hcp(B)/Co*, c) *N(top-hcp)-B(top-top)/N(top-hcp)-B(top-fcc)/Co* and d) *N(top-fcc)-B(top-top)/N(top-fcc)-B(top-hcp)/Co*. The color of the 1st BN (adsorbed) layer is represented by blue for the *N* atom and light brick for the *B* atom, while the 2nd layer for BN corresponds to dark blue and beige for *N* and *B* atoms respectively, *Co* atoms are pink.

The distances between the *Co* surface and *N* and *B* atoms of the *h*-BN sheet are approximately 2.00 and 2.12 Å respectively (Table 3.9), similar with the monolayer case, with a buckling of 0.12 Å. This behavior appears to remain conserved mainly through direct contact of the first *h*-BN layer with the topmost Co layer.

Table 3.12: Binding energy (E_B) per BN pair, the distances of the N (D_N) and B (D_B) atoms from the Co surface, and lattice parameter (a) for the 12 configurations of the bilayer *h*-BN on Co(0001) substrate.

	AB'					
	top-hcp		**top-fcc**		**hcp-fcc**	
1st **layer adsorbed on Co**	top(N)-hcp(B)	top(B)-hcp(N)	top(N)-fcc(B)	top(B)-fcc(N)	hcp(N)-fcc(B)	hcp(B)-fcc(N)
2nd **layer**	top(N)-fcc(B)	hcp(N)-fcc(B)	top(N)-hcp(B)	hcp(B)-fcc(N)	top(B)-hcp(N)	top(B)-fcc(N)
E_B **(eV)**	-0.112	-0.029	-0.112	-0.033	-0.026	-0.026
D_N **(Å)**	2.115	3.164	2.130	3.218	3.096	3.109
D_B **(Å)**	1.996	3.153	2.006	3.208	3.078	3.099
	Bridge-fcc		**Bridge-hcp**		**Bridge-top**	
1st **layer adsorbed on Co**	N(top-hcp) B(hcp-fcc)	N(hcp-fcc) B(top-hcp)	N(top-fcc) B(hcp-fcc)	N(hcp-fcc) B(top-fcc)	N(top-hcp) B(top-fcc)	N(top-fcc) B(top-hcp)
2nd **layer**	N(top-hcp) B(top-fcc)	N(hcp-fcc) B(top-fcc)	N(top-fcc)) B(top-hcp)	N(hcp-fcc) B(top-hcp)	N(top-hcp) B(top-top)	N(top-fcc) B(top-top)
E_B **(eV)**	-0.106	0.001	-0.109	-0.101	-0.110	-0.111
D_N **(Å)**	2.110	2.427	2.123	2.156	2.121	2.116
D_B **(Å)**	1.990	2.363	2.006	2.045	2.004	1.995

3.9.2 Magnetic Properties

Table 3.13 represents the values of the magnetic moments for the 4 most stable configurations. We found that the adsorbed (first) *h*-BN layer has two behaviours, for the *N1* atom it has a moment of about 0.01 μ_B aligned parallel to the *Co* atom; while the *B1* atom has a magnetic moment of about -0.02 μ_B aligned antiparallel to the *Co* atom. The magnetic moment of the surface *Co* atom decreases to 1.55 μ_B (reduction of 10.4 %) compared to that of 1.73 μ_B for the *Co* clean surface. The results obtained are identical with the case of the monolayer *h*-BN. The magnetic moments of the *N2* and *B2* atoms for the second *h*-BN layer were observed to vanish.

Table 3.13: Magnetic moment (m) by μ_B of the *N1* and *B1* atoms of the *h*-BN in the first layer and (*N2*, *B2*) for second layer and the cobalt atoms in each layer for the 4 most stable configurations of the bilayer *h*-BN on Co(0001) substrate. The sites of the *N* and *B* atoms in the four configurations are N2-B2/N1-B1/Co(0001). The *top(N)* means that *N* atom is located on the *top* site and *N(top-fcc)* means that *N* atom is located between *top* and *fcc* sites.

Atoms	top-hcp	top-fcc	Bridge-top	
	top(N)-fcc(B)/ top(N)-hcp(B)/Co	top(N)-hcp(B)/ top(N)-fcc(B)/Co	N(top-hcp)-B(top-top)/ N(top-hcp)-B(top-fcc)/Co	N(top-hcp)-B(top-top)/ N(top-fcc)-B(top-hcp)/Co
B2	0	0	0	0
N2	0	0	0	0
B1	-0.020	-0.020	-0.022	-0.021
N1	0.012	0.013	0.010	0.012
Co1	1.552	1.559	1.551	1.563
Co2	1.605	1.597	1.602	1.597
Co3	1.610	1.608	1.602	1.599
Co4	1.655	1.654	1.655	1.652
Co5	1.728	1.726	1.731	1.728

3.9.3   Electronic Properties

3.9.3.1   Density of states

Figure 3.17 illustrates a study of the density of states for the configurations: *top(N)-fcc(B)/top(N)-hcp(B)/Co* and *top(N)-hcp(B)/top(N)-fcc(B)/Co.* The PDOS of the atoms of the contact layer (*N1* and *B1*) split as in the monolayer *h*-BN case , as well as the one of second layer (*N2* and *B2*) but with less magnitude denoting a major effect limited to the first layer. On another hand, the cobalt atoms PDOS is reduced compared to the one in absence of *h*-BN indicating again charge transfer, mainly between *Co* atoms and *N* and *B* atoms of the first *h*-BN layer in contact with *Co* surface.
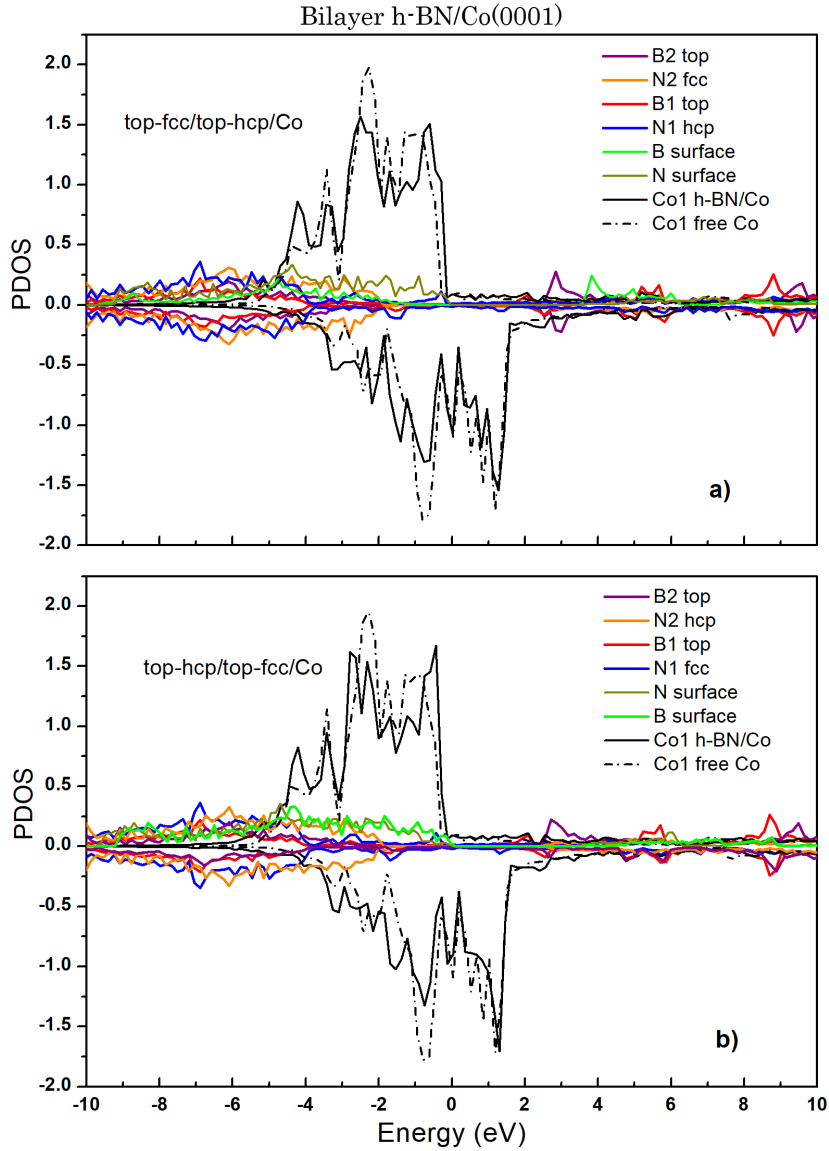
Figure 3.17: PDOS calculations for *top(N)-hcp(B)/top(N)-fcc(B)/Co*(a), *top(N)-hcp(B)/top(N)-fcc(B)/Co* (b) configurations of bilayer *h*-BN on Co(0001).

3.9.3.2 Band Structure

The band structures of spin-up and spin-down for the *top(N)-hcp(B)/top(N)-fcc(B)/Co* configuration are shown in Figure 3.18. Although there are two layers of *h*-BN, however, there is no noticeable change as compared to the monolayer case. The same trend is stated by ref. [TVW+16] where it was observed that the increase in the number of *h*-BN layers did not lead to qualitative changes.
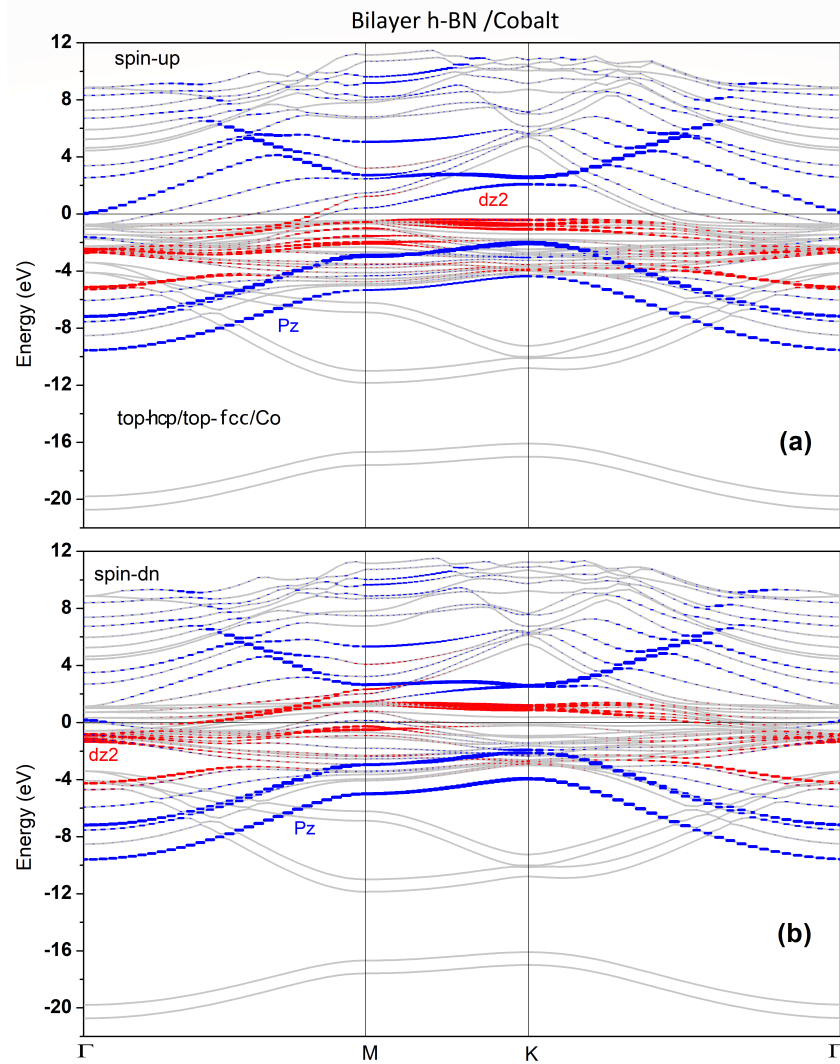
Figure 3.18: Calculated band structures for spin-up (a), spin-down (b) for bilayer *h*-BN on Co(0001) for the most stable *top(N)-hcp(B)/top(N)-fcc(B)/Co* configuration. Blue lines represent the p_z orbitals of the π-band and the red lines the d_{z^2} orbitals of cobalt.

3.9.3.3 Charge Transfer

Using Bader's analysis, we calculated the charges transfer for the two most stable configurations as reported in Table 3.14. The adsorbed layer is unchanged and stayed the same at the interface of monolayer h-BN ($+0.12|e|$ for *Co*, $-0.02|e|$ for *N* and $-0.09|e|$ for *B*). We observed the weak contribution of the second layer of both h-BN and cobalt surface. This confirms that the interaction is mainly limited to the first layer of the h-BN and the cobalt surface.

Table 3.14: Bader charges of the *B1* and *N1* atoms of the first h-BN layer, (*B2* and *N2*) of the second h-BN layer as well as of the cobalt atoms of the first and second layer (*Co1* and *Co2*).

Configurations	N1	B1	N2	B2	Co1	Co2
top(N)-hcp(B)/ **top(N)-fcc(B)/Co**	-0.02	-0.091	-0.0015	0.0001	0.114	-0.001
hcp(N)-fcc(B)/ **top(N)-hcp(B)/Co**	-0.02	-0.091	-0.0014	0.0002	0.123	-0.008

3.10 Summary

First-principles calculations within density functional theory (DFT) were performed to study a monolayer and bilayer interface of graphene (h-BN) with a cobalt substrate and its corresponding structural, magnetic and electronic properties. In the case of graphene, from the 6 (12) possible configurations for the monolayer (bilayer), 2 (4) most stable configurations were defined. For h-BN, the 4 most stable configurations were found from the 12 (12) possible ones for the monolayer (bilayer). A complete panorama of bond energies, equilibrium distances between atoms, magnetic moments on *Co* atoms and induced moments on *C* (graphene) and *B* and *N* (h-BN) atoms is proposed. Band structures and density of states calculations, derived for the most stable configurations, allowed attributing the magnetic behaviour at the graphene (h-BN)/Cobalt interfaces to the hybridization between the p_z orbitals of graphene (h-BN) and d_{z^2} of cobalt and to the resulting charge transfer between the cobalt and carbon (boron and nitrogen) atoms. It also appears that in the case of bilayers, the layer in direct contact with the topmost *Co* atoms plays a preponderant role.

FOUR

TWISTED BILAYER GRAPHENE/COBALT INTERFACE

Contents

4.1 Introduction

This chapter is devoted to the study by means of *ab-inito* calculations of the electronic and magnetic properties of the twisted bilayer graphene/Co(0001) interface. The considered twisting angles are 13.17°, 32.20° and 21.79°, corresponding to reasonable calculation time.

4.2 Twisted Bilayer Graphene (TBG)

4.2.1 Structural Properties

The twisted bilayer configurations can be formed with starting from AB-stacked bilayers graphene, the bottom layer is fixed, and the top layer is rotated, i.e. two layers are rotated relative to each other [SSST15]. The large cell sizes (up to 10^5 carbon atoms) are obtained from the little rotation angles, the number of atoms in a unit cell increases with decreasing of the rotation angle, the commensurate angle 21.79° is the smallest possible cell, which consists of 28 carbon atoms in the unit cell [UFIO14]. We choose three twist angles θ of 21.79°, 32.20° and 13.17° because they have fewer atoms in a cell than the other possible angles, which are shown in Figures 4.1 a-c.

(a) (b)

(c)
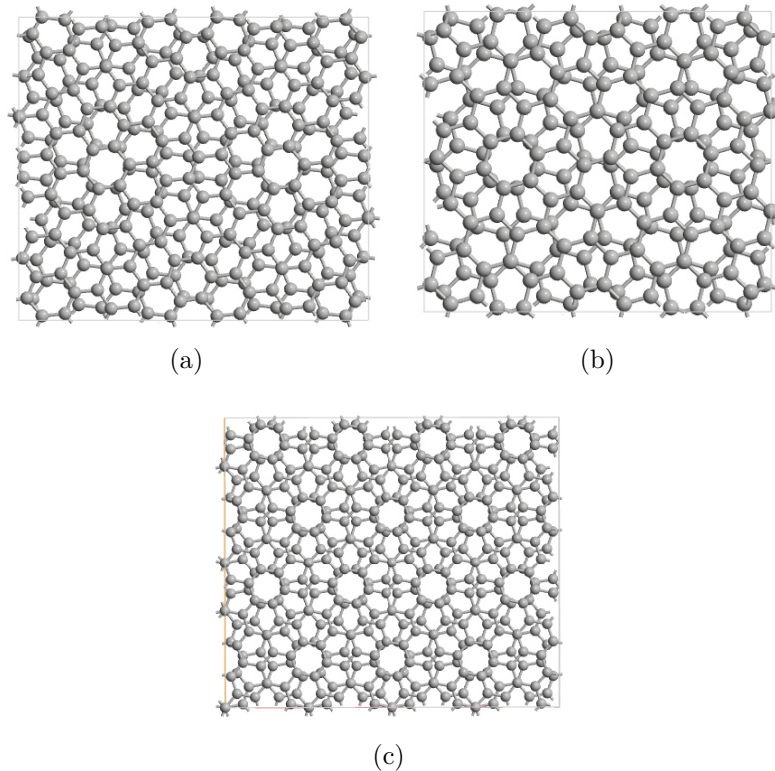
Figure 4.1: Different structures of twisted bilayer graphene (a) 13.17°, (b) 32.20° and (c) 21.79°.

4.2.2 Electronic Properties

The presence of a second graphene layer changes in the electronic properties, drastically when twisting the layers of graphene. The band structures of the single-layer graphene is characterized by the well-known linear dispersion, whereas the parabolic dispersion owns by the bilayers graphene. The TBG bands preserve the linear dispersion around the Dirac point like in the SLG case, this behavior is responsible for the weak coupling between layers. The expanded unit cell of TBG leads to reduced Brillouin zone with band folding, which prunes the range of linear dispersion. Our results are shown in Figures 4.2 are in good agreement with literature [SSP08, MCV+10, CW11, LST+13].

(a)

(b)

(c)
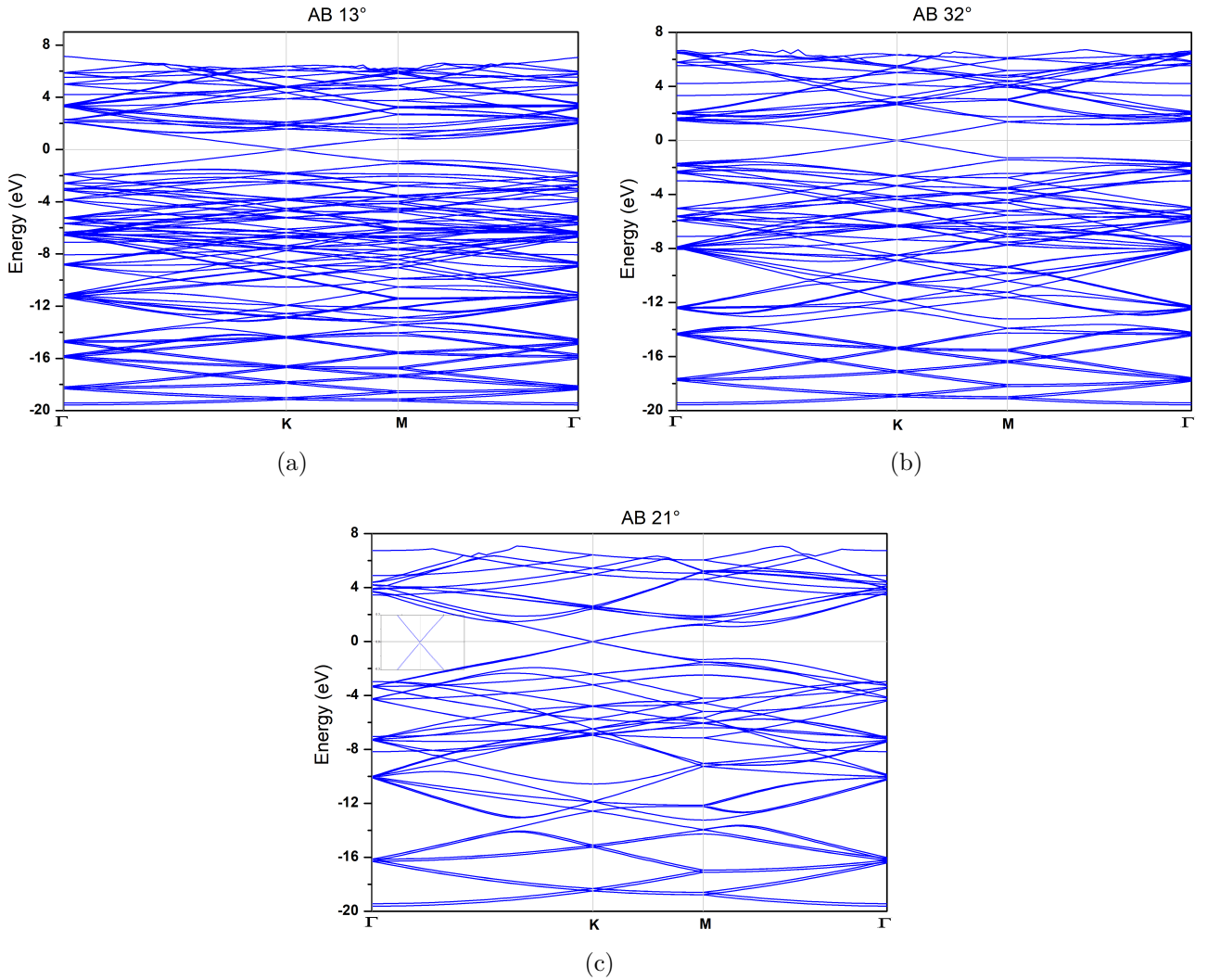
Figure 4.2: Energy band dispersion for three twisting structures of graphene (a) 13.17° (b) 32.20° (c) 21.79°.

4.3 Twisted Bilayer Graphene/Co(0001) Interface

4.3.1 Structural Properties

We are interested here in the case of a twisted bilayer graphene, constituted by two superposed monolayers, covering a Co(0001) surface. We have applied a in plane strain, in order to let the same structures as of the bilayer graphene on Co(0001) and only changing the angles between the two graphene sheets by maintaining the same angle between the twisted bilayer graphene cell and the cobalt surface. In the case of the 21.79°, the system contains 28 *C* atoms and 45 *Co* atoms (Figure 4.4(c)). However, for 13.17° and 32.20° the systems contain 76 and 52 *C* atoms, respectively, and 80 *Co* atoms each (Figures 4.4 a and b). The binding energy (E_B), the optimized lattice cell L_{cell}, the graphene distance (d) of the carbon atoms (*C-C*); the mismatch between the TBG and the *Co* substrate, the intralayer (between the two graphene layers) distance dL and the average distances (D) of the carbon atoms from the *Co* surface are reported in Table 4.1. From the calculated binding energy ($E_B > 0$), we conclude that the structures are energetically not stable. From the lattice cell, we can calculate the average distance (d) between the carbon neighbors' atoms (*C-C*). For the TBG without substrate, we find the same value $d = 1.42$ Å for the three angles, however, due to the applied strain, for the TBG/Co(0001), d is 1.51 Å for 32.20°, 1.53 Å for 21.79° and 1.39 Å for 13.17°. The Figures 4.3 a-c shows the lattice cells for the three angles. For each angle, the value of d is not constant 1.51-1.54 Å for 21.79°, 1.50-1.52 Å for 32.20° and 1.39-1.40 Å for 13.17°. We find a mismatch (+) of 8.9 % and 7.7 % for 32.20° (dilation) and 21.79° respectively and a mismatch (-) of 4.4% for 13.17° (contraction).

Table 4.1: The binding energy (E_B), the optimized lattice cell L_{cell}, the graphene distance (d) of the carbon atoms (*C-C*), the mismatch between the TBG and the *Co* substrate, the interlayer (between the two graphene layers) distance dL and the average distances (D) of the carbon atoms from the *Co* surface. In parentheses the values of twisted graphene without substrate.

$\theta°$	E_B (eV)	D (Å)	dL (Å)	d(Å)	L_{cell} (Å)	Mismatch %
0	-0.114	2.099	3.35	1.42		
13.17	0.207	2.011	3.22 (3.38)	1.39 (1.42)	10.52 (10.75)	-4.4
32.20	0.104	1.997	3.34 (3.36)	1.53 (1.42)	7.00 (6.53)	8.9
21.79	0.268	2.046	3.32 (3.37)	1.51 (1.42)	9.41 (8.90)	7.7
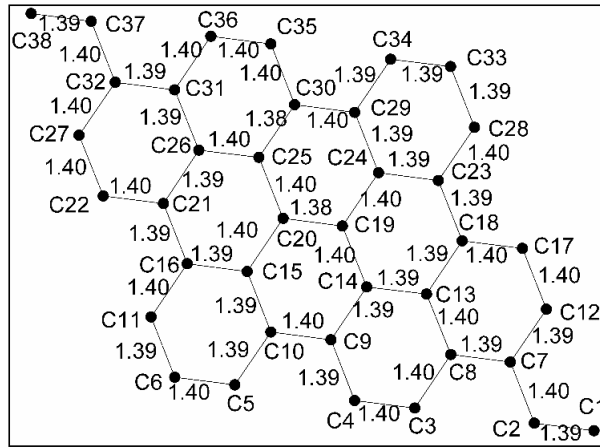
(a)
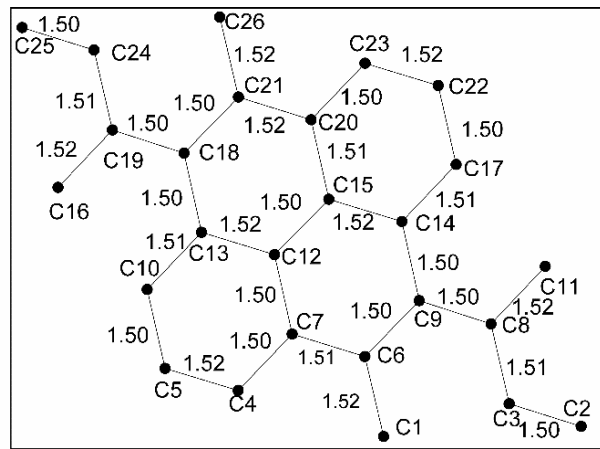
(b)
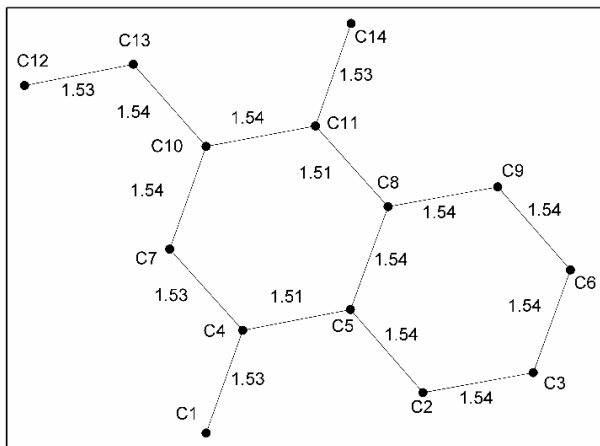
(c)

Figure 4.3: The graphene distance (d) of the carbon atoms (C-C) TBG/Co(0001) for 13.17° (a) 32.20° (b) 21.79° (c).
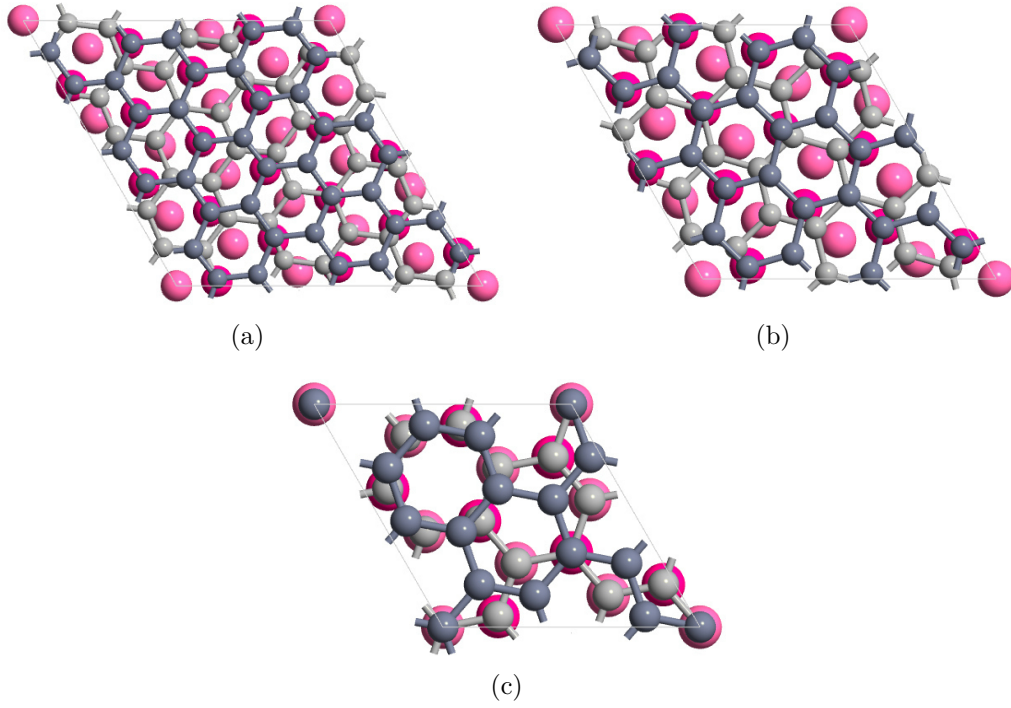
Figure 4.4: Twisted bilayer graphene on Co(0001) substrate for 13.17° (a) 32.20° (b) 21.79° (c). Light and dark pink colors are for *Co* atoms of the contact layer and the adjacent layer (2nd layer), respectively; light and dark gray colors are for the adsorbed (1st layer) and the second layer of graphene atoms, respectively.

Without applying a strain on the TBG/Co(0001) system, there is a rotation between the twisted bilayer graphene cell and the cobalt surface, by comparing to the case of not twisted bilayer graphene on Co(0001). From the Table 4.2, we find that the binding energy is negative ($E_B < 0$) and consequently the system is energetically stable. The graphene distance (d) of the carbon atoms (C-C) is 1.427 Å and it is equal to the d (1.42 Å) of the twisted graphene without substrate. The obtained value of the graphene interlayer distance dL is 3.22 Å and it is 4 % reduced from the dL value of case $\theta = 0°$.

Table 4.2: The binding energy (E_B), the interlayer (between the two graphene layers) distance (dL) and the average distances (D) of the carbon atoms from the Co surface.

$\theta°$	E_B (eV)	D (Å)	dL (Å)
0	-0.114	2.099	3.352
13.17	-0.115	2.090	3.269
32.20	-0.116	2.068	3.278
21.79	-0.136	2.088	3.180

4.3.2 Magnetic Properties

The obtained values of the magnetic moment (m) of carbone atoms, for the twist angles 13.17°, 21.79° and 32.20° are depicted in Figures 4.5 a-c, along with the calculated values for $\theta = 0°$ for comparison. In the case of $\theta = 21.79°$, for the first layer adsorbed on *Co* surface all the 7 *top-C* atoms exhibit an induced negative magnetic moment about -0.044 μ_B and are aligned antiparallel to those of the Co atoms and leading to an antiferromagnetic coupling to the *Co* atoms. The 7 *hcp-C* atoms have a positive magnetic moment 0.044 μ_B and are aligned parallel to those of the *Co* atoms and leading to a ferromagnetic coupling to the *Co* atoms. We find the same behavior observed for the case $\theta = 0°$ (see previous chapter).

For the case of $\theta = 32.20°$, for the first layer adsorbed on Co surface, all the 26 *C* atoms exhibit an induced magnetic moment varying from -0.09 to 0.03 μ_B. Nine (9) very nearby to the *top-C* position, it has a magnetic moment ranging between -0.010 and -0.018 which are close to corresponding *top-C* atoms of the case $\theta = 0°$. Twelve (12) *C* atoms have a magnetic moment of about 0.05 μ_B, only two ones have a positive magnetic moment of about 0.09 μ_B and three (3) atoms have m = -0.09 μ_B.

For the case of $\theta = 13.17°$, for the first layer adsorbed on *Co* surface, all the 38 *C* atoms exhibit an induced magnetic moment varying from -0.032 to 0.025 μ_B. Fifteen (15) have a negative magnetic moment ranging between -0.010 and -0.032 μ_B, this is due to how close the carbon atoms are to the *top* site (the first layer of cobalt surface). In contrast eight (8) *C* atoms have a positive magnetic moment ranging between 0.010 and 0.025 μ_B, this is due to how close they are as well to the *hcp* site (the second layer of cobalt surface). This corresponds to what has been found in $\theta = 0°$. The other atoms (8) have about m = 0.06 μ_B and others one (7 atoms) have m = -0.07 μ_B. In all cases, the magnetic moments carried by the carbon atoms of the second layer of graphene are found very weak.

The Figure 4.5 show the magnetic moment of cobalt atoms of the five (5) layers of the substrate and twisted graphene bilayer for the twist angles 13.17°, 32.20° and 21.79°. For the case of $\theta = 21.79°$, the magnetic moment carried by the *Co* surface atoms (*Co1*) in presence of graphene is found to be quenched to 1.49 μ_B (13.4%) compared to that of 1.72 μ_B for the graphene of the fifth sublayer *Co* (*Co5*) (departing from surface) that can be considered as a *Co* surface non-interacting with graphene (see Figure 4.5(c)). In the case of $\theta = 0°$, m was found to be quenched by 10.4%.

For the case of $\theta = 32.20°$ ($\theta = 13.17°$), as shown in Figures 4.5 a and b, the *Co* atoms (*Co1*) is quenched to 1.48 μ_B (1.50 μ_B), relatively 15% (16%), compared to that of 1.72 μ_B (1.74 μ_B) for the *Co* free surface.
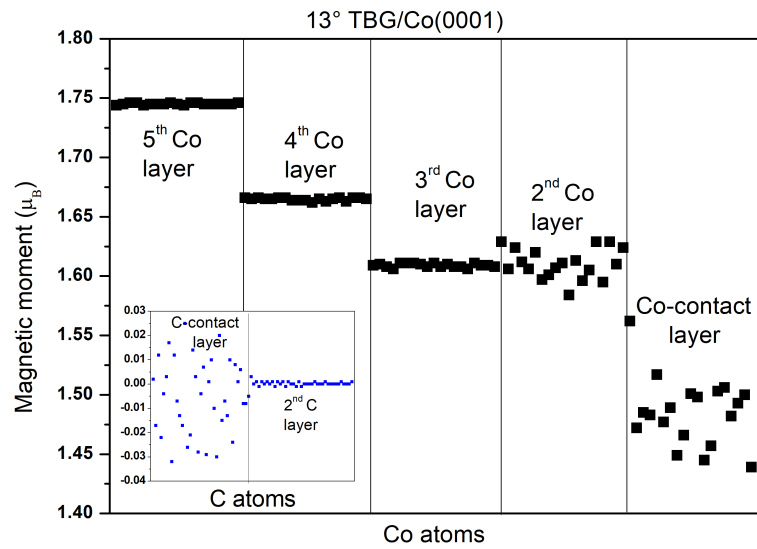
(a)
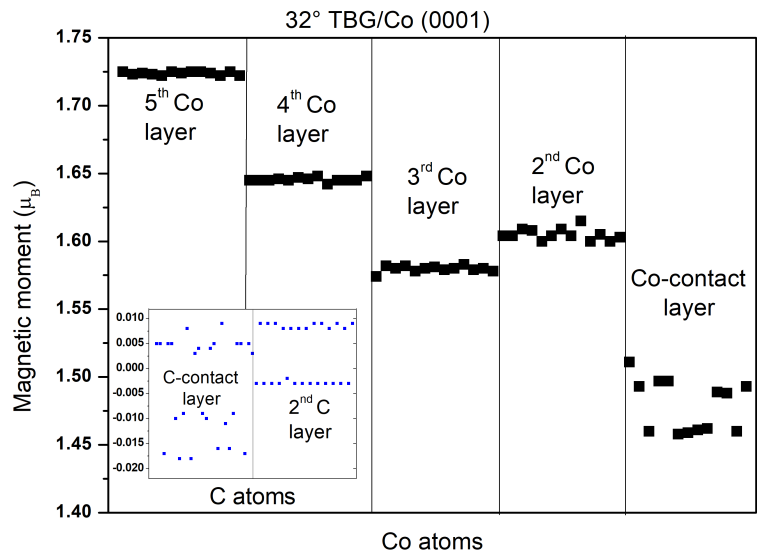
(b)
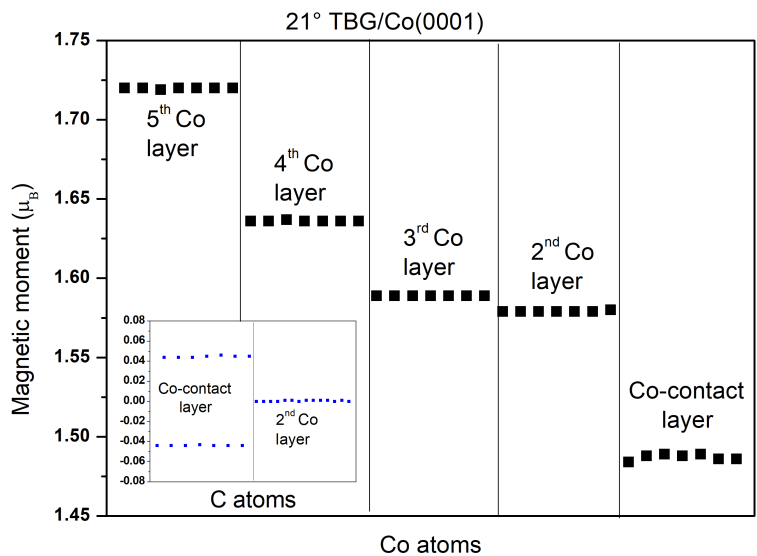
(c)

Figure 4.5: The magnetic moment of the Co substrate and twisted bilayer graphene of the TBG/Co(0001) system for 13.17° (a) 32.20° (b) 21.79° (c).

4.3.3 Electronic Properties

The density of states of the interface structure for twisting angles 13.17 °, 32.20°, 21.79° is shown in Figures 4.6. The contact layer C atoms shows the splitting of the electron states into up and down states, the same behavior is also observed for the neighboring layer (2nd layer). There is an affinity in the density of the cobalt contact layer and the layer next to it (2nd layer), this is due to the effect of the second layer by the interaction between the first layer of graphene and the first layer of cobalt. Similar results were found in the case $\theta = 0°$.
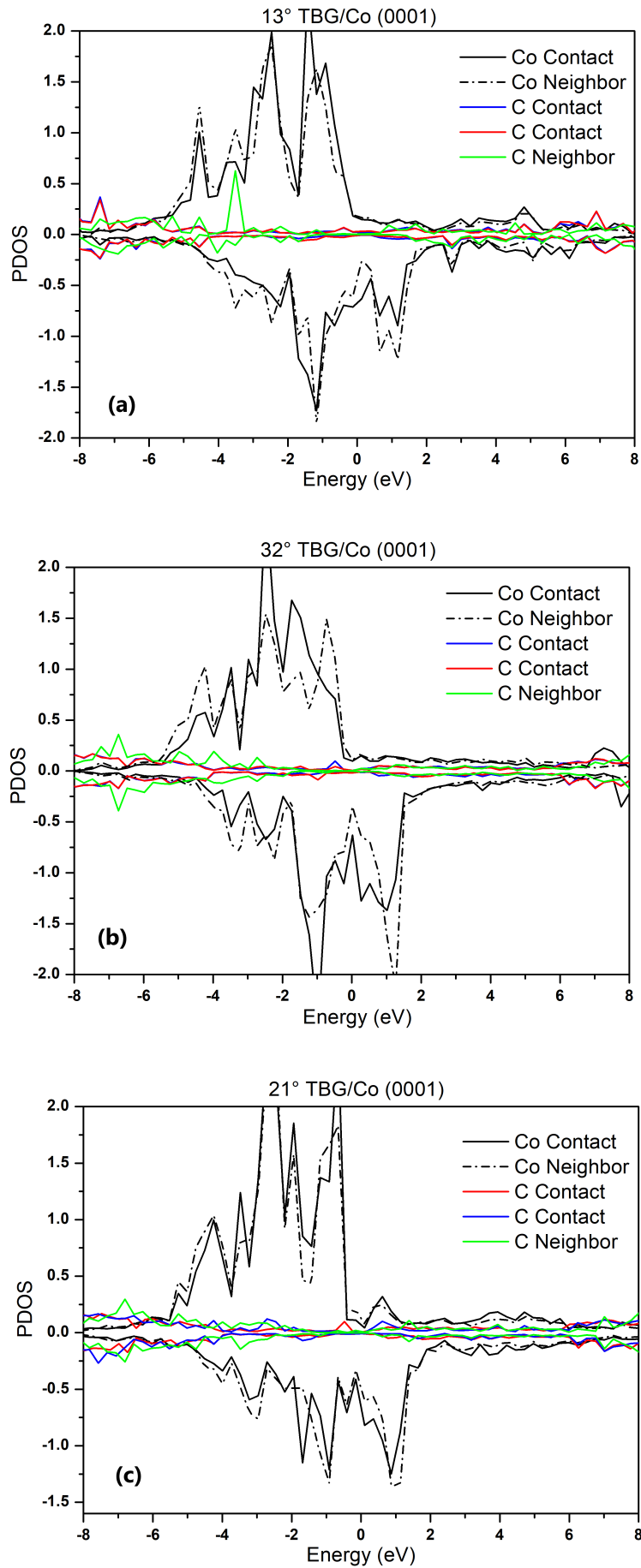
Figure 4.6: PDOS calculations for 13.17° (a), 32.20° (b) and 21.79° (c) structuers of twisted bilayer graphene on Co(0001).

4.4 Summary

In summary, by studying the twisted bilayer graphene on the cobalt surface, we found that by applying plane strain to the structure of twisted bilayer interfaces, it is unstable energetically, but when we rotate the twisted bilayer graphene cell from the cobalt surface, we obtain energetically stable structures. These TBG/Co(0001) interfaces were studied magnetically and electronically and the same behavior was found for the bilayer graphene/Co(0001) interface.

CONCLUSION AND FUTURE OUTLOOK

Nanomaterials are promising in various fields, as they have remarkable properties compared to bulk materials. Quantum physics controls nanoscale materials and is the comprehensive set of classical physics that governs bulk materials.

DFT was successfully applied as a quantum computational method to investigate the structural, magnetic and electronic properties of two-dimensional layered materials in this thesis. The adsorption of graphene and h-BN on a ferromagnetic substrate has been studied and discussed. Overall trends are illustrated, in terms of binding energy (stability), the most stable sites (bridge, *top*, *fcc* or *hcp*), magnetization, the density of state, band-gap at the Fermi energy level and charge transfer.

Our primary goal was to study the interface of h-BN and graphene with cobalt surface. This study also looked at graphene and h-BN bilayers on Co substrate and compared the results with their monolayers counterparts. The results confirmed that the most stable structure is the *top-fcc* and *top-hcp* stacking, which is the same obtained in bilayers structure. Both the *top-C* and the *fcc-C* or the *hcp-C* atoms exhibit an antiferromagnetic and a ferromagnetic coupling respectively and are only mainly limited to the first layer in contact with cobalt. The DOS results show a split into spin-up and spin-down states for C (B, N) atoms. The BS exhibit that bilayer graphene has an open gap in the graphene band, but increased by about 0.5 eV for the majority channel while for the minority channel we observe a Dirac cone at K point below the Fermi level with a small gap of about 0.11 eV in comparison with monolayer graphene. For the h-BN bilayer, we noted that the characteristic gaping structure of h-BN free-standing is kept at the region of K point as observed with its monolayer. The charge transfer confirms the occurrence of the hybridization between the out-of-plane $\pi(p_z)$ orbitals of graphene (h-BN) and metallic d_{z^2} orbitals of cobalt. As consequence, the C (B, N) atoms acquire a magnetic moment while the one of Co atoms is slightly quenched. The study was also conducted on twisted bilayer graphene interfaces. These structures exhibit magnetic and electronic behavior almost similar to that of the non-twisted bilayer interface.

As future work, expanding the study to involve the effect of twisted bilayer hexagonal boron

75

nitride with the cobalt substrate via accurate *ab-initio* calculation method. More features can be calculated, e.g. work function, vibration energies and mechanical stress. Experimenting with elemental absorption on graphene is very difficult, as manipulation is required at the atomic level. These results can be used to aid, accelerate, and guide experiments. Other *2D* twisted material inspection can be helpful in opening more applications.

[AD13]   H. Aoki and M.S. Dresselhaus. *Physics of Graphene.* NanoScience and Technology. Springer International Publishing, 2013. ISBN 9783319026336.

[AGEA15]   Nada F Atta, Ahmed Galal, and EH El-Ads. Graphene–a platform for sensor and biosensor applications. volume 9, pages 38–84. IntechOpen, 2015.

[AOG$^+$20]   A Avsar, H Ochoa, Francisco Guinea, B Özyilmaz, BJ Van Wees, and Ivan J Vera-Marun. Colloquium: Spintronics in graphene and other two-dimensional materials. *Reviews of Modern Physics*, 92(2):021003, 2020.

[ARDJT14]   Alberto Ambrosetti, Anthony M Reilly, Robert A DiStasio Jr, and Alexandre Tkatchenko. Long-range correlation energy calculated from coupled atomic response functions. *The Journal of chemical physics*, 140(18):18A508, 2014.

[ASBZ13]   Tesfaye Abtew, Bi Ching Shih, Sarbajit Banerjee, and Peihong Zhang. Graphene–ferromagnet interfaces: hybridization, magnetization and charge transfer. *Nanoscale*, 5(5):1902–1909, 2013.

[BGR16]   GR Bhimanapati, NR Glavin, and Joshua Alexander Robinson. 2d boron nitride: synthesis and applications. In *Semiconductors and semimetals*, volume 95, pages 101–147. Elsevier, 2016.

[BHZ17]   Qiaoliang Bao, Huiying Hoh, and Yupeng Zhang. *Graphene Photonics, Optoelectronics, and Plasmonics.* CRC Press, 2017.

[BLÁH14]   Tomáš Bučko, Sébastien Lebègue, János G Ángyán, and Jürgen Hafner. Extending the applicability of the tkatchenko-scheffler dispersion correction via iterative hirshfeld partitioning. *The Journal of chemical physics*, 141(3):034114, 2014.

[BLHA13]   Tomas Bucko, Sebastien Lebegue, Jugen Hafner, and Janos G Angyan. Improved density dependent correction for the description of london dispersion forces. *Journal of chemical theory and computation*, 9(10):4293–4299, 2013.

[Blö94]   Peter E Blöchl. Projector augmented-wave method. *Physical review B*, 50(24):17953, 1994.

[BO27]   Max Born and Robert Oppenheimer. Zur quantentheorie der molekeln. *Annalen der physik*, 389(20):457–484, 1927.

[Boe94]   JC Boettger. Nonconvergence of surface energies obtained from thin-film calculations. *Physical Review B*, 49(23):16798, 1994.

[Böe19]   Udo W. Böer, Karl W.and Pohl. *Quantum Mechanics of Electrons in Crystals.* Springer International Publishing, 2019.

[Cao04]   Guozhong Cao. *Nanostructures & nanomaterials: synthesis, properties & applications.* Imperial college press, 2004.

[CJKK08]   Sangkook Choi, Byoung Wook Jeong, Seungchul Kim, and Gunn Kim. Monovacancy-induced magnetism in graphene bilayers. *Journal of Physics: Condensed Matter*, 20 (23):235220, 2008.

[CL11]   Wonbong Choi and Jo-won Lee. *Graphene: synthesis and applications.* CRC press, 2011.

[CLSK10]   Wonbong Choi, Indranil Lahiri, Raghunandan Seelaboyina, and Yong Soo Kang. Synthesis of graphene and its applications: a review. *Critical Reviews in Solid State and Materials Sciences*, 35(1):52–71, 2010.

[Cur14]   Marc Currie. Applications of graphene to photonics. Technical report, NAVAL RESEARCH LAB WASHINGTON DC PHOTONICS TECHNOLOGY BRANCH, 2014.

[CW11]   Zhifan Chen and Xiao Qian Wang. Stacking-dependent optical spectra and many-electron effects in bilayer graphene. *Physical Review B*, 83(8):081405, 2011.

[CWYL14]   Jing Jing Chen, Han-Chun Wu, Da Peng Yu, and Zhi-Min Liao. Magnetic moments in graphene with vacancies. *Nanoscale*, 6(15):8814–8821, 2014.

[DRS+04]   Max Dion, Henrik Rydberg, Elsebeth Schröder, David C Langreth, and Bengt I Lundqvist. Van der waals density functional for general geometries. *Physical review letters*, 92(24):246401, 2004.

[EC98]   Alan S Edelstein and RC Cammaratra. *Nanomaterials: synthesis, properties and applications.* CRC press, 1998.

[EPR+09]   Daejin Eom, Deborah Prezzi, Kwang Taeg Rim, Hui Zhou, Michael Lefenfeld, Shengxiong Xiao, Colin Nuckolls, Mark S Hybertsen, Tony F Heinz, and George W Flynn. Structure and electronic properties of graphene nanoislands on co (0001). *Nano letters*, 9(8):2844–2848, 2009.

[FBF+15]   Andrea C Ferrari, Francesco Bonaccorso, Vladimir Fal'Ko, Konstantin S Novoselov, Stephan Roche, Peter Bøggild, Stefano Borini, Frank HL Koppens, Vincenzo Palermo, Nicola Pugno, et al. Science and technology roadmap for graphene, related two-dimensional crystals, and hybrid systems. *Nanoscale*, 7(11):4598–4810, 2015.

[Fer27]   Enrico Fermi. Un metodo statistico per la determinazione di alcune priorieta dell'atome. *Rend. Accad. Naz. Lincei*, 6(602-607):32, 1927.

[Foc30]   Vladimir Fock. Näherungsmethode zur lösung des quantenmechanischen mehrkörper-problems. *Zeitschrift für Physik*, 61(1-2):126–148, 1930.

[FS16]   Yoshitaka Fujimoto and Susumu Saito. Band engineering and relative stabilities of hexagonal boron nitride bilayers under biaxial strain. *Physical Review B*, 94(24): 245427, 2016.

[GAEK10]   Stefan Grimme, Jens Antony, Stephan Ehrlich, and Helge Krieg. A consistent and accurate ab initio parametrization of density functional dispersion correction (dft-d) for the 94 elements h-pu. *The Journal of chemical physics*, 132(15):154104, 2010.

[GEG11]   Stefan Grimme, Stephan Ehrlich, and Lars Goerigk. Effect of the damping function in dispersion corrected density functional theory. *Journal of computational chemistry*, 32(7):1456–1465, 2011.

[GN10a]   A Geim and K Novoselov. For groundbreaking experiments regarding the two-dimensional material graphene. *The Nobel Prize in Physics*, 2010.

[GN10b]   Andre K Geim and Konstantin S Novoselov. The rise of graphene. In *Nanoscience and technology: a collection of reviews from nature journals*, pages 11–19. World Scientific, 2010.

[GPD+19]   S Matt Gilbert, Thang Pham, Mehmet Dogan, Sehoon Oh, Brian Shevitski, Gabe Schumm, Stanley Liu, Peter Ercius, Shaul Aloni, Marvin L Cohen, et al. Alternative stacking sequences in hexagonal boron nitride. *2D Materials*, 6(2):021006, 2019.

[GPKH14]   A.D. Güçlü, P. Potasz, M. Korkusinski, and P. Hawrylak. *Graphene Quantum Dots*. NanoScience and Technology. Springer Berlin Heidelberg, 2014. ISBN 9783662446119.

[Gri04]   Stefan Grimme. Accurate description of van der waals complexes by density functional theory including empirical corrections. *Journal of computational chemistry*, 25(12): 1463–1473, 2004.

[Gri06]   Stefan Grimme. Semiempirical hybrid density functional with perturbative second-order correlation. *The Journal of chemical physics*, 124(3):034108, 2006.

[GT09]   Zhen Guo and Li Tan. *Fundamentals and applications of nanomaterials*. Artech House, 2009.

[Ham14]   Ikutaro Hamada. van der waals density functional made accurate. *Physical Review B*, 89(12):121103, 2014.

[Har28]   Douglas Rayne Hartree. The wave mechanics of an atom with a non-coulomb central field. part ii. some results and discussion. In *Mathematical Proceedings of the Cambridge Philosophical Society*, volume 24, pages 111–132. Cambridge University Press, 1928.

[HK64]   Pierre Hohenberg and Walter Kohn. Inhomogeneous electron gas. *Physical review*, 136(3B):B864, 1964.

[HWWL02]   Roland Haubner, Matthias Wilhelm, Ronald Weissenbacher, and Benno Lux. Boron nitrides—properties, synthesis and applications. *High Performance Non-Oxide Ceramics II*, pages 1–45, 2002.

[JG13]   Niharika Joshi and Prasenjit Ghosh. Substrate-induced changes in the magnetic and electronic properties of hexagonal boron nitride. *Physical Review B*, 87(23):235440, 2013.

[KBM09]   Jiří Klimeš, David R Bowler, and Angelos Michaelides. Chemical accuracy for the van der waals density functional. *Journal of Physics: Condensed Matter*, 22(2): 022201, 2009.

[KF96]   Georg Kresse and Jürgen Furthmüller. Efficiency of ab-initio total energy calculations for metals and semiconductors using a plane-wave basis set. *Computational materials science*, 6(1):15–50, 1996.

[KFH94]   G Kresse, J Furthmüller, and J Hafner. Theory of the crystal structures of selenium and tellurium: the effect of generalized-gradient corrections to the local-density approximation. *Physical Review B*, 50(18):13181, 1994.

[KGK$^+$07] VM Karpan, G Giovannetti, PA Khomyakov, M Talanana, AA Starikov, M Zwierzycki, J Van Den Brink, G Brocks, and Paul J Kelly. Graphite and graphene as perfect spin filters. *Physical review letters*, 99(17):176602, 2007.

[KH93]   Georg Kresse and Jürgen Hafner. Ab initio molecular dynamics for liquid metals. *Physical Review B*, 47(1):558, 1993.

[KH94]   G Kresse and J Hafner. Norm-conserving and ultrasoft pseudopotentials for first-row and transition elements. *Journal of Physics: Condensed Matter*, 6(40):8245, 1994.

[KJ99]   Georg Kresse and Daniel Joubert. From ultrasoft pseudopotentials to the projector augmented-wave method. *Physical review b*, 59(3):1758, 1999.

[KJBG12]   Indu Kaul, Niharika Joshi, Nirmalya Ballav, and Prasenjit Ghosh. Hydrogenation of ferrimagnetic graphene on a co surface: Significant enhancement of spin moments by c–h functionality. *The journal of physical chemistry letters*, 3(18):2582–2587, 2012.

[KK12]   Mikhail Katsnelson and Mikhail Iosifovich Katnslson. *Graphene: carbon in two dimensions*. Cambridge university press, 2012.

[KMM96]   Charles Kittel, Paul McEuen, and Paul McEuen. *Introduction to solid state physics*, volume 8. Wiley New York, 1996.

[KNS15]   Ralph Koitz, Jens K Nørskov, and Felix Studt. A systematic study of metal-supported boron nitride materials for the oxygen reduction reaction. *Physical Chemistry Chemical Physics*, 17(19):12722–12727, 2015.

[Koh06]   Jorge Kohanoff. *Electronic structure calculations for solids and molecules: theory and computational methods.* Cambridge University Press, 2006.

[KRPSL09]   Lingzhu Kong, Guillermo Román-Pérez, José M Soler, and David C Langreth. Energetics and dynamics of h 2 adsorbed in a nanoporous material at low temperature. *Physical review letters*, 103(9):096103, 2009.

[KS65]   Walter Kohn and Lu Jeu Sham. Self-consistent equations including exchange and correlation effects. *Physical review*, 140(4A):A1133, 1965.

[KSF14]   Narjes Kheirabadi, Azizollah Shafiekhani, and Morteza Fathipour. Review on graphene spintronic, new land for discovery. *Superlattices and Microstructures*, 74: 123–145, 2014.

[KTK18]   Nandakumar Kalarikkal, Sabu Thomas, and Obey Koshy. *Nanomaterials: Physical, Chemical, and Biological Applications.* CRC Press, 2018.

[LA08]   Yu-Ming Lin and Phaedon Avouris. Strong suppression of electrical noise in bilayer graphene nanodevices. *Nano letters*, 8(8):2119–2125, 2008.

[LBS08]   Robert Laskowski, Peter Blaha, and Karlheinz Schwarz. Bonding of hexagonal bn to transition metal surfaces: An ab initio density-functional theory study. *Physical Review B*, 78(4):045409, 2008.

[Liu17]   Zhi Liu. *Transition Metal Nitrides and Their Solid Solutions: A First-Principles Approach with Cluster Expansion Computational Predictive Models.* PhD thesis, The University of Toledo, Spin, 2017.

[LKWVW16]   Johannes Christian Leutenantsmeyer, Alexey A Kaverzin, Magdalena Wojtaszek, and Bart J Van Wees. Proximity induced room temperature ferromagnetism in graphene probed with spin currents. *2D Materials*, 4(1):014001, 2016.

[LMK+10]   Kyuho Lee, Éamonn D Murray, Lingzhu Kong, Bengt I Lundqvist, and David C Langreth. Higher-accuracy van der waals density functional. *Physical Review B*, 82 (8):081101, 2010.

[LML07]   Fang Liu, Pingbing Ming, and Ju Li. Ab initio calculation of ideal strength and phonon instability of graphene under tension. *Physical Review B*, 76(6):064120, 2007.

[LST+13]   W Landgraf, S Shallcross, K Türschmann, D Weckbecker, and O Pankratov. Electronic structure of twisted graphene flakes. *Physical Review B*, 87(7):075433, 2013.

[LWKH08]   Changgu Lee, Xiaoding Wei, Jeffrey W Kysar, and James Hone. Measurement of the elastic properties and intrinsic strength of monolayer graphene. *science*, 321 (5887):385–388, 2008.

[LWW+15]   WQ Liu, WY Wang, JJ Wang, FQ Wang, C Lu, F Jin, A Zhang, QM Zhang, G Van Der Laan, YB Xu, et al. Atomic-scale interfacial magnetism in fe/graphene heterojunction. *Scientific reports*, 5(1):1–9, 2015.

[MA18]   BD Malhotra and MA Ali. Functionalized carbon nanomaterials for biosensors. pages 75–103. 2018.

[Mar04]   Richard M. Martin. *Pseudopotentials*, page 204–232. Cambridge University Press, 2004.

[Mar14]   Richard M Martin. *Electronic structure: basic theory and practical methods*. Cambridge university press, 2014.

[MBB+20]   Shantanu Mishra, Doreen Beyer, Reinhard Berger, Junzhi Liu, Oliver Groning, José I Urgel, Klaus Mullen, Pascal Ruffieux, Xinliang Feng, and Roman Fasel. Topological defect-induced magnetism in a nanographene. *Journal of the American Chemical Society*, 142(3):1147–1152, 2020.

[MCV+10]   E Suárez Morell, JD Correa, P Vargas, M Pacheco, and Z Barticevic. Flat bands in slightly twisted bilayer graphene: Tight-binding calculations. *Physical Review B*, 82 (12):121407, 2010.

[MJG11]   Jesse Maassen, Wei Ji, and Hong Guo. Graphene spintronics: the role of ferromagnetic electrodes. *Nano letters*, 11(1):151–155, 2011.

[MOP+17]   Sajedeh Manzeli, Dmitry Ovchinnikov, Diego Pasquier, Oleg V Yazyev, and Andras Kis. 2d transition metal dichalcogenides. *Nature Reviews Materials*, 2(8):1–15, 2017.

[MP76]   Hendrik J Monkhorst and James D Pack. Special points for brillouin-zone integrations. *Physical review B*, 13(12):5188, 1976.

[MP89]   MPAT Methfessel and AT Paxton. High-precision sampling for brillouin-zone integration in metals. *Physical Review B*, 40(6):3616, 1989.

[MSD⁺04]   Ann E Mattsson, Peter A Schultz, Michael P Desjarlais, Thomas R Mattsson, and Kevin Leung. Designing meaningful density functional theory calculations in materials science–a primer. *Modelling and Simulation in Materials Science and Engineering*, 13(1):R1, 2004.

[Nay16]   Pramoda Kumar Nayak. *Two-dimensional Materials: Synthesis, Characterization and Potential Applications*. BoD–Books on Demand, 2016.

[NGM⁺04]   Kostya S Novoselov, Andre K Geim, Sergei V Morozov, Dingde Jiang, Yanshui Zhang, Sergey V Dubonos, Irina V Grigorieva, and Alexandr A Firsov. Electric field effect in atomically thin carbon films. *science*, 306(5696):666–669, 2004.

[OHKL98]   Teri Wang Odom, Jin-Lin Huang, Philip Kim, and Charles M Lieber. Atomic structure and electronic properties of single-walled carbon nanotubes. *Nature*, 391 (6662):62–64, 1998.

[OHL⁺08]   Jeroen B Oostinga, Hubert B Heersche, Xinglan Liu, Alberto F Morpurgo, and Lieven MK Vandersypen. Gate-induced insulating state in bilayer graphene devices. *Nature materials*, 7(2):151–157, 2008.

[OSHD09]   Augusto F Oliveira, Gotthard Seifert, Thomas Heine, and Hélio A Duarte. Density-functional based tight-binding: an approximate dft method. *Journal of the Brazilian Chemical Society*, 20(7):1193–1205, 2009.

[OSKH13]   Carlo M Orofeo, Satoru Suzuki, Hiroyuki Kageshima, and Hiroki Hibino. Growth and low-energy electron microscopy characterization of monolayer hexagonal boron nitride on epitaxial cobalt. *Nano Research*, 6(5):335–347, 2013.

[OYMT11]   Thomas Olsen, Jun Yan, Jens J Mortensen, and Kristian S Thygesen. Dispersive and covalent interactions between graphene and metal surfaces from the random phase approximation. *Physical review letters*, 107(15):156401, 2011.

[PAV17]   John E Proctor, Daniel Melendrez Armada, and Aravind Vijayaraghavan. *An introduction to graphene and carbon nanotubes*. CRC Press, 2017.

[PBE96]   John P Perdew, Kieron Burke, and Matthias Ernzerhof. Generalized gradient approximation made simple. *Physical review letters*, 77(18):3865, 1996.

[Per09]   NMR Peres. The transport properties of graphene. *Journal of Physics: Condensed Matter*, 21(32):323201, 2009.

[PEVM94]   Wolfgang Pauli, Charles P Enz, and Karl Von Meyenn. *Writings on physics and philosophy.* Springer, 1994.

[Pro19]   Bianca Provost. *Density Functional Theory Study of Aromatic Adsorption on Iron Surfaces.* PhD thesis, University of Cambridge, Girton College, England, 2019.

[PW89]   Robert G Parr and Yang Weitao. Chemical potential derivatives. In *Density-Functional Theory of Atoms and Molecules.* Oxford University Press, 1989.

[PYPS16]   Haowei Peng, Zeng Hui Yang, John P Perdew, and Jianwei Sun. Versatile van der waals density functional based on a meta-generalized gradient approximation. *Physical Review X*, 6(4):041005, 2016.

[RP11]   RM Ribeiro and NMR Peres. Stability of boron nitride bilayers: Ground-state energies, interlayer distances, and tight-binding description. *Physical Review B*, 83 (23):235312, 2011.

[RT08]   Hashem Rafii-Tabar. *Computational physics of carbon nanotubes.* Cambridge University Press, 2008.

[RTM08]   Stephanie Reich, Christian Thomsen, and Janina Maultzsch. *Carbon nanotubes: basic concepts and physical properties.* John Wiley & Sons, 2008.

[Sah14]   Viraht Sahni. *Quantal Density Functional Theory II.* Springer, 2014.

[SAHR11]   S Das Sarma, Shaffique Adam, EH Hwang, and Enrico Rossi. Electronic transport in two-dimensional graphene. *Reviews of modern physics*, 83(2):407, 2011.

[SC11a]   Stephan N Steinmann and Clemence Corminboeuf. Comprehensive benchmarking of a density-dependent dispersion correction. *Journal of chemical theory and computation*, 7(11):3567–3577, 2011.

[SC11b]   Stephan N Steinmann and Clemence Corminboeuf. A generalized-gradient approximation exchange hole model for dispersion coefficients. *The Journal of chemical physics*, 134(4):044117, 2011.

[SHJ$^+$10]   Yumeng Shi, Christoph Hamsen, Xiaoting Jia, Ki Kang Kim, Alfonso Reina, Mario Hofmann, Allen Long Hsu, Kai Zhang, Henan Li, Zhen-Yu Juang, et al. Synthesis of few-layer hexagonal boron nitride thin film by chemical vapor deposition. *Nano letters*, 10(10):4134–4139, 2010.

[Sla29]   John C Slater. The theory of complex spectra. *Physical Review*, 34(10):1293, 1929.

[SMMB08]   Bhagawan Sahu, Hongki Min, AH MacDonald, and Sanjay K Banerjee. Energy gaps, magnetism, and electric-field effects in bilayer graphene nanoribbons. *Physical Review B*, 78(4):045404, 2008.

[SS11]   David Sholl and Janice A Steckel. *Density functional theory: a practical introduction.* John Wiley & Sons, 2011.

[SSP08]   S Shallcross, S Sharma, and Oleg A Pankratov. Quantum interference at the twist boundary in graphene. *Physical review letters*, 101(5):056803, 2008.

[SSST15]   M. Sharon, M. Sharon, H. Shinohara, and A. Tiwari. *Graphene: An Introduction to the Fundamentals and Industrial Applications.* Advanced Material Series. Wiley, 2015. ISBN 9781118842560. LCCN 2015025148.

[SŽA$^+$14] GM Sipahi, Igor Žutić, Nicolae Atodiresei, RK Kawakami, and Predrag Lazić. Spin polarization of co (0001)/graphene junctions from first principles. *Journal of Physics: Condensed Matter*, 26(10):104204, 2014.

[TAC09]   Mehmet Topsakal, E Aktürk, and SJPRB Ciraci. First-principles study of two- and one-dimensional honeycomb structures of boron nitride. *Physical Review B*, 79(11): 115442, 2009.

[TCY20]   Zihan Tang, Yue Chen, and Wei Ye. Calculation of surface properties of cubic and hexagonal crystals through molecular statics simulations. *Crystals*, 10(4):329, 2020.

[TDJCS12]   Alexandre Tkatchenko, Robert A DiStasio Jr, Roberto Car, and Matthias Scheffler. Accurate and efficient method for many-body van der waals interactions. *Physical review letters*, 108(23):236402, 2012.

[Tho27]   Llewellyn H Thomas. The calculation of atomic fields. In *Mathematical proceedings of the Cambridge philosophical society*, volume 23, pages 542–548. Cambridge University Press, 1927.

[TLMM10]   G Trambly Laissardière, Didier Mayou, and Laurence Magaud. Localization of dirac electrons in rotated graphene bilayers. *Nano letters*, 10(3):804–808, 2010.

[TNMY13]   Kenji Toyoda, Katsuya Nozawa, Nozomu Matsukawa, and Shigeo Yoshii. Density functional theoretical study of graphene on transition-metal surfaces: the role of

metal d-band in the potential-energy surface. *The Journal of Physical Chemistry C*, 117(16):8156–8160, 2013.

[TS09]   Alexandre Tkatchenko and Matthias Scheffler. Accurate molecular van der waals interactions from ground-state electron density and free-atom reference data. *Physical review letters*, 102(7):073005, 2009.

[Tsu14]   Takao Tsuneda. Density functional theory in quantum chemistry. 2014.

[TVW+16]   AA Tonkikh, EN Voloshina, P Werner, H Blumtritt, B Senkovskiy, G Güntherodt, SSP Parkin, and Yu S Dedkov. Structural and electronic properties of epitaxial multilayer h-bn on ni (111) for spintronics applications. *Scientific reports*, 6:23547, 2016.

[UFIO14]   Kazuyuki Uchida, Shinnosuke Furuya, Jun chi Iwata, and Atsushi Oshiyama. Atomic corrugation and electron localization due to moiré patterns in twisted bilayer graphenes. *Physical Review B*, 90(15):155451, 2014.

[UTB+18]   Dmitry Yu Usachov, Artem V Tarasov, Kirill A Bokai, Viktor O Shevelev, Oleg Yu Vilkov, Anatoly E Petukhov, Artem G Rybkin, Ilya I Ogorodnikov, Mikhail V Kuznetsov, Matthias Muntwiler, et al. Site-and spin-dependent coupling at the highly ordered h-bn/co (0001) interface. *Physical Review B*, 98(19):195438, 2018.

[Van90]   David Vanderbilt. Soft self-consistent pseudopotentials in a generalized eigenvalue formalism. *Physical review B*, 41(11):7892, 1990.

[VD11]   Elena Voloshina and Yuriy Dedkov. Electronic and magnetic properties of the graphene-ferromagnet interfaces: Theory vs. experiment. *Physics and Applications of Graphene-Experiments, edited by S. Mikhailov (InTech, 2011)*, pages 329–352, 2011.

[WA11]   H-S Philip Wong and Deji Akinwande. *Carbon nanotube and graphene device physics*. Cambridge University Press, 2011.

[War14]   Brullot Ward. Development, synthesis and characterization of multifunctional nanomaterials. *KU Leuven, Belgium*, 2014.

[Wik21]   Wikipedia. Empilement compact — Wikipedia, the free encyclopedia, 2021. [Online; accessed 25-February-2021].

[WLKG18]   Vei Wang, Yun Ye Liang, Yoshiyuki Kawazoe, and Wen-Tong Geng. High-throughput computational screening of two-dimensional semiconductors. *arXiv preprint arXiv:1806.04285*, 2018.

[WMS17]   Jingang Wang, Fengcai Ma, and Mengtao Sun. Graphene, hexagonal boron nitride, and their heterostructures: properties and applications. *RSC advances*, 7(27): 16801–16822, 2017.

[Wol14a]   Edward L Wolf. *Applications of graphene: an overview.* Springer, 2014.

[Wol14b]   E.L. Wolf. *Graphene: A New Paradigm in Condensed Matter and Device Physics.* OUP Oxford, 2014. ISBN 9780199645862. LCCN 2013940539.

[WRH+10]   Martin Weser, Yvonne Rehder, Karsten Horn, Muriel Sicot, Mikhail Fonin, Alexei B Preobrajenski, Elena N Voloshina, Eberhard Goering, and Yu S Dedkov. Induced magnetism of carbon atoms at the graphene/ni (111) interface. *Applied Physics Letters*, 96(1):012504, 2010.

[WTS+15]   Zhiyong Wang, Chi Tang, Raymond Sachs, Yafis Barlas, and Jing Shi. Proximity-induced ferromagnetism in graphene revealed by the anomalous hall effect. *Physical review letters*, 114(1):016603, 2015.

[WWW+13]   Jiangtao Wu, Baolin Wang, Yujie Wei, Ronggui Yang, and Mildred Dresselhaus. Mechanics and mechanically tunable band gap in single-layer hexagonal boron-nitride. *Materials Research Letters*, 1(4):200–206, 2013.

[WWW+16]   Qunhong Weng, Xuebin Wang, Xi Wang, Yoshio Bando, and Dmitri Golberg. Functionalized hexagonal boron nitride nanomaterials: emerging properties and applications. *Chemical Society Reviews*, 45(14):3989–4012, 2016.

[YH07]   Oleg V Yazyev and Lothar Helm. Defect-induced magnetism in graphene. *Physical Review B*, 75(12):125408, 2007.

[YHZ18]   Huijuan Cui Yuli Huang, Xiaoyun Li and Zhen Zhou. Bi-layer graphene: Structure, properties, preparation and prospects. *Current Graphene Science (Discontinued)*, 2 (2):97–105, 2018.

[ZFW+17]   Kailiang Zhang, Yulin Feng, Fang Wang, Zhengchun Yang, and John Wang. Two dimensional hexagonal boron nitride (2d-hbn): synthesis, properties and applications. *Journal of Materials Chemistry C*, 5(46):11992–12022, 2017.

[ZWS+09]   J Zhou, Q Wang, Q Sun, XS Chen, Y Kawazoe, and P Jena. Ferromagnetism in semihydrogenated graphene sheet. *Nano letters*, 9(11):3867–3870, 2009.

[ZZG11]   YG Zhou, Xiaotao T Zu, and Fei Gao. Substrate-induced magnetism in bn layer: A first-principles study. *Solid state communications*, 151(12):883–886, 2011.

Résumé: Les matériaux bidimensionnels (2D) tels que le graphène et l'hexagonal de nitrure de bore (*h*-BN), en raison des propriétés uniques qu'ils possèdent, ont suscité un intérêt croissant en tant que plateforme pour présenter des applications potentielles et futures dans les dispositifs optoélectroniques et spintroniques. Dans ce travail, nous avons étudié les propriétés structurale, magnétique et électronique des monocouche et bicouches de graphène et d'*h*-BN en interfaces avec un substrat de cobalt, en nous basant sur des calculs *ab-initio*. Ainsi, nous avons étudié l'effet d'un substrat de cobalt à travers une étude approfondie des systèmes graphène/Co(0001) et *h*-BN/Co(0001), pour différentes configurations d'empilement et déterminer les configurations les plus stables. Les principales propriétés électroniques et magnétiques sont expliquées au moyen des hybridations d'interface et de transfert de charge entre les atomes de *Co* et les atomes de *C* (*B* et *N*). Enfin, dans le cas du graphène, nous avons traité une situation plus compliquée lorsque les deux couches sont en rotation avec différents angles ce qui reflète le cas expérimental réel.

Abstract: Two-dimensional layered materials such as graphene and hexagonal boron nitride (*h*-BN), due to the unique properties they possess, have attracted increasing interest as a platform to present potential and future applications in optoelectronics and spintronics devices. In this work, we investigated the structural, magnetic, and electronic properties of monolayer and bilayer graphene and *h*-BN interfaced with a cobalt surface based on *ab-initio* calculations. Thus, we investigated the effect of a cobalt substrate through a deep study of graphene/Co(0001) and *h*-BN/Co(0001) systems, for different stacking configurations and find the more stable configurations. The main electronic and magnetic properties are explained by means of interface hybridizations and charge transfer between the *Co* atoms and *C* (*B* and *N*) atoms. Finally, for the graphene, we study a more complicated situation when the two layers are twisted, with different angles, which reflect the real experimental case.

ملخص: جذبت المواد ثنائية الأبعاد (2D) مثل الغرافين ونتريد البورون السداسي (*h*-BN)، نظرًا للخصائص الفريدة التي تمتلكها، اهتمامًا متزايدًا كمنصة لعرض التطبيقات المحتملة والمستقبلية في الأجهزة الإلكترونية الضوئية والإلكترونات السبنية. في هذا العمل، درسنا الخصائص الهيكلية والمغناطيسية والإلكترونية لواجهات الأحادية والثنائية الطبقات من الغرافين و*h*-BN مع ركيزة الكوبالت، بناءً على حسابات *ab-initio*. وعلى إثر هذا، قمنا بدراسة تأثير ركيزة الكوبالت من خلال دراسة متعمقة لأنظمة الغرافين /(0001) Co و *h*-BN /(0001) Co، لتكوينات المتراصة المختلفة ولتحديد التكوينات الأكثر استقرارًا. يتم شرح الخصائص الإلكترونية والمغناطيسية الرئيسية عن طريق تهجين ونقل الشحنة بين ذرات Co وذرات C (B وN). أخيرًا، في حالة الغرافين، تعاملنا مع حالة أكثر تعقيدًا عندما تدور الطبقتان بزوايا مختلفة مما يعكس الحالة التجريبية الحقيقية.